POROUS CATHODE DESIGN AND OPTIMIZATION OF LITHIUM SYSTEMS

by

Yen-Hung Chen

A dissertation submitted in partial fulfillment
of the requirements for the degree of
Doctor of Philosophy
(Mechanical Engineering)
in The University of Michigan
2008

Doctoral Committee:

Professor Ann Marie Sastry, Chair
Professor H. Scott Fogler
Professor Jyoti Mazumder
Professor Margaret Wooldridge
Chia-Wei Wang, Senior Engineer, Sakti3 Inc.

To My Family and Friends.

ACKNOWLEDGEMENTS

Firstly, and foremost, I would like to express my grateful thanks to my advisor Prof. Ann Marie Sastry for the guidance and support. Many thanks to you for the opportunity to work on this interesting and challenging project so that I learn how to be a great scholar, a great team leader, a great teacher, and a great parent from you. Your great expertise and knowledge as well as your enthusiasm and passion for work will always enlighten my future life and career.

Thank you to my committee members — Prof. H. Scott Fogler, Prof. Jyoti Mazumder, and Professor Margaret Wooldridge for serving on my committee and providing your precious advice on my thesis.

A big thank you to Dr. Chia-Wei Wang, my committee member, friend, brother, and mentor. You helped me explore my potential and fulfill my achievement. Thank you for always being encouraging, thoughtful and supportive.

Also, I would like to thank my colleagues from Prof. Sastry's group. Thank you for your support over the years and congenial environment. It has always been pleasure to stay in this big family and discuss problems with you. Thank you Dr. Munish Inamdar, Dr. Myounggu Park, Mr. HyonCheol Kim, Mr. Xiangchun Zhang, Mr. Myoungdo Chung, Mr. Min Zhu, and Mr. Sangwoo Han for supporting me throughout the last four years. Thanks also to the former group members: Dr. Fabio Albano, Dr. Yun-Bo Yi, Dr. Taeyong Kim, Ms. Tahira Reid, Dr. Kimberly Cook, Mr. Peter Verhees, and Mr. Tim

Slusser. I have so many wonderful moments with you guys in this group and I will always keep every detail in my mind.

Thank you to Prof. Wei Shyy for your advisement on optimization approaches. I would also like to thank Dr. Smitesh Bakrania, a friend and graduate schoolmate, for your support in TEM images and insightful suggestions.

Mr. Jeffery Stone, a true friend and brother, thank you for your jovial attitude and kindred spirit for listening, talking and being there.

A special thank you to my best friend Peter Ho for the infinite support. Even though I know that our friendship needs no words, I could not have had a better lunch hour and Friday night without you.

I am also deeply grateful to my friends, Ching-Chin, Hsun-Yi, Mitchell, Vivi, Edward, Holly, Jacob, Chien-Chou, and Chin-Yi for supporting me through difficulties and sharing joy and tears in this foreign country. Every footprint we have ever had together will never fade.

Finally, and most importantly, I would like to thank my parents Tsai-Te Chen and Chiung-Yu Chen Lu, and my sister Hung-Yin Chen, brother-in-law Meng-Hua Cheng, and younger sister Yi-Chour Chen, for their endless love. I could not have finished my doctoral studies without your support and encouragement.

I also wish to acknowledge the support provided by the US Department of Energy and the Lawrence Berkeley National Laboratories for this thesis work.

TABLE OF CONTENTS

LIST OF TABLES

LIST OF FIGURES

ABSTRACT

Narrowing the gap between theoretical and actual capacity in key Li-based battery systems can be achieved through improvements in both electronic and ionic conductivities of materials, via addition of conductive species. Additives do, however, penalize both volumetric and gravimetric properties, and also limit liquid transport and high rate performance. In this work, we developed techniques to design and optimize cathode system, based directly on the relationships among ionic and electronic conductivities, and specific energy for a range of commercially viable cathode electrochemistries, and additives. We also investigated formation mechanisms, and resulting geometric characteristics in nanoparticle agglomerates, to systematically study percolation and conductivity in self-assembled structures.

In our study of selection of conductive additives, architectures of model composite cathodes, comprised of active material, graphite, carbon black, and PVDF, were generated using our prior approach in simulating polydisperse arrangements. Several realizations of materials were used to predict conductivity. A key finding of this portion of the work, was that the conductive coatings strongly influence conductivity, via reduction of contact resistance. Percolation was detected at ≥30% in the cathode materials simulated cases, which was slightly larger than the percolation threshold (29%) for a 3D spherical particulate system. Thus, from this work, we conclude that neither surface nor bulk modifications of active material particles conductivities seem to be desirable targets for improvement of laminate conductivity, for the ranges of materials studied.

In the cathode optimization study, our results quantified trade-offs among ionic and electronic conductivity, and conductivity and specific energy. We also provided quantitative relationships for improved utilization and specific power, with higher specific energy. Finally, we provided quantitative guidance for design of high energy density $Li(Ni_{1/3}Co_{1/3}Mn_{1/3})O_2$ cells using conductive additives, and also provided guidelines for design of cathode systems, based directly on solid and liquid phase transport limitations. Future work will focus on higher rates of performance, and will be based on analyses here.

The grail, of course, in creating very highly conductive materials would be the achievement of ordered, self-assembled conductive particle chains which would be both highly connected, and manufacturable at low-cost. Thus, in our last effort, we studied particle made via combustion synthesis as a model system, both for the geometry of the particles involved, and also for the specific environmental importance of understanding their formation. In the agglomeration and aggregation study, 3D, branchlike nanoparticle agglomerates were systematically studied via use of new algorithms in generation of such structures. Though 2D TEM images provide insufficient geometric information for full, 3D reconstruction of such structures, they nonetheless provided ranges of structures from which we worked. Our findings in this portion of the study included the conclusion that Coulomb forces concentrated on the tip are likely root causes of the long chain-like shapes of observed clusters, creating branch-like soot agglomerates; particles tend to form a more compact and smaller cluster with van der Waals force. Under a certain combination of forces, including Coulomb and van der Waals forces, nanoparticles form self-similar structures with a specific fractal dimension.

CHAPTER I

INTRODUCTION

Li-ion batteries are the presently the leading potential energy storage technology for electric vehicles (EV) and hybrid electric vehicles (HEV) due to the high energy and power density through development of electrochemistries. However, a major obstacle to the development of lithium systems is the lack of systematically designed cathodes, the rate-limiting electrode in Li-batteries. Table 1.1 shows the energy storage system performance goals for EV and HEV [1-3]. The dramatic increase in required specific energy from power-assist EV to pure EV illustrates the importance of capacity improvement. Moreover, in spite of the emergence of a generation of cathode materials with higher energy densities, the gap between theoretical and actual capacity in these materials (e.g. $LiFePO_4$, $Li(Ni_{0.8}Co_{0.15}Al_{0.05})O_2$ and $Li(Ni_{1/3}Co_{1/3}Mn_{1/3})O_2$) remains very high, i.e. ~ 30%, as shown in Table 1.2 [4-10]. Low conductivity, both electronic and ionic, is the key culprit in the failure to realized close-to-theoretical values.

Conductive additives are presently used to create conductive networks, to increase electronic conductivity of these cathodes. Selection of optimal combinations of conductive additives, however, remains challenging, as choices of materials, and architectures, have grown dramatically. Monotonically increasing additives not only penalizes both volumetric and gravimetric properties, such as energy and power, but also

applications / characteristics	power-assist HEV	PHEV	EV
energy (kWh)	0.3~0.5	3.4~11.6	40
power (kW)	25~40	38~45	40~53.3
specific energy (Wh/kg)	7.5~8.3	57~97	150~200
specific power (W/kg)	665~667	317~750	300~400
discharge rate (C)	1	1~3	2
reference	[1]	[2]	[3]

Table 1.1: Energy storage system performance goals for power-assist hybrid electric vehicles (HEV), plug-in HEV, and EV

cathode material	general properties	theoretical capacity (mAh/g)	discharge capacity (mAh/g)	utilization	rate	additives	ref
$LiCoO_2$	easy to prepare	274	180	0.66	C/10	coated with Al_2O_3 7% carbon black	[4]
$LiNi_{1-x}Co_xO_2$	high capacity low cost	274 x=0.2	176	0.64	C/10	10% carbon black	[5]
$LiMn_2O_4$	low capacity high rate low cost	148	135 122	0.91 0.90	C/24 C/5	32% carbon black	[6]
			120	0.81	1C	10% carbon black	[7]
$LiFePO_4$	high energy density low electronic conductivity low cost	170	155	0.91	C/25	6% carbon black 6% graphite	[8]
			115	0.68	1C		
$Li(Ni_{0.8}Co_{0.15}Al_{0.05})O_2$	high specific energy high power	279	190	0.68	1C	3% carbon black	[9]
$Li(Ni_{1/3}Co_{1/3}Mn_{1/3})O_2$	high energy high capacity good cycle performance	278	185	0.67	C/10	40% teflonized acetylene black	[10]
			172	0.62	1C		

Table 1.2: Theoretical capacity and actual discharge capacity of different cathode materials.

limits liquid phase transport and lower ionic conductivity, impeding high rate performance. Optimization of conductivities by selecting shapes, sizes and densities of both additives and active particles is thus critical.

Reaching sufficient conductivity first requires achievement of percolation in the conductive phase [11-13]. This problem has been studied extensively for anode materials [14-17], and more generically for a variety of shapes of particles, but less so for specific cathode materials and particular loading schema. In the cathode system, gains have been achieved using multiple schema for loading with conductive additives, including nano-scale particles such as carbon black and micro-scale particles such as graphite. To optimize the fractions of two different scales of conductive particles by type and method beyond the percolation point, requires understanding of particle packing and/or agglomeration, along with validated models for determination of conductivity.

Alterations in loading method strongly affect percolation onset in single-phase systems [14], and thus resulting conductivities. Methods are thus needed to incorporate polydisperse, multiphase materials, in order to reduce costly experimentation. In this work, we have developed random packing algorithms and a voxelated finite element conduction model to predict the conductivity of cathodes with different amounts, types and architectures of conductive additives and active materials. We further identified the optimal blends of active materials, conductive additives, and binder to achieve the highest conductivities, for a range of materials available at present (Chapter II).

The cathode system does benefit in increasing effective conductivity from selection of optimal active materials and additives; however, the best overall performance may not result simply from the cathode electrode with best electronic conductivity, due to resulting reduced ionic conductivity in the liquid phase. Thus, to rationally design cathode systems in Li-batteries, optimizing the composition of conductive additives, active particles, porosity, and electrode thicknesses must be based on considerations of both solid and liquid phase transport properties. Optimization of battery design will undoubtedly replace sequential testing of various cathodic electrochemistries. In Chapter III, the relationship between the ionic and electronic conductivities with additives is mapped, and correlated to battery performance. Quantitative guidance for design of high power and energy density cells in better matching theoretical and actual capacity is also provided.

Recently, there has been a claim that self-assembled structures of mixtures of acetylene black and PVDF as additives dramatically reduces resistance [18] in cathode systems. A very low percolation threshold of acetylene black particles, for example, can be achieved due to elongated particle agglomerates. However, the key energetic drivers for the self-assembling processes and detailed characterizations of agglomerates have not been systematically studied. To understand agglomeration and aggregation phenomena in nanoparticles, we have used experiments and simulations to systematically study particle agglomerates forming mechanism and identify the geometric characteristics. Chapter IV details the formation of clusters by semi-stochastic placement and analysis of the morphology, which provides the baseline in conductivity and percolation study of self-assembled structure as future work.

Chapter V, to conclude, summarizes the major findings and future directions of our research.

BIBLIOGRAPHY

1. http://www.uscar.org/commands/files_download.php?files_id=83

2. http://www.uscar.org/commands/files_download.php?files_id=156

3. http://www.uscar.org/commands/files_download.php?files_id=27

4. Z. Chen, and J. R. Dahn, Studies of $LiCoO_2$ coated with metal oxides, Electrochemical and Solid-State Letters, 6 (11), A221-A224 (2003).

5. G. T. -K. Fey, R. F. Shiu, T. P. Kumar, C. L. Chen, Preparation and characterization of lithium nickel cobalt oxide powders via a wet chemistry processing, Materials Science & Engineering B, 100, (3), 234-243 (2003).

6. S. Mandal, J. M. Amarilla, J. Ibanez, and J. M. Rojo, The role of carbon black in $LiMn_2O_4$-based composites as cathodes for rechargeable lithium batteries, Journal of Electrochemical Society, 148, A24-A29 (2001).

7. A. S. Skapin, M. Gaberseck, R. Dominko, M. Bele, J. Drofenik, and J. Jamnik, Detection of highly conductive pathways in $LiMn_2O_4$-carbon black composites for Li ion batteries by microcontact impedance spectroscopy, Solid State Ionics, 167, 229-235 (2004).

8. K. Zaghib, J.Shim, A. Guerfi, P. Charest, and K. A. Striebel, Effect of carbon source as additives in $LiFePO_4$ as positive electrode for lithium-ion batteries, Electrochemical and Solid-State Letters, 8, A207-210 (2005).

9. S. -T. Myung, M. H. Cho, H. T. Hong, T. H. Kang, and C. –S. Kim, Electrochemical evaluation of mixed oxide electrode for Li-ion secondary batteries: $Li_{1.1}Mn_{1.9}O_4$ and $LiNi_{0.8}Co_{0.15}Al_{0.05}O_2$, Journal of Power Sources, 146, 222-225 (2005).

10. D. -C Li, T. Muta, L. -Q. Zhang, M. Yoshio, and H. Noguchi, Effect of synthesis method on the electrochemical performance of $LiNi_{1/3}Mn_{1/3}Co_{1/3}O_2$, Journal of Power Sources, 132, 150-155 (2004).

11. J. Quintanilla and S. Torquato, Clustering properties of d-dimensional overlapping spheres, Physical Review E, 54 (5), 5331-5339 (1996).

12. J. Quintanilla and S. Torquato, Clustering in a continuum percolation model, Advances in Applied Probability, 29 (2), 327-336 (1997).

13. Y. -B. Yi and A. M. Sastry, Analytical approximation of the two-dimensional percolation threshold for fields of overlapping ellipses, Physical Review E, 66, 066130-1-066130-8 (2002).

14. Y. -B. Yi and A. M. Sastry, Analytical approximation of the percolation threshold for overlapping ellipsoids of revolution, Proceedings of the Royal Society of London, Series A, 460, 2353-2380 (2004).

15. C. -W. Wang, K. A. Cook, and A. M. Sastry, Conduction in multiphase particulate/fibrous networks: simulations and experiments on Li-ion anodes," Journal of the Electrochemical Society, 150 (3), A385-A397 (2003).

16. C. -W. Wang, A. M. Sastry, K. A. Striebel, and K. Zaghib, Extraction of layerwise conductivities in carbon-enhanced, multilayered LiFePO4 cathodes, Journal of the Electrochemical Society, 152 (5), A1001-A1010 (2005).

17. Y. -B. Yi, C. -W. Wang, and A. M. Sastry, Compression of packed particulate systems: simulations and experiments in graphitic Li-ion anodes, Journal of Engineering Materials and Technology, 128, 73-80 (2006).

18. G. Liu, H. Zheng, A. S. Simens, A. M. Minor, X. Song, and V. S. Battaglia, Optimization of acetylene black conductive additive and PVDF composition for high-power rechargeable lithium-ion cells, Journal of Power Sources, 154 (12), A1129-A1134, (2007).

CHAPTER II

SELECTION OF CONDUCTIVE ADDITIVES IN LI-ION BATTERY CATHODES: A NUMERICAL STUDY[1]

INTRODUCTION

The lithium-ion cell has been successively improved incrementally with adoption of new cathode electrochemistries, from $LiCoO_2$ [1], to higher-capacity $LiNi_{1-x}Co_xO_2$ [2,3,4], to lower cost $LiNi_{1-x}Co_xO_2$ [5,6]. However, capacity fade and/or uncontrolled generation of flammable gasses during operation remain persistent problems. The addition of conductive additives to cathode materials has been demonstrated to improve capacity, via reduction of internal resistance, and cyclability. Typical materials (Table 2.1) [7,8,9,10,11,12,13,14] include carbon black (as an additive or a coating on cathode particles or current collectors), and graphite nonaqueous ultrafine carbon (UFC) suspensions. Selection of optimal combinations of conductive additives, though, remains challenging, as choices of materials, and architectures, have grown dramatically.

Gains have been achieved using multiple schema for loading with conductive additives, as summarized by Fig. 2.1 [15]. Performance has been improved by several measures, in different systems. But the relative gains in addition of additives, including

[1] Material in this chapter is a published paper: Y. -H. Chen, C. -W. Wang, G. Liu, X.-Y. Song, V. S. Battaglia, and A. M. Sastry, Selection of conductive additives in Li-ion battery cathodes: a numerical study, *Journal of the Electrochemical Society* 154 (10), A978-A986 (2007).

cathode material	theoretical capacity (mAh/g)	ref	additive	amount (wt.%)	performance enhancement		
					capacity (mAh/g)	conductivity	others
$LiCoO_2$	274	[7]	carbon	5-10	158	-	-
		[8]	carbon black	5	-	-	slight improvement in cyclability from 125 to 133 mAh/g in 10 cycles
$LiMn_2O_4$	148	[7]	carbon black	10	129	-	improvement in cyclability from 90 to 110 mAh/g in 50 cycles
		[9]	carbon black	32.2	135	-	-
		[10]	nonaqueous ultrafine carbon with TAB2	20 (1:3~1:1)	130	-	-
		[11]	carbon black	10	130	-	-
		[12]	carbon black	25 (v.f.)	120	conductivity increase: 10^{-5} to 1 S/cm	-
		[8]	carbon black	10	-	conductivity increase: 2.5×10^{-5} to 0.4 S/cm	-
$LiFePO_4$	170	[13]	carbon black	31	-	conductivity increase: 5×10^{-8} to 0.1 S/cm	-
		[14]	carbon black graphite	6 6	160	resistance decrease: 140 to 80 Wcm^2	-

Table 2.1: Improved performance by adding different additives in different cathode materials.

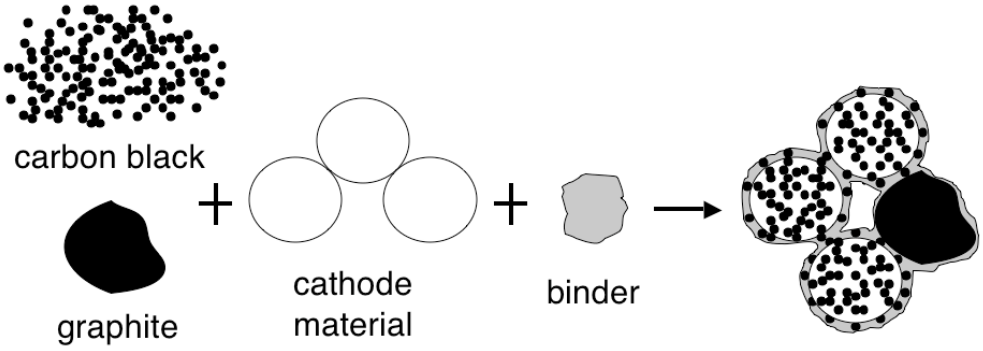

(a)

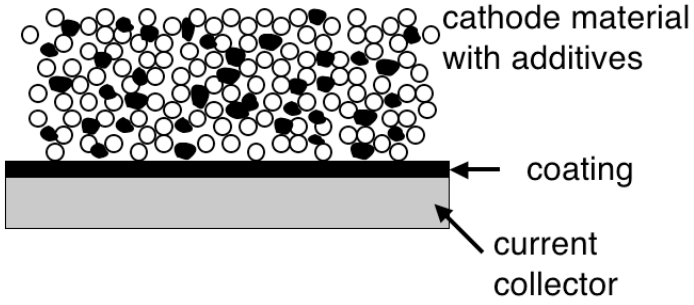

(b)

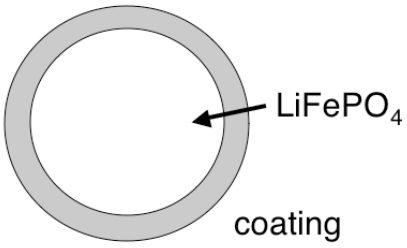

(c)

Figure 2.1: The possible ways to incorporate conductive additives: (a) addition of large (graphite) and small particles (carbon blacks), (b) current collector coating, and (c) coating of the cathode particles [15].

methods by which they can be added, have not been studied, though measurement of conduction has improved [16].

Four systems have emerged as important cathodes in recent studies Table 2.2: 1) the spinel $LiMn_2O_4$ [17,18], 2) $LiFePO_4$ [19,20], 3) the "Gen 2" material, $Li(Ni_{0.8}Co_{0.15}Al_{0.05})O_2$ put forward by the Department of Energy's ATD (Advanced Technology Development) program based at Argonne National Laboratories [21,22], and 4) the "1/3, 1/3, 1/3" system, $Li(Ni_{1/3}Co_{1/3}Mn_{1/3})O_2$ [23,24]. The strengths of these systems, include, respectively, low cost, high rate ($LiMn_2O_4$, per [17, 18]); low cost, high energy density $LiFePO_4$ [19,20,25]; high energy, high power ($Li(Ni_{0.8}Co_{0.15}Al_{0.05})O_2$, per [21, 22]); and high energy, high capacity, and good cycle performance ($Li(Ni_{1/3}Co_{1/3}Mn_{1/3})O_2$, per [23, 24]).

Achievement of sufficient conductivity first requires attainment of percolation in a conductive phase [26,27,28], a problem studied extensively for anode materials, and generically for a variety of shapes of particles [29,30,31,32]. There have also been published studies for specific cathode materials and loading schema [12,33]. Both particle shape and loading type are required in order to both identify percolation onset, and optimize addition of conductive particles by type and method beyond the percolation point. Even percolation onset is strongly affected by relatively minor changes in particles shape; for example, the percolation threshold is reduced from 30% to 10% as particle aspect ratio (L/D) increases from 1 to 6 [29]. It can thus be presumed that alterations in loading method have similarly strong effect on percolation onset, and overall conductivity. However, the conductance of gap regions, as opposed to simple bulk conduction, must also be modeled and mapped to experimental findings; additionally,

cathode material	reference	general properties	producer	targeted applications
$LiMn_2O_4$	[17,18]	low capacity high rate low cost	Toda	high power
$LiFePO_4$	[19, 20, 25]	high energy density low electronic conductivity low cost	Hydro Quebec	high energy or high power
$Li(Ni_{0.8}Co_{0.15}Al_{0.05})O_2$	[21, 22]	high specific energy high power	Fuji	high energy or high power
$Li(Ni_{1/3}Co_{1/3}Mn_{1/3})O_2$	[23, 24]	high energy high capacity good cycle performance	Seimi	high energy

Table 2.2: Important cathodes in recent studies.

methods are needed to incorporate the polydisperse, multiphase materials already in use, in order to reduce costly experimentation.

Our present study was focused upon the four electrochemistries mentioned earlier: $LiFePO_4$ (Hydro- Quebec, Inc., Quebec, Canada), $LiMn_2O_4$ (Toda Co. Ltd., Japan), $Li(Ni_{1/3}Co_{1/3}Mn_{1/3})O_2$ (Seimi Chemical Co. Ltd., Kanagawa, Japan), and $Li(Ni_{0.8}Co_{0.15}Al_{0.05})O_2$ (Fuji Chemical Industry Co., Ltd., Japan). The carbon black (Shawinigan) or graphite (SFG-6) was used as conductive additive. Poly(vinylidene fluoride) (PVDF, Kureha) was used as binder. The particle size and mass density of each material are listed in Table 2.3 [34,35,36]. We set two main objectives, with the present work:

1) To predict the conductivity of cathodes with different amounts, types and architectures of conductive additives and active materials; and

2) To identify the best blends of active materials, conductive additives, and binder to achieve the highest conductivity among combinations studied.

METHODS

Conduction experiments in our prior work [31] and others [36], have established baseline conductivities of materials. For packed particle arrangements, our prior model for packing [32] was used to construct the polydisperse structures of the model cathode systems, following classic and more recent work on numerical simulation of complex structures [32,37,38,39,40,41]. A voxelated finite element method was used to determine the effective conductivity of the multiphases networks, in order to meet our second objective of determining best blends of conductive additives, among those studied.

material	$LiMn_2O_4$	$LiFePO_4$	$Li(Ni_{0.8}Co_{0.15}Al_{0.05})O_2$	$Li(Ni_{1/3}Co_{1/3}Mn_{1/3})O_2$	graphite [34]
particle size (μm)	8.96	6.41	10.17	11.04	7.45
mass density (g/cm^3)	4.28	3.58	2.28	4.75	1.95
bulk conductivity (S/m)	5.56×10^{-4}	5.91×10^{-1}	4.00×10^{-2}	1.06×10^{-3}	–
conductivity from ref. (S/m)	10^{-4}~ 10^{-3} [35]	10^{-9} [36]	–	–	1.67×10^{4}

Table 2.3: Particle size (μm), mass density (g/cm^3), and bulk conductivities (S/m) of different active materials and graphite.

EXPERIMENTS

MEASUREMENT OF CONDUCTIVITY

Electronic properties of cathode materials are not widely reported. Importantly, it has been established in the presently-studied cathode materials, that manufacturing methods affect conductive properties [42,43]. The materials studied were prepared and tested for their conductive properties via a single approach, designed to reduce variability and allow application of classic theory in conduction to determine conductivity of the bulk phase.

Powders of active materials were placed into a round die of inner diameter 12.72 mm, and compressed with a force of 9.8 to 29.4 kN at 25°C for 5min to achieve various densities, using Carver Laboratory Press Model 2699. Pellet densification reduces particle separation distance and gap resistance [44], and generally is used to improve the accuracy of measured bulk conductivity.

The conductivity of a pellet was measured using an inline four-point-probe technique [31]; a schematic of the experiment is shown as Fig. 2.2. A current was delivered and withdrawn from the outer two probes; the voltage difference was measured from the inner two probes. The current source was a 1.2V AAA NiMH battery (Radio Shack) in series with resistance of 11MΩ. A Keithley 6517A Electrometer, and an HP 34401A multimeter were used to measure the current and the voltage respectively. The conductivity of the pellet was calculated [45] as

$$\sigma_e = \frac{I}{4.532tV}, \tag{1}$$

where σ_e is the conductivity of the pellet in S/mm, t is the thickness of the pellet in mm, I is the current measured in Amp, and V is the voltage measured in V. Equation (1) is valid for a single layer specimen.

For porous materials, Bruggeman [46] classically found that the effective conductivity, σ_e, is related to the bulk conductivity, σ_0, and the volume fraction of the solid phase, ε, as

$$\sigma_e = \sigma_0 \varepsilon^{\alpha}, \qquad \text{where } \alpha = 1.5 , \tag{2}$$

where α is the Bruggeman exponent, a curve fitting parameter for experimental results. Volume fraction ε is calculated from

$$\varepsilon = \frac{D_p}{D_B}, \tag{3}$$

where D_P and D_B are the density of pellet and density of bulk material respectively, whereupon bulk conductivity is determined directly.

MEASUREMENT OF PARTICLE SIZE AND SHAPE

Particle size distributions (PSD) were quantified using a Beckman Coulter LS230 Laser Diffraction Particle Size Analyzer, with a measurement range of between ~0.04 μm to 2000 μm. Sample powders of 0.05 ~ 0.10 g were mixed with 100 ml distilled water beaker where 5 drops Darvan C were used as a dispersant; uniformity was achieved with approximately 15 minutes of ultrasonic mixing.

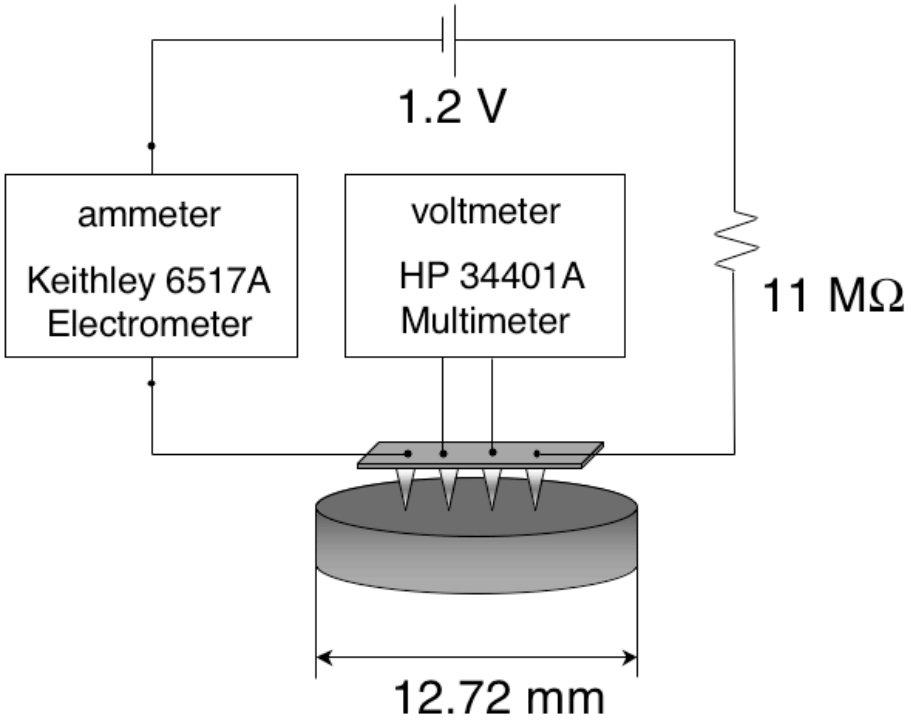

Figure 2.2: Schematic illustration of the configuration in conductivity measurement.

SIMULATIONS

PACKING ALGORITHM

The architecture of the composite cathode, comprised of active material, graphite, carbon black, and PVDF, was generated using our prior approach [32]. The general procedure is summarized briefly as follows: sizes and numbers of particles in each phase, as determined by the PSD and designated volume fraction, were initially placed randomly in a representative volume. Particles were simulated as spheres, ellipsoids, or coated objects. Repulsive forces between particles were applied to correct initial overlaps.

During the Li-ion cell preparation, all constituents are fully mixed, leaving, presumably, active material particles coated with composites of PVDF and carbon black. Carbon black particles are typically 10-90 nm [47] in diameter; the typical aggregate size of carbon black is 100-300 nm [47], though the primary aggregate may fracture during mixing [47]. Thus, a mixture of carbon black and polymer binder was approximated as a coating surrounded other particles, as shown in Fig. 2.3. This also allowed creation of simulations that were identical to experimental volume fractions.

Periodic boundary conditions and the collision algorithm were applied to achieve computational efficiency and fidelity to experimental conditions. The representative volume in this study was set to $1\times1\times2$ unit^3. Periodic boundary conditions were assigned in the x- and y- directions, to reduce the size of the simulation domain. The length of the representative volume in z- direction was set at a minimum of twice the length of each of the other two directions, because of the lack of a periodic boundary in that direction. The collision process was terminated when the total volume fraction of the unit volume in the

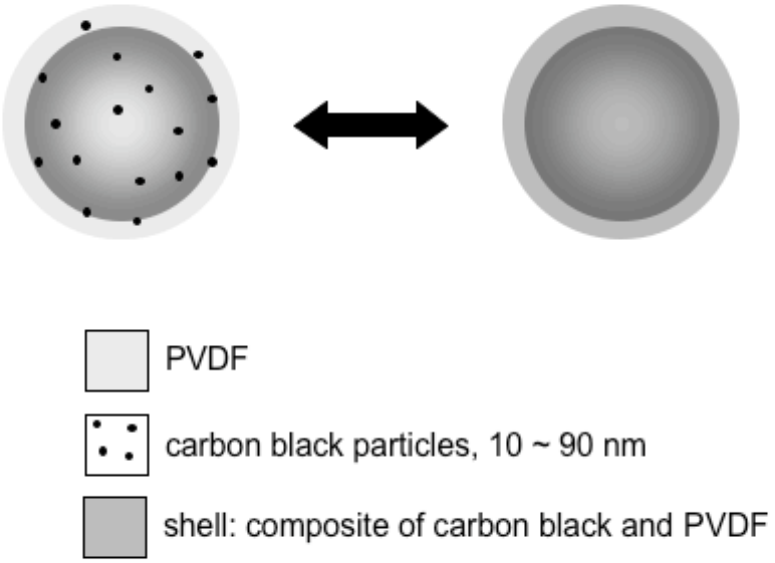

Figure 2.3: Schematic diagram of coating of carbon black/PVDF.

middle portion of the representative volume in z-direction was equal to the assigned volume fraction.

Relative sizes of materials are illustrated in Table 2.3. The radius of active materials was set to 0.15 of the representative volume; the semi-axes of graphite were dependent upon the size of active materials. The graphite was represented as a disk-like ellipsoid with aspect ratios a/b, a/c and b/c (a, b, and c are the lengths of three semi-axes) set to 1, 7.4 and 7.4, respectively. The mixture of the carbon black and PVDF was simulated as a coating around the active material and graphite particles. Table 2.4 lists factors (volume fraction of active material, porosity, graphite, and ratio of PVDF and carbon black) and levels of each. The volume fraction of carbon black and PVDF could be determined if porosity, the amount of active material, and the ratio of carbon black and PVDF were determined. Three simulation realizations were generated for each permutation of conditions studied.

CONDUCTIVITY MODELING

The active material and conductive additives particle aggregates are separated by an interfacial polymer layer. This feature is generally attributed to the occurrence of a tunneling effect through the insulating polymer. Combined with the conduction percolation through the aggregates, this phenomenon is known as “tunneling-percolation” [47]. The tunneling effect between paired particles can be simulated with assignment of a gap resistance. The value of this gap resistance depends on contact pressure, distance, and material properties of the contacting particles and polymer interface [44]. In the cases studied here, the gap resistance was assumed to be zero, since cathodes were usually

factor	level
porosity (v.f.%)	40 50
active material (v.f.%)	30 40 50
graphite (v.f.%)	0 2.5 5 7.5
PVDF/C	1.22 2.74 5.48

Table 2.4: List of simulation cases for each active material.

prepared with application of high compression pressure to reduce the distance among the packed particles, and the mixture of carbon black and PVDF served as coating around the particles binding particles directly. The current between contact surfaces is defined by

$$\left(V_a - V_b\right) = i \cdot R, \tag{4}$$

where i is current in amps, V_a and V_b are the electrical potentials on the points of both side of the contact surfaces in V, and R is the gap resistance in Ω.

Bulk conductivities of different active materials measured from experiments were assigned to corresponding phases. Figure 2.4 shows the conductivities of mixtures of carbon black and PVDF. In simulations, the conductivities of PVDF and carbon black were assigned three levels, as shown in Table 2.4, depending upon the ratio of PVDF and carbon black.

MODEL GENERATION AND ANALYSIS

Finite element meshing was performed using a voxelation method, to prevent mesh-induced singularities. The representative volume was set to 1×1×2 unit^3. Voxels of 100×100×100 were assigned to a unit volume, which was the middle portion of the representative volume in the z-direction. Assuming the representative volume in z-direction ranged from 0 to 2 units, the middle section was between 0.5 and 1.5 units, in the z-direction. A cubic element of length of 0.01 units enclosing the voxel was generated, with an assigned electronic conductivity.

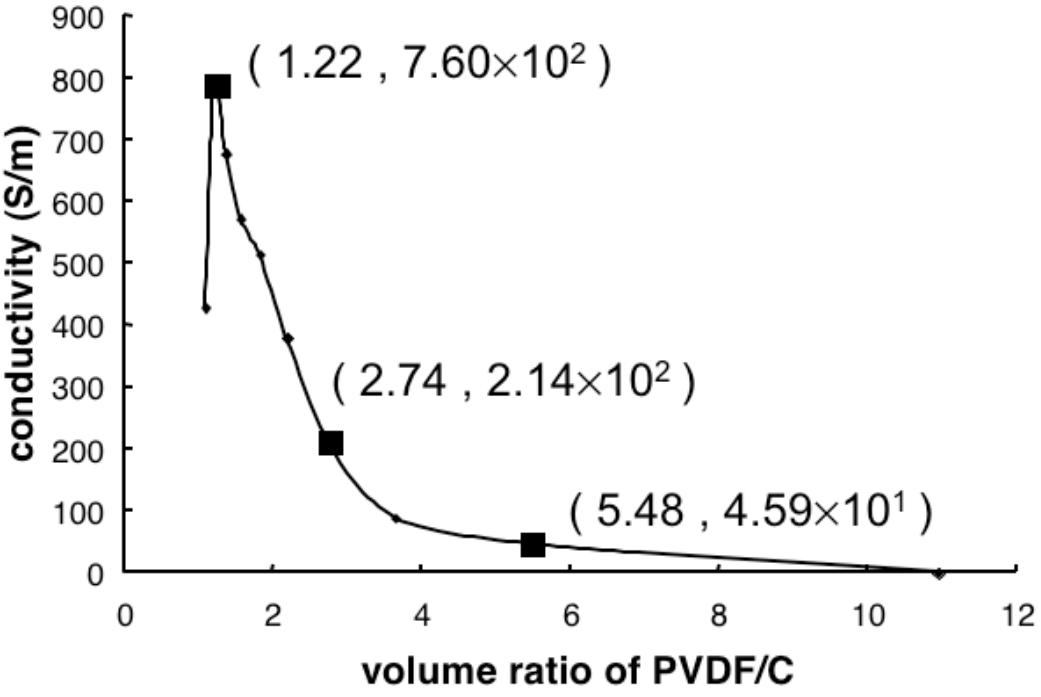

Figure 2.4: Conductivities of different combinations of carbon black and PVDF.

$$J = -\sigma_1 \nabla V , \quad (6)$$

$$F = -\sigma_2 \nabla T , \quad (7)$$

where σ_1 is electronic conductivity in S/m, J is the current density in A/m^2, V is the electrical potential drop in V along its length, σ_2 is thermal conductivity in W/m·K, F is the heat flux in W/m^2, and T is the temperature drop in K. Wall boundary conditions were set as 0K and 1K respectively, at x=0 and x=1. The total heat flux in the x- direction was calculated, whereupon effective conductivity of the cubic unit volume was determined via equation (7).

RESULTS

Table 2.3 contains materials properties, particle sizes, densities, and bulk conductivities used in simulations. Figure 2.4 reports the bulk conductivity of the carbon black and PVDF mixture. Increasing the carbon black content by 30 v.f.% resulted in 16-fold increase in conductivity. The only exception to this trend was for a 1:1 ratio of PVDF to carbon, where measured conductivity dropped to 420 S/m, i.e. the same value as for the 2.2:1 ratio.

Figure 2.5 shows examples of various microstructures (comprised of spherical active materials, graphite particles, and coated mixture of carbon black and PVDF) generated from collision modeling. Figure 2.5(a) illustrates an example of the microstructure of percolated network studied in the present work. Figure 2.5(b) and (c) illustrate the significant microstructural differences in materials of identical volume fraction, but different particle shapes and sizes.

The voxelated finite element model of Fig. 2.6(a) and (b) is an example of a multiphase analysis used to avoid mesh singularities around the contact region. Figure 2.6(a) shows the temperature distribution of core material, for a structure comprised of 30% active material, 7.5% graphite, and 40% porosity. Fig. 2.6(b) shows the temperature distribution of coatings for a volume composition of 10.15% carbon black and 12.35% PVDF.

Simulation results of normalized conductivities of $LiMn_2O_4$ system for various combinations of active materials, graphite, carbon black, and PVDF are reported in Fig. 2.7. Averaged data were plotted in the figures, with error bars of $\pm 1\sigma$ (standard deviation). Figures of results of other systems are omitted for brevity, since trends were similar; numerical results are reported in Tables 2.5 to 2.8.

Averaged normalized simulation results of conductivity with 40% and 50% porosity are presented in Tables 2.5 to 2.8. These tables report averaged, normalized conductivities for specific combinations of active material, graphite, and ratios of PVDF to carbon black. The two-way statistical analyses (by SPSS 12.0 [49]) of the simulation data are also given in Tables 2.5 to 2.8. The statistical analyses in term of p values allow determination of the significance of the effects of additives. Factors are considered significant if p is smaller than 0.05. The p values in rows denote the effect of increase in the ratio of PVDF to carbon black, on normalized conductivity. The p values in columns denote the effect of increase in the volume fraction of graphite on the normalized conductivity.

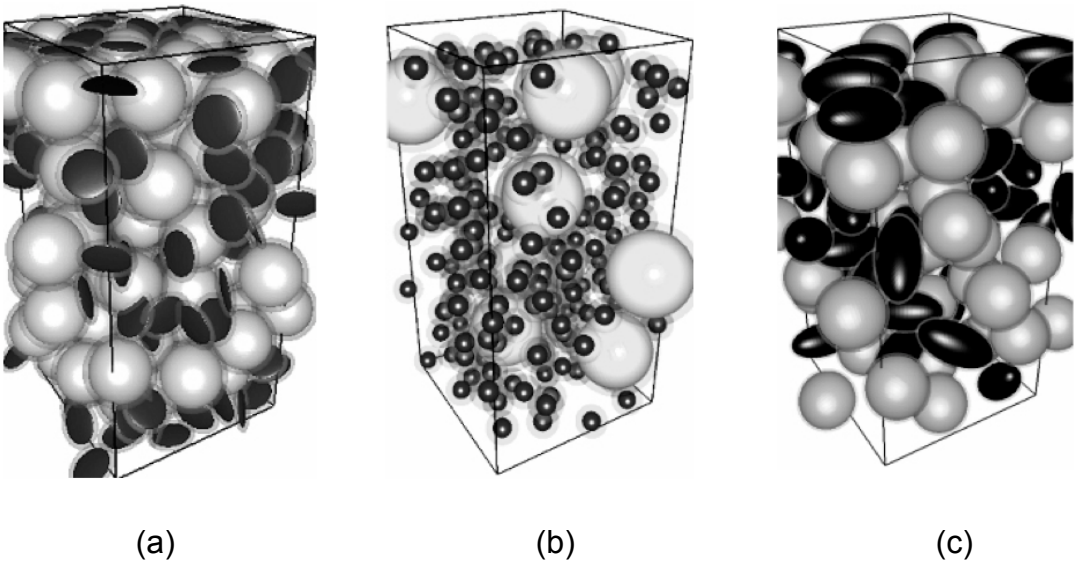

Figure 2.5: Packing simulations with different constituents, (a) 60% volume fraction mixture of spheres and platelets, representing cathode active material and graphite, (b) 40% volume fraction mixture of two different sizes, representing cathode active materials and carbon black, (c) 40% volume fraction mixture of ellipsoids and spheres, representing spherical cathode active materials, and ellipsoidal graphite fiber.

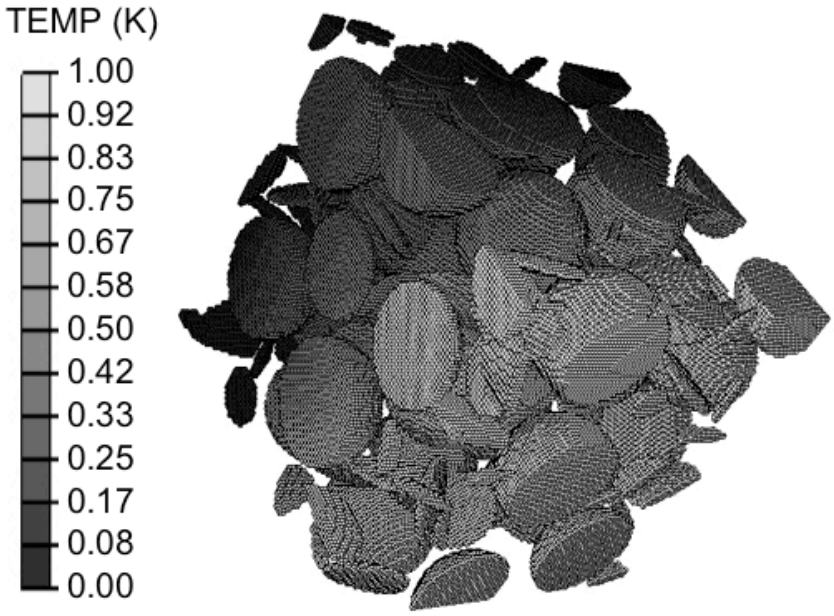

(a)

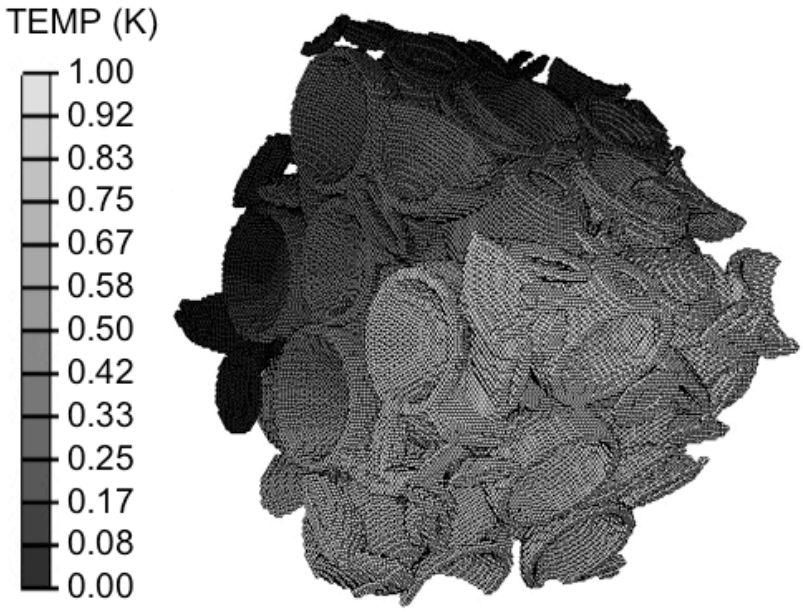

(b)

Figure 2.6: Temperature distribution from finite element analyses, structure of 40% porosity; 30% active material, 7.5% graphite, 10.15% carbon black, and 12.35% PVDF showing in (a) core material (active material and graphite) and (b) coatings (carbon black and PVDF).

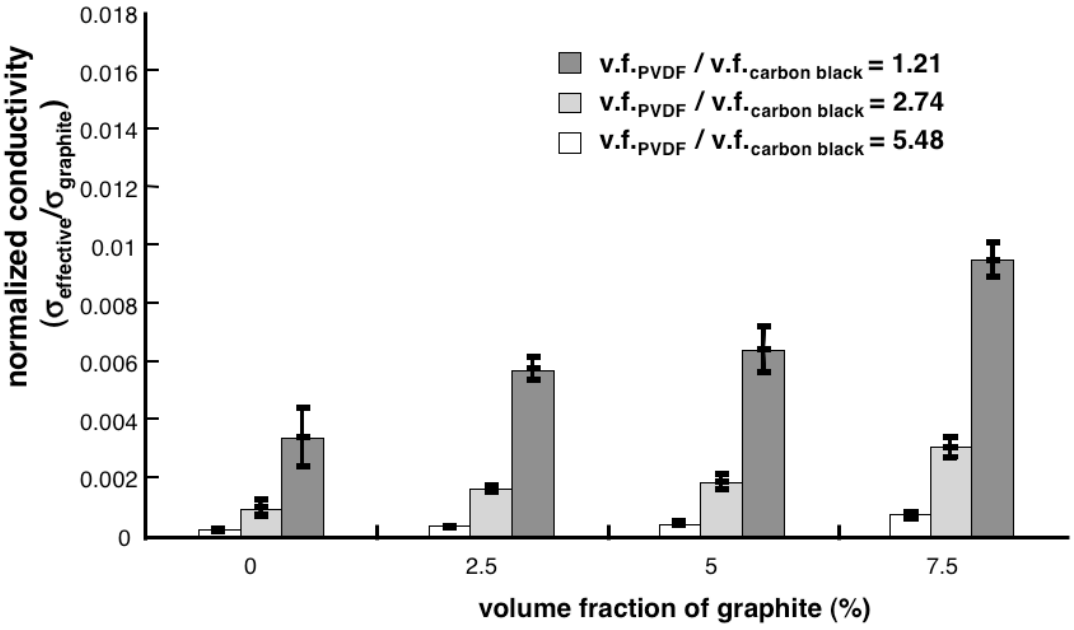

Figure 2.7(a): Conductivity of composite $LiMn_2O_4$ with 40% porosity and 30% active material.

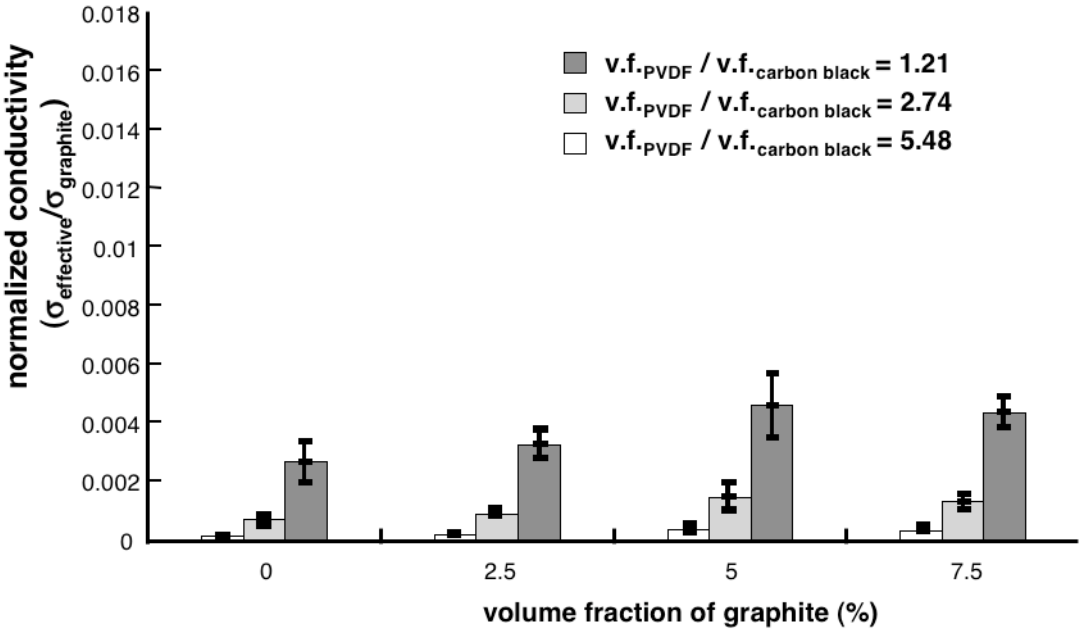

Figure 2.7(b): Conductivity of composite $LiMn_2O_4$ with 40% porosity of 40% active material.

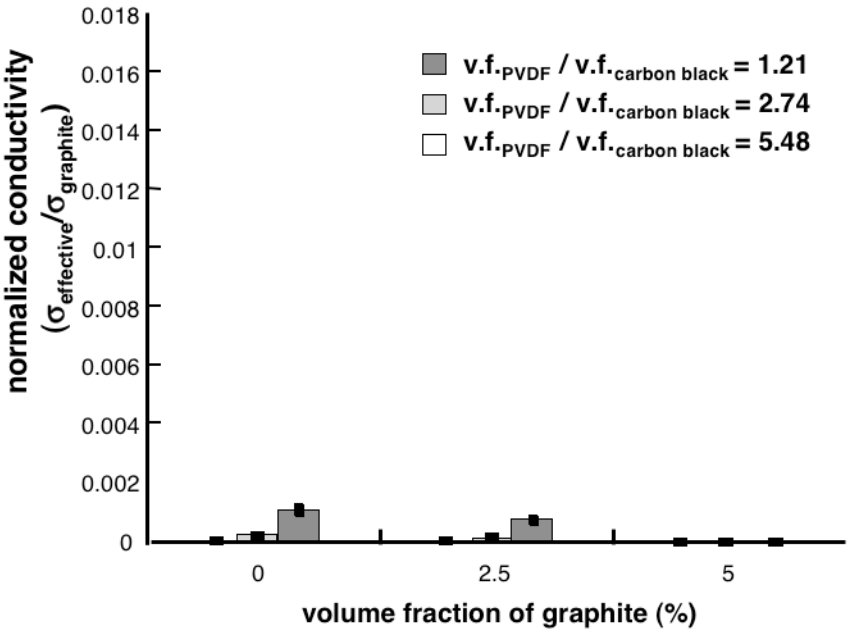

Figure 2.7(c): Conductivity of composite $LiMn_2O_4$ with 40% porosity and 50% active material.

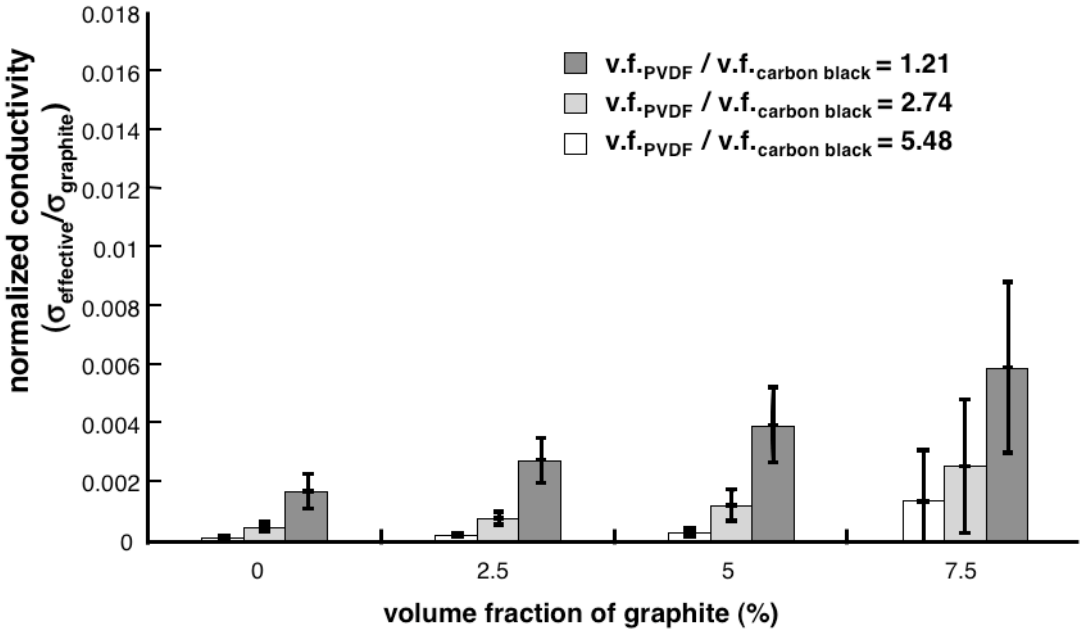

Figure 2.7(d): Conductivity of composite $LiMn_2O_4$ with 50% porosity and 30% active material.

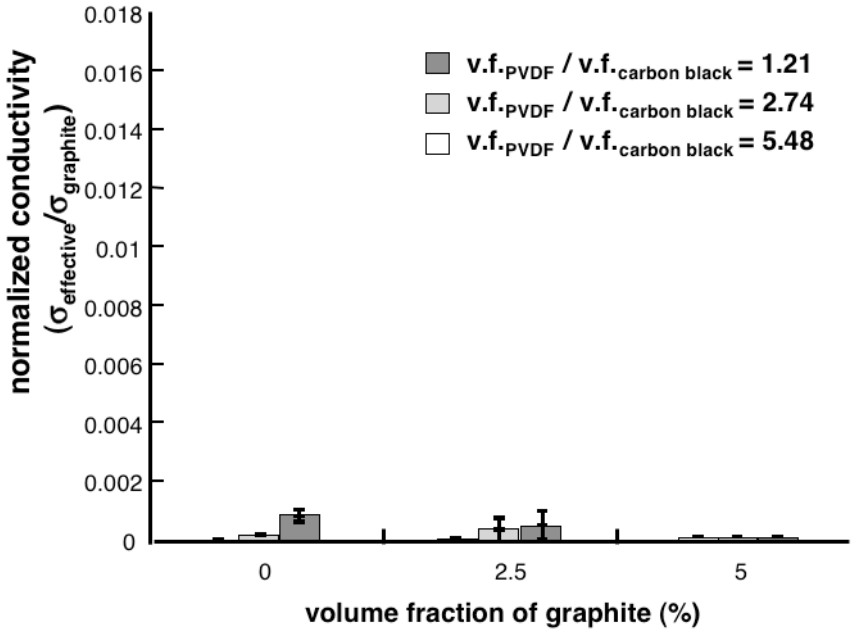

Figure 2.7(e): Conductivity of composite $LiMn_2O_4$ with 50% porosity and 40% active material.

	Porosity = 40%														
	$LiMn_2O_4$ = 30%					$LiMn_2O_4$ = 40%					$LiMn_2O_4$ = 50%				
graphite (%) / PVDF/C	0	2.5	5	7.5	p	0	2.5	5	7.5	p	0	2.5	5	7.5	p
1.21	4.5E-3	5.75E-3	6.77E-3	9.60E-3	$<10^{-4}$	1.94E-3	2.75E-3	3.40E-3	3.79E-3	0.04	1.28E-3	8.82E-4	1.82E-5	-	$<10^{-4}$
2.74	1.21E-3	1.62E-3	1.96E-3	2.93E-3	$<10^{-4}$	5.23E-4	7.64E-4	9.92E-4	1.08E-3	0.05	3.46E-4	2.40E-4	5.06E-6	-	$<10^{-4}$
5.48	2.59E-4	3.52E-4	4.30E-4	6.65E-4	$<10^{-4}$	1.12E-4	1.67E-4	2.20E-4	2.36E-4	0.01	7.38E-5	5.13E-5	1.21E-6	-	$<10^{-4}$
p	0.002	$<10^{-4}$	$<10^{-4}$	$<10^{-4}$		0.001	$<10^{-4}$	0.001	$<10^{-4}$		$<10^{-4}$	$<10^{-4}$	0.3	-	

(a)

	Porosity = 50%									
	$LiMn_2O_4$ = 30%					$LiMn_2O_4$ = 40%				
graphite (%) / PVDF/C	0	2.5	5	7.5	p	0	2.5	5	7.5	p
1.21	1.57E-3	2.94E-3	5.16E-3	9.24E-3	0.06	1.12E-3	8.56E-4	2.28E-4	-	0.05
2.74	4.23E-4	8.18E-4	1.75E-3	5.12E-3	0.2	3.02E-4	2.34E-4	6.33E-5	-	0.2
5.48	9.04E-5	1.77E-4	4.42E-4	3.55E-3	0.4	6.46E-5	5.02E-5	1.37E-5	-	0.2
p	0.003	0.001	0.003	0.1		$<10^{-4}$	0.4	0.3	-	

(b)

Table 2.5: Simulation results and two-way statistical analyses of the simulation data in terms of p values of normalized conductivity of composite $LiMn_2O_4$ with (a) 40% porosity and (b) 50% porosity.

	Porosity = 40%														
	$LiFePO_4$ = 30%					$LiFePO_4$ = 40%					$LiFePO_4$ = 50%				
graphite (%) / PVDF/C	0	2.5	5	7.5	p	0	2.5	5	7.5	p	0	2.5	5	7.5	p
1.21	2.22E-3	2.88E-3	7.84E-3	1.47E-2	0.05	2.45E-3	3.41E-3	4.70E-3	6.49E-3	0.005	8.92E-4	7.19E-4	6.68E-5	-	0.002
2.74	6.01E-4	7.97E-4	2.40E-3	5.80E-3	0.05	6.64E-4	9.50E-4	1.38E-3	2.26E-3	0.06	2.45E-4	2.09E-4	5.86E-5	-	0.004
5.48	1.30E-4	1.74E-4	5.53E-4	1.89E-3	0.02	1.46E-4	2.13E-4	3.23E-4	6.17E-4	0.3	5.68E-5	5.64E-5	3.35E-5	-	0.03
p	0.02	0.005	$<10^{-4}$	0.03		$<10^{-4}$	$<10^{-4}$	$<10^{-4}$	0.07		0.002	$<10^{-4}$	$<10^{-4}$	-	

(a)

	Porosity = 50%									
	$LiFePO_4$ = 30%					$LiFePO_4$ = 40%				
graphite (%) / PVDF/C	0	2.5	5	7.5	p	0	2.5	5	7.5	p
1.21	2.54E-3	2.25E-3	3.70E-3	6.64E-3	0.2	9.75E-4	6.04E-4	5.43E-4	-	0.03
2.74	6.87E-4	6.20E-4	1.06E-3	3.05E-3	0.3	2.66E-4	1.68E-4	1.86E-4	-	0.1
5.48	1.50E-4	1.37E-4	2.41E-4	1.05E-3	0.3	6.01E-5	4.07E-5	6.56E-5	-	1
p	0.02	0.001	0.003	0.04		$<10^{-4}$	0.002	0.001	-	

(b)

Table 2.6: Simulation results and two-way statistical analyses of the simulation data in terms of p values of normalized conductivity of composite $LiFePO_4$ with (a) 40% porosity and (b) 50% porosity.

	Porosity = 40%														
	$Li(Ni_{0.8}Co_{0.15}Al_{0.05})O_2$ = 30%					$Li(Ni_{0.8}Co_{0.15}Al_{0.05})O_2$ = 40%					$Li(Ni_{0.8}Co_{0.15}Al_{0.05})O_2$ = 50%				
graphite (%) / PVDF/C	0	2.5	5	7.5	p	0	2.5	5	7.5	p	0	2.5	5	7.5	p
1.21	4.03E-3	5.48E-3	7.81E-3	1.21E-2	0.001	2.09E-3	3.26E-3	3.87E-3	3.75E-3	0.1	1.24E-3	9.47E-4	1.18E-4	-	$<10^{-4}$
2.74	1.09E-3	1.54E-3	2.32E-3	4.34E-3	0.002	5.64E-4	8.94E-4	1.10E-3	1.14E-3	0.2	3.34E-4	2.63E-4	4.11E-5	-	$<10^{-4}$
5.48	2.33E-4	3.33E-4	5.28E-4	1.22E-3	0.005	1.21E-4	1.93E-4	2.42E-4	2.69E-4	0.4	7.18E-5	5.80E-5	1.51E-5	-	$<10^{-4}$
p	$<10^{-4}$	$<10^{-4}$	$<10^{-4}$	$<10^{-4}$		$<10^{-4}$	$<10^{-4}$	0.1	0.003		$<10^{-4}$	$<10^{-4}$	0.2	-	

(a)

	Porosity = 50%									
	$Li(Ni_{0.8}Co_{0.15}Al_{0.05})O_2$ = 30%					$Li(Ni_{0.8}Co_{0.15}Al_{0.05})O_2$ = 40%				
graphite (%) / PVDF/C	0	2.5	5	7.5	p	0	2.5	5	7.5	p
1.21	1.92E-3	3.30E-3	2.62E-3	6.34E-3	0.005	1.13E-3	9.93E-4	1.67E-4	-	$<10^{-4}$
2.74	5.19E-4	9.65E-4	7.39E-4	2.26E-3	0.009	3.06E-4	2.71E-4	5.08E-5	-	$<10^{-4}$
5.48	1.11E-4	2.17E-4	1.61E-4	5.85E-4	0.02	6.56E-5	5.87E-5	1.49E-5	-	0.001
p	$<10^{-4}$	$<10^{-4}$	$<10^{-4}$	0.001		0.001	$<10^{-4}$	$<10^{-4}$	-	

(b)

Table 2.7: Simulation results and two-way statistical analyses of the simulation data in terms of p values of normalized conductivity of composite $Li(Ni_{0.8}Co_{0.15}Al_{0.05})O_2$ with (a) 40% porosity and (b) 50% porosity.

	Porosity = 40%														
	$Li(Ni_{1/3}Co_{1/3}Mn_{1/3})O_2$ = 30%					$Li(Ni_{1/3}Co_{1/3}Mn_{1/3})O_2$ = 40%					$Li(Ni_{1/3}Co_{1/3}Mn_{1/3})O_2$ = 50%				
graphite (%) / PVDF/C	0	2.5	5	7.5	p	0	2.5	5	7.5	p	0	2.5	5	7.5	p
1.21	3.94E-3	5.62E-3	6.31E-3	8.99E-3	0.006	3.06E-3	3.51E-3	5.16E-3	4.24E-3	0.001	1.25E-3	8.41E-4	3.04E-7	-	0.8
2.74	1.06E-3	1.59E-3	1.87E-3	3.09E-3	0.003	8.26E-4	9.70E-4	1.55E-3	1.30E-3	0.001	3.37E-4	2.29E-4	2.94E-7	-	0.5
5.48	2.27E-4	3.46E-4	4.24E-4	8.23E-4	0.004	1.76E-4	2.09E-4	3.53E-4	2.92E-4	0.001	7.20E-5	4.91E-5	2.60E-7	-	0.4
p	0.001	$<10^{-4}$	$<10^{-4}$	$<10^{-4}$		$<10^{-4}$	$<10^{-4}$	$<10^{-4}$	$<10^{-4}$		$<10^{-4}$	$<10^{-4}$	1	-	

(a)

	Porosity = 50%									
	$Li(Ni_{1/3}Co_{1/3}Mn_{1/3})O_2$ = 30%					$Li(Ni_{1/3}Co_{1/3}Mn_{1/3})O_2$ = 40%				
graphite (%) / PVDF/C	0	2.5	5	7.5	p	0	2.5	5	7.5	p
1.21	2.38E-3	3.97E-3	3.97E-3	4.95E-3	0.01	5.86E-4	1.03E-3	6.98E-5	-	0.002
2.74	6.43E-4	1.12E-3	1.13E-3	1.60E-3	0.01	1.58E-4	2.86E-4	1.92E-5	-	0.002
5.48	1.37E-4	2.43E-4	2.49E-4	3.77E-4	0.01	3.38E-5	6.17E-5	4.22E-5	-	0.002
p	0.008	$<10^{-4}$	0.001	$<10^{-4}$		0.004	$<10^{-4}$	$<10^{-4}$	-	

(b)

Table 2.8: Simulation results and two-way statistical analyses of the simulation data in terms of p values of normalized conductivity of composite $Li(Ni_{1/3}Co_{1/3}Mn_{1/3})O_2$ with (a) 40% porosity and (b) 50% porosity.

The statistical analysis results in Tables 2.5 to 2.8 show that volume fraction of graphite is significant for conductivity in some cases with 30% active material. For example, in Table 2.7(a), with 40% porosity, 30% active material, and PVDF/C of 1.21, the p value of 0.001 denotes the significant effect of increase in the volume fraction of graphite on the normalized conductivity. For this composition, the normalized conductivity increases from 4.03×10^{-3} to 1.21×10^{-2} with an increase in graphite from 0 to 7.5%.

The statistical analysis results in Tables 2.5 to 2.8 show that the ratio of PVDF to carbon black is the most significant factor affecting conductivity. Values of $p < 0.05$ can be seen in almost every row in Tables 2.5 to 2.8. For example, in Table 2.6(a), with 40% porosity, 30% active material, and 2.5% graphite, the p value of 0.005 indicates the significant effect of increase in the volume ratio of PVDF to carbon black on the normalized conductivity. In this composition, the normalized conductivity increases from 1.74×10^{-4} to 2.28×10^{-3} with a reduction in volume ratio from 5.48 to 1.21.

Indeed, addition of graphite actually reduces conductivity, when the PVDF coating is penalized for the addition of graphite. For example, in Table 2.7(a), with 40% porosity, 50% active material, and PVDF/C of 1.21, a $p < 10^{-4}$ denotes the significant effect of increase in the volume fraction of graphite on the normalized conductivity. In this composition, the normalized conductivity decreases from 1.24×10^{-3} to 1.18×10^{-4} with increase in graphite from 0 to 5%; meanwhile, because of increase in graphite, carbon black decreases from 4.51% to 2.26%, and PVDF decreases from 5.49% to 2.74%. The effect of reduction of conductivity can be found in cases with 40% porosity, 50% active material shown in Table 2.5(a), Table 2.6(a), and Table 2.7(a).

DISCUSSION

Simulations of the computational intensity described here must necessarily represent rather small volumes; thus, examination of size effect is critical. Prior studies of overlapping [29] and nonoverlapping [50] spherical particles have shown that the error due to size effect of the domain is negligible for the ratio L/d (domain length to particle diameter) > 2.5. The error in determination of effective properties was specifically found to be <1.8% for a periodic elastic composite with a disordered unit cell of a random dispersion of nonoverlapping identical spheres [50], a similar system to simulations presented here. In all simulations here, the ratio of L/d>3.3 was used, to prevent any introduction of error.

Differences in arrangements of statistically similar structures, along with contrast ratios of properties in phases, result in variances in predicted, effective properties in heterogeneous materials. These increased variances can be explained in terms of percolation of phases in each case. Because achievement of percolation is probabilistic in finite volumes, resulting conductivity is typically highly variable, close to the percolation point. Here, results showed highest variability at the closest value to the percolation point studied for graphite (7.5% for the present study; as compared to 10% being the theoretical percolation point for particles with an aspect ratio of 7.4 [29]).

Increasing the volume fraction of carbon black and PVDF appears to be the best strategy in improving overall conductivity, for the materials and ranges of volume fractions studied. Active material particles, made conductive with a coating of carbon black and PVDF, achieved percolation because the volume fraction in studied cases (≥30%) was larger than the percolation threshold (29%) for a 3D spherical particulate

system [29]. This loading scheme can be thought of as achieving percolation in a system of hollow, conductive spheres, with the path of least resistance of electrons through the coating.

Clearly, there is an important tradeoff in considering the type of additive to use. It is advantageous to use highly conductive surface coatings, versus using larger particle conductive additives dispersed among active material particles, in many ranges studied. As demonstrated by calculated p values in Tables 2.5 to 2.8, increasing the thickness of coatings improves conductivity for all cases studied, with the exception of cases with 40% porosity, 50% active material, and 5% graphite, as shown in Table 2.5(a), Table 2.7(a), and Table 2.8(a). In these cases, the coating thickness amounted to only 0.082 μm, 0.091 μm, and 0.097 μm respectively, or 0.92%, 0.89%, and 0.87% respectively of the diameter of a typical active material particle. It seems likely that imperfections in coatings for these thin layers would substantially reduce the conductivity of the surface, and therefore fail to create a percolated network of spheres. Improvements from addition of larger particle conductive additives is only obvious in cases with 40% porosity and 30% active material for the four active material systems, and cases with 50% porosity and 30% active material for $Li(Ni_{0.8}Co_{0.15}Al_{0.05})O_2$ and $Li(Ni_{1/3}Co_{1/3}Mn_{1/3})O_2$ systems.

In Table 2.9, we compared the effective conductivity of two different loading schemes around active material particle. In both loading schemes, the PVDF/carbon black composite coating was included. From this table, we see that addition of a carbon nanofilm coating around active material particles does not significantly improve laminate conductivity. Moreover, binder is required to maintain structural integrity of the composite electrode, regardless of other additives or treatments. Because of the relatively

active material	$LiFePO_4$ with nanofilm coating	$LiFePO_4$ without nanofilm coating
bulk conductivity (S/m)	5.91×10^{-1}	10^{-9}
normalized effective conductivity	1.47×10^{-2}	1.16×10^{-2}

Table 2.9: Comparison between $LiFePO_4$ with and without nanofilm coating; cathode system with 30% active material, 40% porosity, 7.5% graphite, 10.15% carbon black, and 12.35% PVDF.

low conductivity of the binder, carbon black addition seems a reasonable way of improving conduction.

BIBLIOGRAPHY

1. K. Ozawa, Lithium-ion rechargeable batteries with $LiCoO_2$ and carbon electrodes: the $LiCoO_2$/C system, Solid State Ionics, Diffusion & Reactions, 69, 212-21 (1994).

2. C. Delmas and I. Saadoune, Electrochemical and physical properties of the $Li_xNi_{1-y}Co_yO_2$ phases, Solid State Ionics, 53-56, 370-375 (1992).

3. C. Delmas, I. Saadoune, and A. Rougier, The cycling properties of the $Li_xNi_{1-y}Co_yO_2$ electrode, Journal of Power Sources, 44 (1-3), 595-602 (1993).

4. A. Rougier, I. Saadoune, P. Gravereau, P. willmann, C. Delmas, Effect of cobalt substitution on cationic distribution in $LiNi_{1-y}Co_yO_2$ electrode materials, Solid State Ionics, 90 (1-4), 83-90 (1996).

5. J. R. Dahn, W. W. Fuller, M. Obrovac, and U. von Sacken, Thermal stability of Li_xCoO_2, Li_xNiO_2 and λ-MnO_2 and consequences for the safety of Li-ion cells, Solid State Ionics, 69 (3-4), 265-70 (1994).

6. Z. Zhang, D. Fouchard, and J. R. Rea, Differential scanning calorimetry material studies: implications for the safety of lithium-ion cells, Journal of Power Sources, 70 (1), 16-20 (1998).

7. Z. Liu, J. Y. Lee, and H. J. Linder, Effects of conducting carbon on the electrochemical performance of $LiCoO_2$ and $LiMn_2O_4$ cathodes, Journal of Power Sources, 97-98, 361-365 (2001).

8. R. Dominko, M. Gaberscek, J. Drofenik, M. Bele, and S. Pejovnik, A novel coating technology for preparation of cathodes in Li-ion batteries, Electrochemical and Solid-State Letters, 4 (11), 187-190 (2001).

9. S. Mandal, J. M. Amarilla, J. Ibanez, and J. M. Rojo, The role of carbon black in $LiMn_2O_4$-based composites as cathodes for rechargeable lithium batteries, Journal of Electrochemical Society, 148, A24-A29 (2001).

10. A. Momchilov, A. Trifonova, B. Banov, B. Pourecheva, and A. Kozawa, Nonaqueous UFC suspensions, used as conductive additive in cathodes for lithium batteries, Journal of Power Sources, 81-82, 566-570 (1999).

11. A. S. Skapin, M. Gaberscek, R. Dominko, M. Bele, J. Drofenik, and J. Jamnik, Detection of highly conductive pathways in $LiMn_2O_4$-carbon black composites for Li ion batteries by microcontact impedance spectroscopy, Solid State Ionics, 167, 229-235 (2004).

12. M. G. Lazarraga, S. Mandal, J. Ibanez, J. M. Amarila, and J. M. Rojo, $LiMn_2O_4$-based composites processed by a chemical-route microstructural, electrical,

electrochemical, and mechanical characterization, Journal of Power Sources, 115, 315-322 (2003).

13. S. L. Bewlay, K. Konstantinov, G. X. Wang, S. X. Dou, and H. K. Liu, Conductivity improvements to spray-produced $LiFePO_4$ by addition of a carbon source, Materials Letters, 58, 1788-1791 (2004).

14. K. Zaghib, J.Shim, A. Guerfi, P. Charest, and K. A. Striebel, Effect of carbon source as additives in $LiFePO_4$ as positive electrode for lithium-ion batteries, Electrochemical and Solid-State Letters, 8, A207-210 (2005).

15. C. M. Julien, K. Zaghib, A. Mauger, M. Massot, A. Massot, A. Ait-Salah, M. Selmane, F. Gendron, Characterization of the carbon coating onto $LiFePO_4$ particles used in lithium batteries, Journal of Applied Physics, 100 (6), 63511-1-7 (2006).

16. C.-W. Wang, A. M. Sastry, K. A. Striebel, and K. Zaghib, Extraction of layerwise conductivities in carbon-enhanced, multilayered $LiFePO_4$ cathodes, Journal of The Electrochemical Society, 152 (5), A1001-A1010 (2005)

17. R. J. Gummow, A. de Kock, M. M. Thackeray, Improved capacity retention in rechargeable 4 V lithium/lithium-manganese oxide (spinel) cells, Solid State Ionics, 69 (1), 59-67 (1994).

18. J. P. Tu, H. M. Wu, X. T. Chen, Y. Li, X. B. Zhao, G. S. Cao, Electrochemical study on $LiMn_2O_4$ as cathode material for lithium ion batteries, Journal of Electroanalytical Chemistry, 8 (2), 113-128 (2006).

19. A. K. Padhi, K. S. Nanjundaswamy, C. Masquelier, and J. B. Goodenough, metal redox energies in phosphates with NASICON structure by lithium intercalation, Journal of The Electrochemical Society, 144, 2581-2586 (1997).

20. C. H. Mi, X. G. Zhang, X. B. Zhao, and H. L. Li, Effect of sintering time on the physical and electrochemical properties of $LiFePO_4$/C composite cathodes, Journal of Alloys and Compounds, 424 (1-2), 327-333 (2006).

21. S.-W. Song, G. V. Zhuang, and P. N. Ross, Jr., Surface film formation on $LiNi_{0.8}Co_{0.15}Al_{0.05}O_2$ cathodes using attenuated total reflection IR spectroscopy, Journal of The Electrochemical Society, 151 (8), A1162-A1167 (2004).

22. I. Belharouak, D. Vissers, K. Amine, Thermal stability of the $Li(Ni_{0.8}Co_{0.15}Al_{0.05})O_2$ cathode in the presence of cell components, Journal of The Electrochemical Society, 153 (11), A2030-A2035 (2006).

23. Z. Lu and J. R. Dahn, The effect of Co substitution for Ni on the structure and electrochemical behavior of T2 and O2 structure $Li_{2/3}[Co_xNi_{1/3-x}Mn_{2/3}]O_2$, Journal of The Electrochemical Society, 148 (3), 237-240 (2001).

24. P. He, H. Wang, L. Qi, T. Osaka, Electrochemical characteristics of layered $LiNi_{1/3}Co_{1/3}Mn_{1/3}O_2$ and with different synthesis conditions, Journal of Power Source, 160 (1) 627-632 (2006).

25. K. Zaghib, P. Charest, A. Guerfi, J. Shim, M. Perrier, and K. Striebel, Safe Li-ion polymer batteries for HEV applications, Journal of Power Sources, 134 (1), 124-129 (2004).

26. J. Quintanilla and S. Torquato, Clustering properties of d-dimensional overlapping spheres, Physical Review E, 54 (5), 5331-5339 (1996).

27. J. Quintanilla and S. Torquato, Clustering in a continuum percolation model, Advances in Applied Probability, 29 (2), 327-336 (1997).

28. Y. -B. Yi and A. M. Sastry, Analytical approximation of the two-dimensional percolation threshold for fields of overlapping ellipses, Physical Review E, 66, 066130-1-066130-8 (2002).

29. Y. -B. Yi and A. M. Sastry, Analytical approximation of the percolation threshold for overlapping ellipsoids of revolution, Proceedings of the Royal Society of London, Series A, 460, 2353-2380 (2004).

30. C. -W. Wang, K. A. Cook, and A. M. Sastry, Conduction in multiphase particulate/fibrous networks: simulations and experiments on Li-ion anodes, Journal of The Electrochemical Society, 150 (3), A385-A397 (2003).

31. C. -W. Wang, A. M. Sastry, K. A. Striebel, and K. Zaghib, Extraction of layerwise conductivities in carbon-enhanced, multilayered $LiFePO_4$ cathodes, Journal of The Electrochemical Society, 152 (5), A1001-A1010 (2005).

32. Y. -B. Yi, C. -W. Wang, and A. M. Sastry, Compression of packed particulate systems: simulations and experiments in graphitic Li-ion anodes, Journal of Engineering Materials and Technology, 128, 73-80 (2006).

33. J. Moskon, R. Dominko, M. Gaberscek, R. Cerc-Korosec, and J. Jamnik, Citrate-derived carbon nanocoatings for poorly conducting cathode, Journal of The Electrochemical Society, 153, (10), A1805-1811 (2006).

34. http://www.matweb.com (date: 05/31/2006).

35. J. Guan and M. Liu, Transport properties of $LiMn_2O_4$ electrode materials for lithium-ion batteries, Solid State Ionics, 110, 21-28 (1998).

36. S. -Y. Chung, J. T. Bloking, Y. -M. Chiang, Electronically conductive phospho-olivines as lithium storage electrodes, Nature Materials, 1 (2), 123-128 (2002).

37. P. Meakin and R. Jullien, Restructure effects in the rain model for random deposition, Journal of Physics, 48, 1651–1687 (1987).

38. L. Liu and Y. Yuan, Dynamic simulation of powder compact by random packing of monosized and polydisperse particles, Journal of Materials Science Letters, 19 (10), 841-843 (2000).

39. G. Fu, and W, Dekelbab, 3-D random packing of polydisperse particles and concrete aggregate grading, Powder Technology, 133, 147-155 (2003).

40. E. Santiso and E. A. Muller, Dense packing of binary and polydisperse hard spheres, Molecular Physics, 100, 2461-2469 (2002).

41. V. Falk, and U. D'Ortona, A polydisperse sedimentation and polydisperse packing model, Powder Technology, 128, 229-235 (2002).

42. N. V. Kosova, N. F. Uvarov, E. T. Devyatkina, E. G. Avvakumov, Mechanical synthesis of $LiMn_2O_4$ cathode material for lithium batteries, Solid State Ionics, 135, 107-114 (2000).

43. J. Molenda, K. Swierczek, M. Molenda, and J. Marzec, Electronic structure and reactivity of $Li_{1-x}Mn_2O_4$ cathode, Solid State Ionics, 135, 53-59 (2000).

44. P. B. Joshi and P. Ramakrishnan, Materials for Electrical and Electronic Contacts, p. 90-91, Science Publishers, Enfield (2004).

45. F. M. Smits, Measurement of sheet resistivities with the 4-point probe, Bell System Technical Journal, 37 (3), 711-718 (1958).

46. D. A. G. Bruggeman, Berechnung verschiedener physikalischer konstanten von heterogenen substanzen, Annalen der Physik, 24, 636-664 (1935).

47. D. Guy, B. Lestriez, R. Bouchet, and D. Guyomard, Critical role of polymeric binders on the electronic transport properties of composites electrode, Journal of The Electrochemical Society, 153 (4), A679-A688 (2006).

48. ABAQUS/STANDARD v.6.6, ABAQUS, Inc., Providence, RI.

49. SPSS v.13, SPSS Inc., Chicago, IL.

50. A. A. Gusev, Representative volume element size for elastic composites: a numerical study, Journal of the Mechanics and Physics of Solids, 45(9), 1449-1459 (1997).

CHAPTER III

POROUS CATHODE OPTIMIZATION FOR LITHIUM CELLS: IONIC AND ELECTRONIC CONDUCTIVITY, CAPACITY, AND SELECTION OF MATERIALS[1]

INTRODUCTION

A key culprit in limiting performance of Li-ion cells is inadequate conductivity, both electronic and ionic. Presently, the gap between actual and theoretical capacities in leading Li-based technologies are 32.3%, 31.9% and 38.1% in $LiFePO_4$, $Li(Ni\text{-}Co_{0.15}Al_{0.05})O_2$ and $Li(Ni_{1/3}Co_{1/3}Mn_{1/3})O_2$ respectively [1,2,3]. The relationship between electronic and ionic conductivity is also problematic, absent mathematical optimization, because an increase in one generally penalizes the other. Porous electrodes, used in numerous industrial applications due to high achievable reaction rates, including Li batteries [4], must balance these needs.

Individually, various parameters have been examined for improving cell performance. Adjustments in form factor [5,6,7], cathode particle size [8,9,10,11,12], porosity and thickness of the cathode electrode and separator [13], electrolyte concentration [13], loading schema for conductive additives [14,15,16,17,18,19], and cathode particle arrangement [20] have all been shown to improve performance. Among

[1] Material in this chapter is a unpublished paper in progress: Y. -H. Chen, C. -W. Wang, X. Zhang, and A. M. Sastry, Cathode optimization for lithium cells: ionic and electronic conductivity, capacity, and selection of materials, *Journal of the Electrochemical Society* (2008).

these, improvements in transport properties, ionic and electronic conductivity, have been empirically shown to have the greatest effect. To date, however, no comprehensive numerical study has been reported which studies the optimization of these parameters via addition of conductive materials.

Continuum, porous electrode models [13,21,22,23], equivalent circuit models [24, 25,26], atomistic [27,28], and molecular dynamics models [29,30], have been widely used to model cells. However, these scales of simulations do not directly inform engineering of cathode architecture designs via selection of additives. Few consider ion and electron transport [13,22], and none correlate conductivities to battery performance. Cathode design requires mesoscale simulations with various loading schema, but to date, there is little work in this area [20].

Optimization of battery design will undoubtedly replace sequential testing of various cathodic electrochemistries (i.e. those in Table 1.2). This is the preferred path in better matching theoretical and actual capacity, by selecting combinations of high power and energy density materials. In this study, a numerical, finite element model at the particle scale was applied to simulate porous effective ionic and electronic conductivities in cathodes with additives. Those effective properties were introduced to porous electrode model to simulate the battery performance. Optimization approach, similar to [13], was applied to simplify numerical computation and to make analysis and optimization feasible. Our objectives of this study are as follows:

1) To demonstrate predictive methods of both ionic and electronic conductivity, and to validate predictions of electronic conductivity.

2) To map relationship between the ionic and electronic conductivities with additives.

3) To correlate conductivities to battery performance.

4) To identify optimal schema for high energy $Li(Ni_{1/3}Co_{1/3}Mn_{1/3})O_2$ cells.

METHODS

In prior work [19], we established methods for measurement of conductivity, particle packing algorithms, and finite element analyses for prediction of effective conductivity of cathodes. Here, we investigated both cathode (electronic) and electrolytic (ionic) conductivities; Table 3.1 lists the material properties of electrodes and electrolyte [19,35,36,37] studied. In this research, $Li(Ni_{1/3}Co_{1/3}Mn_{1/3})O_2$ was selected as the active material with PVDF as binder. Graphite and carbon black were used as conductive additives. The mixture of PVDF and carbon black (PVDF/C) was simulated as a coating around the active material and graphite particles, as in prior work [19]. Open spaces were presumed to be filled with electrolyte, i.e. LiPF6 in ethylene carbonate-diethyl carbonate (EC/DEC 1:1 v/v). Cathode compression experiments were used to validate the conduction modeling; validated conductivities were then used in battery performance simulations. After these simulations, optimization approach was used to further analyze and optimize combinations of materials.

EXPERIMENTS

MATERIALS AND COMPRESSION OF CATHODE SYSTEM

Cathode electrode was constructed by combining 81.6 wt % $Li(Ni_{1/3}Co_{1/3}Mn_{1/3})O_2$

parameter	cathode system			electrolyte	anode
material	$Li(Ni_{1/3}Co_{1/3}Mn_{1/3})O_2$	graphite	PVDF/C	$LiPF_6$ (1M) in EC/DEC (1:1)	Li
particle size (μm)	11.04	7.45	-	-	-
mass density (g/cm^3)	4.75	1.95	1.86	1.23	0.53
bulk conductivity (S/m)	1.06×10^{-3}	1.67×10^{4}	760	0.52	1.20×10^{-9}
diffusion coefficient (m^2/s)	- [a]	-	-	1.2×10^{-9}	-
reference	[22]	[37]	[22]	[38,39]	[37]

[a] see Fig. 3.12

Table 3.1:Material properties of cathode system, electrolyte, and anode.

porosity (%)	active material (%)	graphite (%)	carbon black (%)	PVDF (%)	thickness (μm)
50	31.8	3.8	6.1	8.3	200.0
40	38.2	4.6	7.3	10.0	166.7
30	44.5	5.3	8.5	11.6	142.9

Table 3.2: Cathode thickness and volume fraction of active material, graphite, PVDF, and carbon black during compression at different porosity.

(Seimi Chemical), 4 wt % SFG-6 graphite (Timcal), 6.4 wt % acetylene black (Denkon), and 8 wt % PVDF binder (Kureha); fabrication was accomplished in several steps, including a compression and drying sequence. They were fabricated at Lawrence Berkeley National Laboratory by Drs. Battaglia and Gao. Table 3.2 shows cathode thicknesses and the volume fractions of each constituent phase during compression. To construct the cathode, a conductive glue was first made via mixture of acetylene black and PVDF, with a weight ratio of 4:5. The mixture was agitated for 30 minutes at 70% power using a Branson 450 Sonicator, to improve carbon black dispersion. The conductive glue was blended with $Li(Ni_{1/3}Co_{1/3}Mn_{1/3})O_2$ and graphite using Polytron PT10-3S Homogenizer at 3000 to 5000 RPM for 5 minutes. The slurry was poured against a Mitutoyo doctor blade holder, and spread evenly across the blade. The blade was set at a height of 250 μm for casting. Trace NMP solvent was spread on the perforated glass table top of the casting machine; then, an Al foil was overlaid on the material, to serve as a current collector. The Al foil was then held to the glass by vacuum and the trace NMP. The ratio of the height of the blade and the final electrode thickness was set to approximately 3:1 of the final target thickness. The laminate was then dried at 120°C for 12 hours under high vacuum. The cathode was then compressed by rolling and cathode electrodes with assigned porosity were obtained by controlling final cathode thickness.

MEASUREMENT OF ELECTRONIC CONDUCTIVITY

The conductivity of prepared cathode electrode was measured using an inline four-point-probe technique [34]. The same procedure indicated in [34] was adopted here.

In summary, the constant current source was provided from the outer two probes by a Maccor battery test system Series 4000; the voltage difference was measured from the inner two probes by an HP 34401A multimeter; and two different probe spacing distances were used. In each sample, five random points were picked for conductivity measurement.

MICROSTRUCTURE OF CATHODE SYSTEM

FEI Quanta 3D scanning electron microscopy (SEM) was used to observe the microstructure of cathode system. SEM pictures were taken in two different directions of view angles as Fig. 3.1 shows. Specimens for side view were frozen in liquid nitrogen and razor blade was then used to provide a clean cut surface for which to examine the internal microstructure of the material, with minimal shearing.

SIMULATIONS

PACKING ARCHITECTUREA AND CONDUCTION MODELING

The simulations were performed as detail described in [19]. The simulations were used to estimate effective conductivity, effective ionic conductivity, and effective diffusion coefficient. Briefly, the architecture of the composite cathode, comprised of active material, graphite, carbon black, and PVDF, was generated via elastic collision modeling. Periodic boundary conditions were assigned to x-, y-, and z- directions to achieve computational efficiency. The radius of active materials was set to 0.15 of the representative volume; the semi-axes of graphite were dependent upon the size of active materials. The graphite was assumed as a disk-like ellipsoid with aspect ratios a/b, a/c

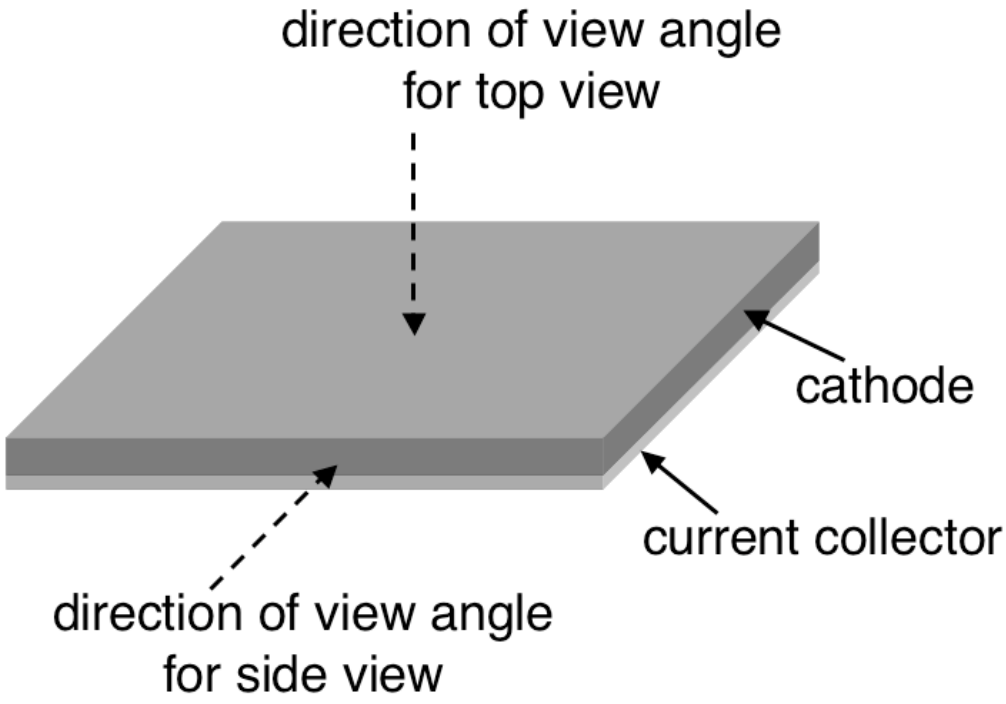

Figure 3.1: Schematic illustration of direction of view angle for SEM.

and b/c (a, b, and c are the length of three semi-axes) set to 1, 7.4 and 7.4, respectively. Finite element meshing was performed using a voxelation method, to prevent mesh-induced singularities. Voxels of 100×100×100 were assigned to the representative volume. A cubic element with each side of 1 unit length enclosing the voxel was generated, with an assigned material property. ABAQUS/STANDARD [35] was used for steady state conduction and diffusion analysis. Effective properties of conduction and diffusion of the representative volume were then calculated by applying potential difference in z- direction. Porous regions were assumed to be fully occupied by the electrolyte phase. Simulation results of solid phase later were compared with experimental results to validate the conductivity simulations. Five simulation realizations were generated for each permutation of conditions studied.

BATTERY PERFORMANCE MODELING

A model Li | $Li(Ni_{1/3}Co_{1/3}Mn_{1/3})O_2$ system with electrolyte EC/DEC (1:1 v/v) and $LiPF_6$ salt was used to evaluate battery performance for various cathode designs. Li-metal was selected as anode electrode to eliminate limited reaction rate in anode. The anode thickness was calculated based on the theoretical capacity provided by cathode, and the capacity ratio of the anode-to-cathode is one. Separator was selected as electrolyte only with 50 μm of thickness. Electrode area was 2.4×10^{-3} m^2. 3C discharge rate was used to meet the plug-in HEV battery goals from United States Council for Automotive Research [36].

This model was modified from 1D porous electrode model coupled with 2D spherical particle diffusion modeling [22, 37]. Effective material properties calculated

from the previous section were introduced in this model. The model includes solid phase electrical conduction using current balance based on Ohm's law, ionic conduction in electrolyte phase, ionic diffusion in electrolyte phase in 1D domain, and ionic diffusion in cathode spherical particles in 2D domain. The governing equations of each region are summarized in Table 3.3, where subscript 1 denotes the solid phase, subscript 2 denotes the electrolyte phase, subscript eff denotes the effective material property, subscript neg denotes the material properties of negative electrode, κ is conductivity, φ is potential, Sa is the specific surface area, j_{loc} is the local current density, R is the gas constant, T is the temperature, F is Faraday's constant, f is the ionic activity factor, D is the diffusion coefficient, t_+ is the cationic transport number, c is the cationic concentration , and r is the radius of the particle. 0.4 is used for cationic transport number in the simulation.

The initial conditions and the boundary conditions are shown in Table 3.4 and Table 3.5 respectively, where i_app is the assigned current density. Bulter-Volmer electrode kinetics were applied at the interfaces of electrode and electrolyte:

$$j_{loc} = i_0 \left\{ \exp\left(\frac{\eta F}{RT} \right) - \exp\left(\frac{-\eta F}{RT} \right) \right\} \tag{19}$$

with

$$\eta = \phi_1 - \phi_2 - E_{ref}(c_{1,surf}) \tag{20}$$

and

$$i_0 = k_0 \sqrt{c_2 (c_{1,\max} - c_{1,surf}) c_{1,surf}} \tag{21}$$

where i_0 is the exchange current density, E_{ref} is the open-circuit potential of the electrode particle, which is a function of c_1 at the surface ($c_{1,surf}$), k_0 is the reaction-rate constant,

region / description	1D domain			2D domain
	anode	separator	cathode	cathode spherical particle
electrical conduction in solid phase	$\nabla\left(-\kappa_{1,avg}\nabla\phi_1\right)=0$ (1)	-	$\nabla\left(-\kappa_{1,eff}\nabla\phi_1\right)=S_a j_{loc}$ (2)	-
ionic conduction in electrolyte phase	-	$\nabla\left\{\begin{matrix}-\kappa_{2,eff}\nabla\phi_2 \\ +\frac{2RT\kappa_{2,eff}}{F}\left[1+\frac{\partial}{\partial c_2}\ln f\right]\left[1-t_+\right]\nabla(\ln c_2)\end{matrix}\right\}=0$ (3)	$\nabla\left\{\begin{matrix}-\kappa_{2,eff}\nabla\phi_2 \\ +\frac{2RT\kappa_{2,eff}}{F}\left[1+\frac{\partial}{\partial c_2}\ln f\right]\left[1-t_+\right]\nabla(\ln c_2)\end{matrix}\right\}=S_a j_{loc}$ (4)	-
ionic diffusion in electrolyte phase	-	$\varepsilon\frac{dc_2}{dt}+\nabla\left\{-D_{2,eff}\nabla c_2\right\}=0$ (5)	$\varepsilon\frac{dc_2}{dt}+\nabla\left\{-D_{2,eff}\nabla c_2\right\}=\frac{S_a j_{loc}(1-t_+)}{F}$ (6)	-
ionic diffusion in solid phase	-	-	-	$r^2\frac{dc_1}{dt}+\nabla\left(-r^2 D_1\nabla c_1\right)=0$ (7)

Table 3.3: Governing equations of each simulated domain: 1D porous electrodes and 2D spherical particle.

region / description	1D domain			2D domain
	anode	separator	cathode	cathode spherical particle
electrical conduction in solid phase	$\phi_1 = 0$ (1-1)	-	$\phi_1 = 4.4$ (2-1)	-
ionic conduction in electrolyte phase	-	$\phi_2 = 0$ (3-1)	$\phi_2 = 0$ (4-1)	-
ionic diffusion in electrolyte phase	-	$c_2 = 2000$ (5-1)	$c_2 = 2000$ (6-1)	-
ionic diffusion in solid phase	-	-	-	$c_1 = 14870$ (7-1)

Table 3.4: Initial conditions of each simulated domain: 1D porous electrodes and 2D spherical particle.

boundary / description	boundary node in 1D domain				boundary line in 2D domain	
	1	2	3	4	cathode surface	other surface
electrical conduction in solid phase	$\phi_1 = 0$ (8)	$-n\bullet\nabla\left(-\kappa_{1,eff}\nabla\phi_1\right)=0$ (9)	$-n\bullet\nabla\left(-\kappa_{1,eff}\nabla\phi_1\right)=0$ (10)	$-n\bullet\nabla\left(-\kappa_{1,eff}\nabla\phi_1\right)=-i\_app$ (11)	-	-
ionic conduction in electrolyte phase	-	$-n\bullet\nabla\left\{\begin{matrix}-\kappa_{2,eff}\nabla\phi_2 \\ +\frac{2RT\kappa_{2,eff}}{F}\left[1+\frac{\partial}{\partial c_2}\ln f\right]\left[1-t_+\right]\nabla(\ln c_2)\end{matrix}\right\}=i\_app$ (12)	-	$-n\bullet\nabla\left\{\begin{matrix}-\kappa_{2,eff}\nabla\phi_2 \\ +\frac{2RT\kappa_{2,eff}}{F}\left[1+\frac{\partial}{\partial c_2}\ln f\right]\left[1-t_+\right]\nabla(\ln c_2)\end{matrix}\right\}=0$ (13)	-	-
ionic diffusion in electrolyte phase	-	$-n\bullet\nabla\left\{-D_{2,eff}\nabla c_2\right\}=\frac{i\_app}{F}$ (14)	-	$\nabla\left\{-D_{2,eff}\nabla c_2\right\}=0$ (15)	-	-
ionic diffusion in solid phase	-	-	-	-	$\nabla\left\{-D_1\nabla c_1\right\}=j_{loc}/F$ (16)	$\nabla\left\{-D_1\nabla c_1\right\}=0$ (17)

Table 3.5: Boundary conditions of each simulated domain: 1D porous electrodes and 2D spherical particle.

and $c_{1,max}$ is the maximum surface concentration. The function of E_{ref} is estimated from discharge-capability plot at 0.09C [37].

OPTIMIZATION OF CONDUCTIVITIES AND BATTERY PERFORMANCE

An optimization approach was introduced to design the cathode system. The cathode thickness was excluded in the variables for conduction modeling because the conduction model only simulates the unit cell of cathode system, which is independent of cathode thickness. Numerical simulations (conduction modeling and battery performance modeling) were conducted at selected points. Electronic and ionic conductivities of cathode electrode, specific energy, specific power, and utilization of simulated battery were included in the objective functions.

RESULTS

Figure 3.2 reports the conductivity measurement and simulation results at different porosity. Experimental results show that a cathode laminate with 50% porosity has a conductivity of 77 S/m. The value decreases slightly to 71 S/m with 40% porosity and increases to 105 S/m with 50% porosity. Simulation results demonstrate the increasing trend of conductivity with cathode compression. The value starts from 59 S/m with 50% porosity increases to 150 S/m with 30% porosity. Fig. 3.3 presents SEM pictures of cathode electrode in side view and top view where active material are light color particles with darker PVDF/C phase. A decrease in porosity can be observed from side view pictures. Besides, distribution of PVDF/C becomes less uniform with decrease

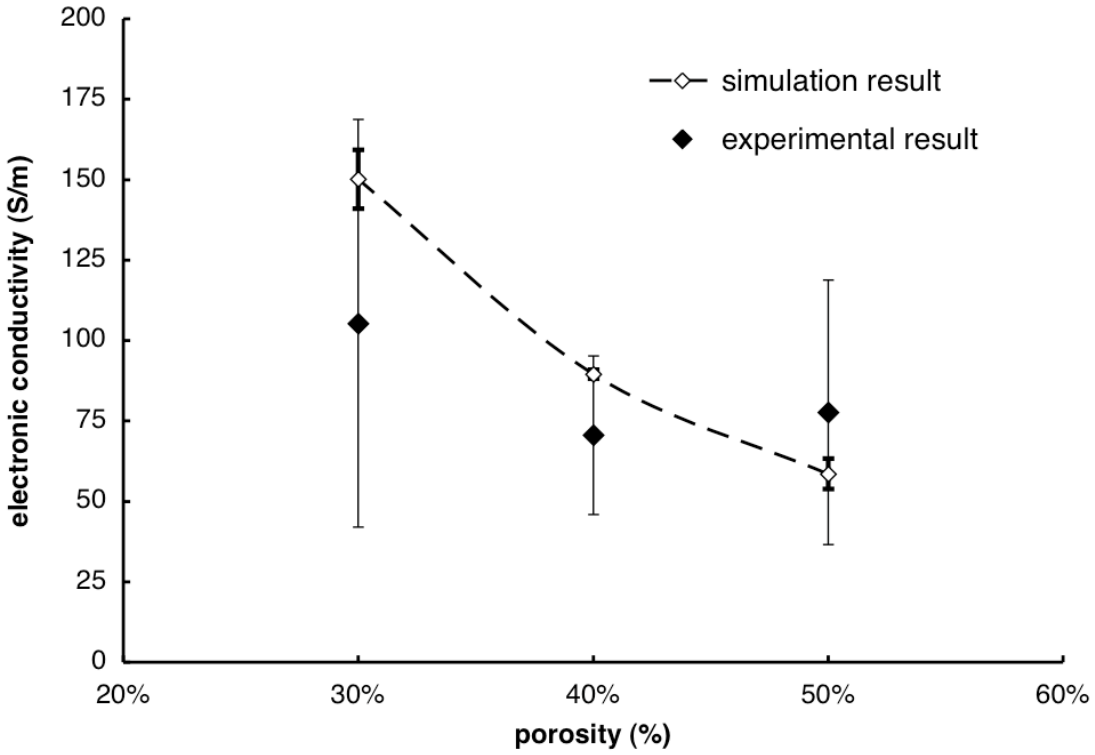

Figure 3.2: Effective electronic conductivity of cathode electrode at different porosity from compression experiments and simulations.

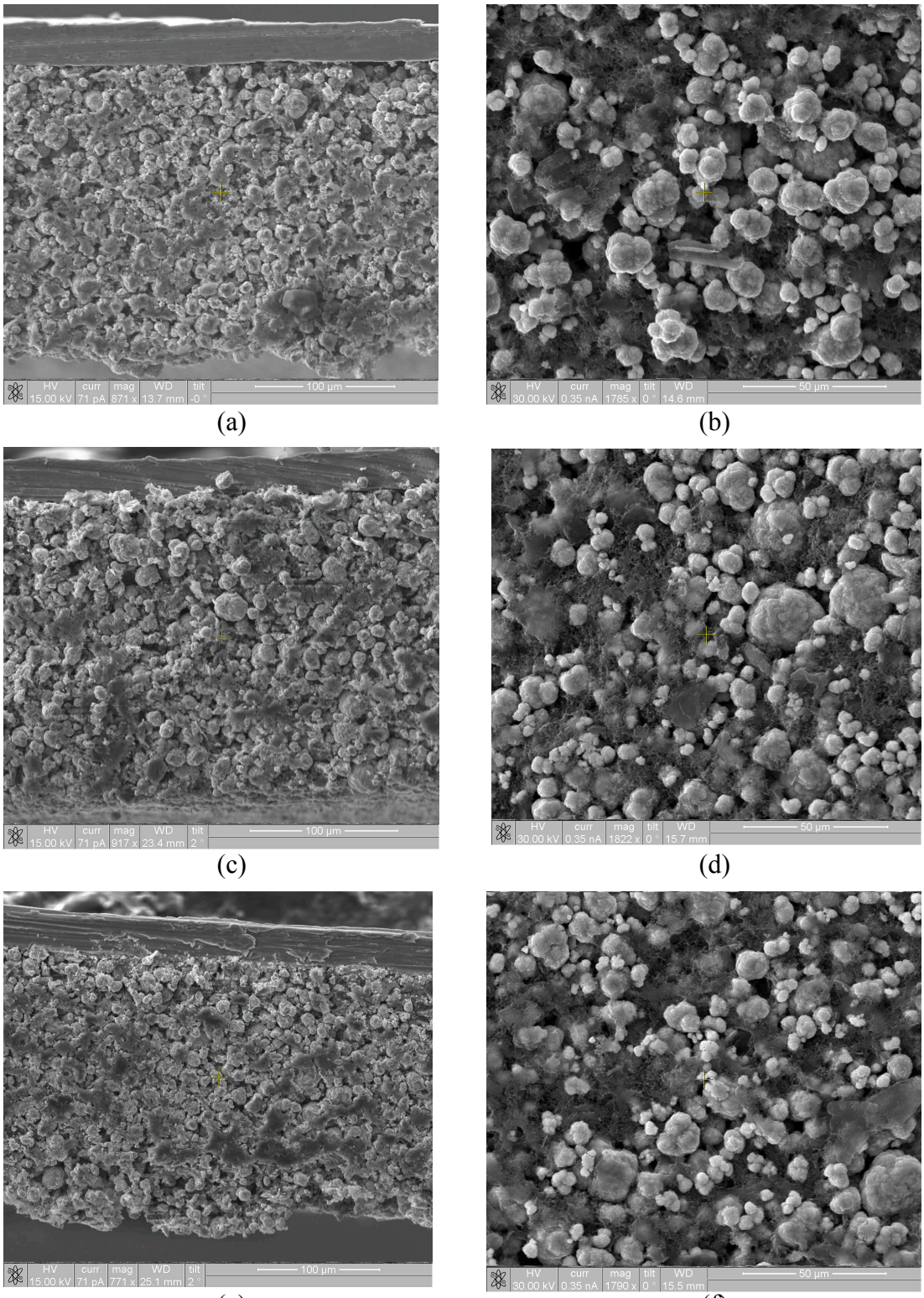

Figure 3.3: SEM pictures of cathode electrodes at (a) 50% porosity side view, (b) 50% porosity top view, (c) 40% porosity side view, (d) 40% porosity top view, (e) 30% porosity side view, (f) 30% porosity top view.

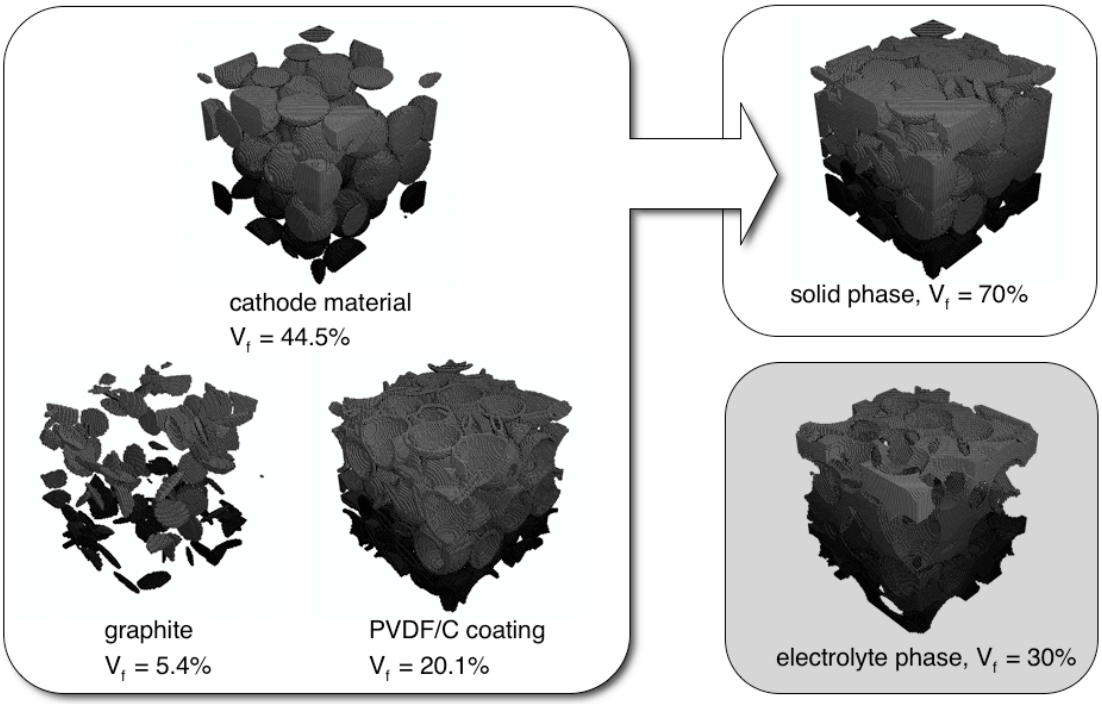

Figure 3.4: Illustration of composition of cathode electrode: complementary solid phase and electrolyte phase.

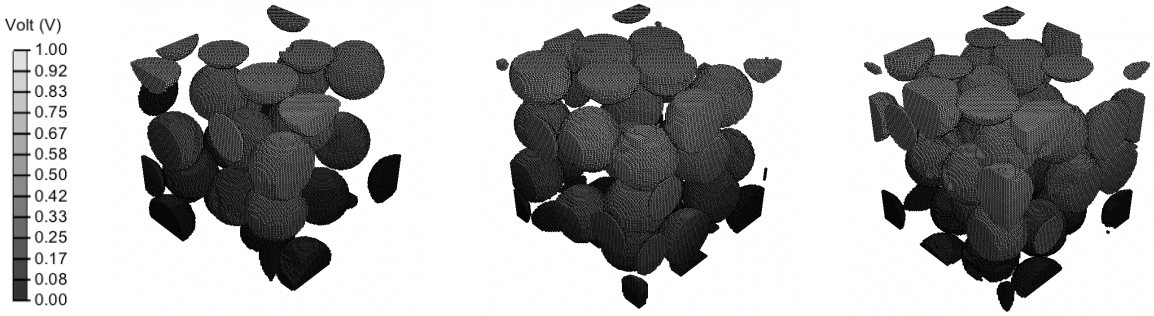

(a) (b) (c)

Figure 3.5: Simulated random structure of cathode material particles at different porosities: (a) 50%, (b) 40%, (c) 30%.

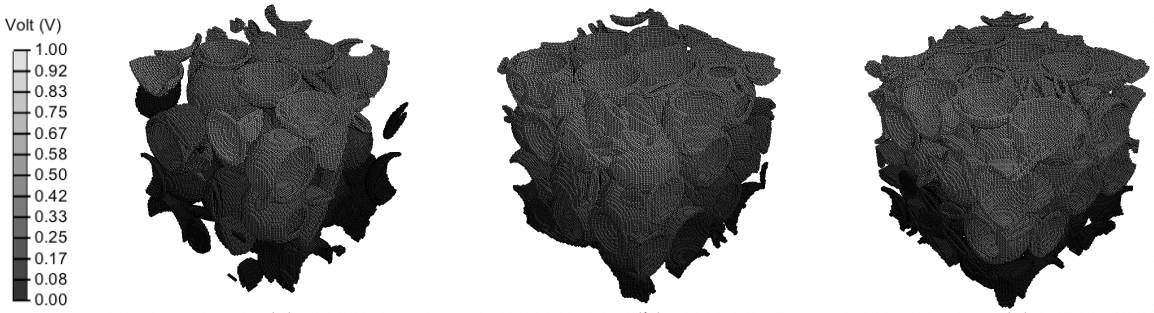

(a) (b) (c)

Figure 3.6: Simulated random structure of PVDF/C at different porosities: (a) 50%, (b) 40%, (c) 30%.

(a) (b) (c)

Figure 3.7: Simulated random structure of graphite at different porosities: (a) 50%, (b) 40%, (c) 30%.

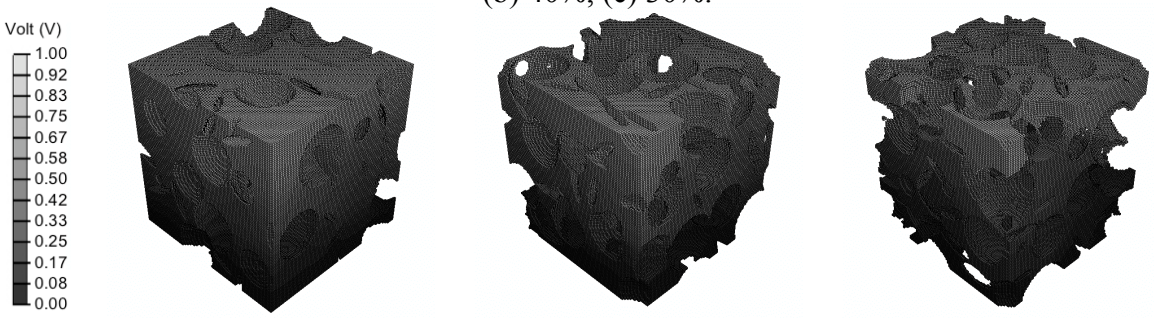

(a) (b) (c)

Figure 3.8: Simulated random structure of electrolyte at different porosities: (a) 50%, (b) 40%, (c) 30%.

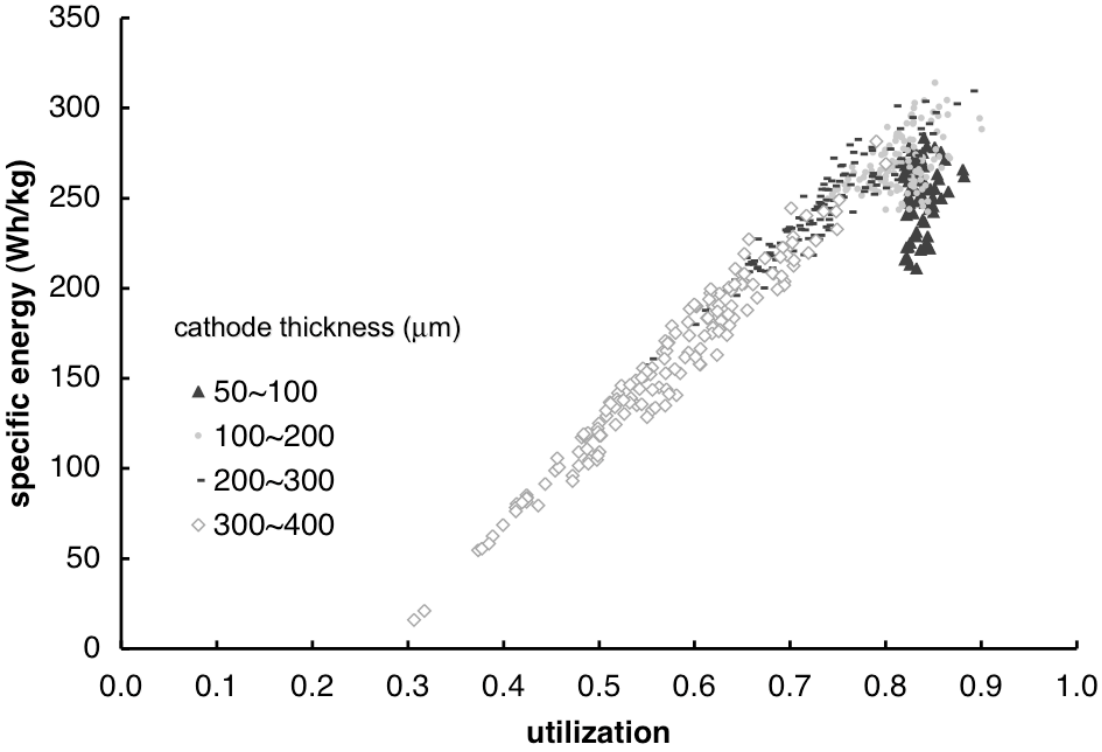

Figure 3.9: Optimization results of specific energy as a function of utilization at different cathode thickness.

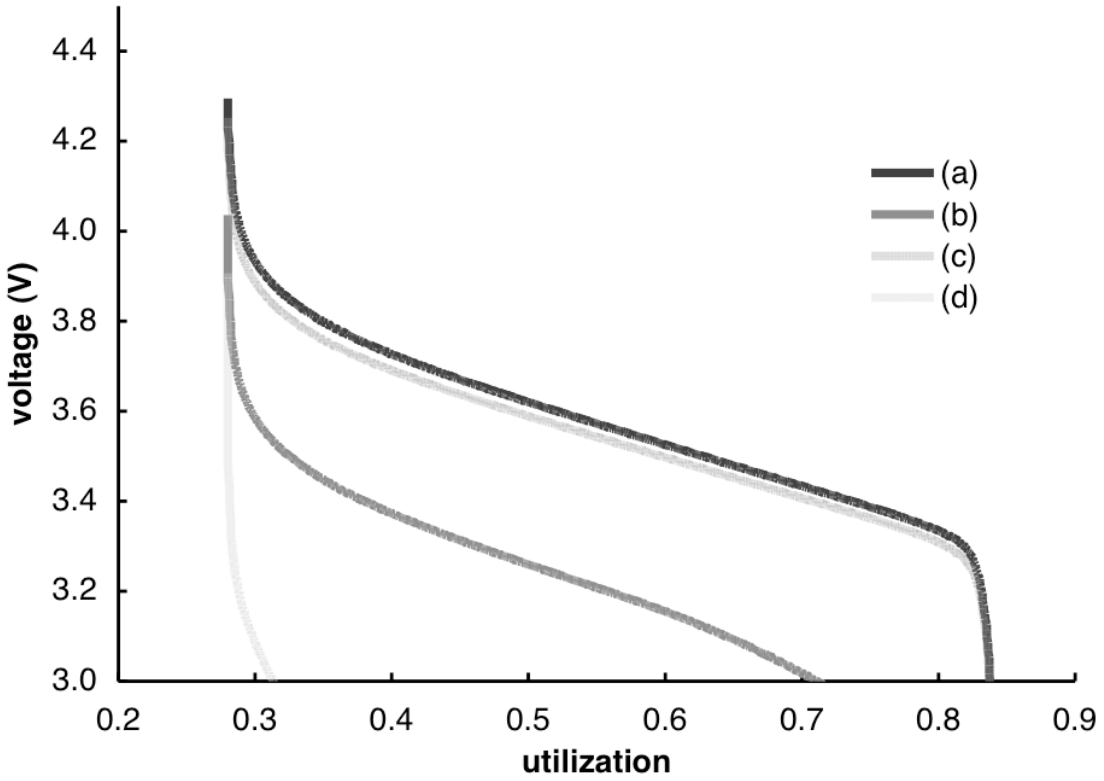

Figure 3.10: Discharge curve generated from battery performance simulation of cathode electrode with 0% graphite, 10% PVDF/C and (a) 30% active material and 50 μm thickness, (b) 30% active material and 400 μm thickness, (c) 45% active material and 50 μm thickness, and (d) 45% active material and 400 μm thickness.

in porosity. Also, with decrease in porosity, it can be seen that more active material particles near top surface are compressed and embedded into PVDF/C phase.

Figure 3.4 illustrates the structural composition of simulated structure of complementary solid phase and electrolyte phase from voxelated finite element conduction model. Solid phase is composed of cathode material, graphite, and PVDF/carbon black coating. Porosity is filled with electrolyte, which completes the representative volume with solid phase. Fig. 3.5-3.8 show the simulated structure of active material, PVDF/carbon coating, graphite, and electrolyte phase respectively at different porosity. Compact structure of solid phase was obtained with decrease in porosity; meanwhile, structure of liquid phase was becoming less dense.

Figure 3.9 shows specific energy as a function of utilization at different cathode thickness range. With cathode thickness larger than 100 μm, specific energy increases from 10 to 320 Wh/kg with increase in utilization from 0.3 to 0.9. For cathode thickness ranging from 50 to 100 μm, specific energy and utilization are also positively related but the result points form another group with lower specific energy and higher utilization. Utilization increases from 0.83 to maximum 0.90 with increase in cathode thickness from 50 to 134 μm, and then decreases to 0.31 with decrease in thickness to 400 μm. Fig. 3.10 illustrates some cases of discharge voltage vs. utilization.

DISCUSSION

Electronic conductivity increases with compression of cathode electrode, though there is a discrepancy between experimental and simulation results. Experimental results with larger standard deviations than simulations might arise from the non-uniformity of

structures introduced by nonuniform mixing process and non-affine compression. This also influences four-point-probe conductivity measurements, which assume homogeneity in each layer. On the other hand, simulated structures based on well-randomized collision realizations, with perfectly coated particles, produced smaller deviations in predicted conductivies.

There is a trade-off between ionic and electronic conductivity; neither best ionic nor best electronic conductivity ensures the highest specific energy. Simulated structural results demonstrate the complementarity of solid and liquid phases. With reductions in porosity, more active material or conductive additives can be added in the solid phase, which result in higher electronic conductivity. However, cathodes with less porosity have intrinsically slower ion transport, which limits the reaction and lowers specific energy.

It is sufficient to use highly conductive surface coatings only, versus using both larger graphite particle and coating, to obtain high specific energy. In the studied variable ranges, cathode systems with 36.2% active material, 0% graphite, 10% PVDF/C and 192.5 μm thickness results in the highest specific energy of 323.5 Wh/kg. As our previous study shows [22], PVDF/C coating phase achieve percolation base on percolated active material spherical particulate system, which has advantage to boost effective conductivity easily. It is not necessary to use graphite to further increase conductivity, which does not contribute to higher specific energy.

Clearly, optimal design is needed for cathode thickness and volume fraction of active material. Ion transport, cathode capacity, and mass balance effect of active material are important factors on utilization. For thicker cathode electrode (250 to 400 μm), long ion transporting distance limits reaction rate, resulting in lower utilization. In

order to improve utilization in thicker electrode, selection of low volume fraction active material to obtain more porosity is a better strategy. On the other hand, cathode capacity and mass balance effect of active material explain lower utilization in thinner electrode (50 to 100 μm). Fig. 3.11 shows the upper bound and lower bound of weight ratio of active material to whole battery, where the weight ratio decreases with decrease in cathode electrode length. Therefore, even though ion has shorter transporting distance in thinner cathode, relatively lower capacity due to mass balance effect of active material also results in lower utilization. In thinner electrodes, more active material is required, rather than porosity, to improve specific energy since liquid limitation is not the dominant issue.

APPENDIX

The diffusion coefficient of Li in $Li_x(Ni_{1/3}Co_{1/3}Mn_{1/3})O_2$ was averaged value from the diffusion coefficient of $Li_x(Co_{0.5}(NiMn)_{0.25})O_2$ and $Li_x(Li_{0.08}Co_{0.16}(NiMn)_{0.38})O_2$ and the curve is shown in Fig. 3.12 [38].

Open-circuit potential vs. state of charge of $Li(Ni_{1/3}Co_{1/3}Mn_{1/3})O_2$ was estimated from discharge-capability plot at 0.09C. The curve is shown in Fig. 3.13 [37].

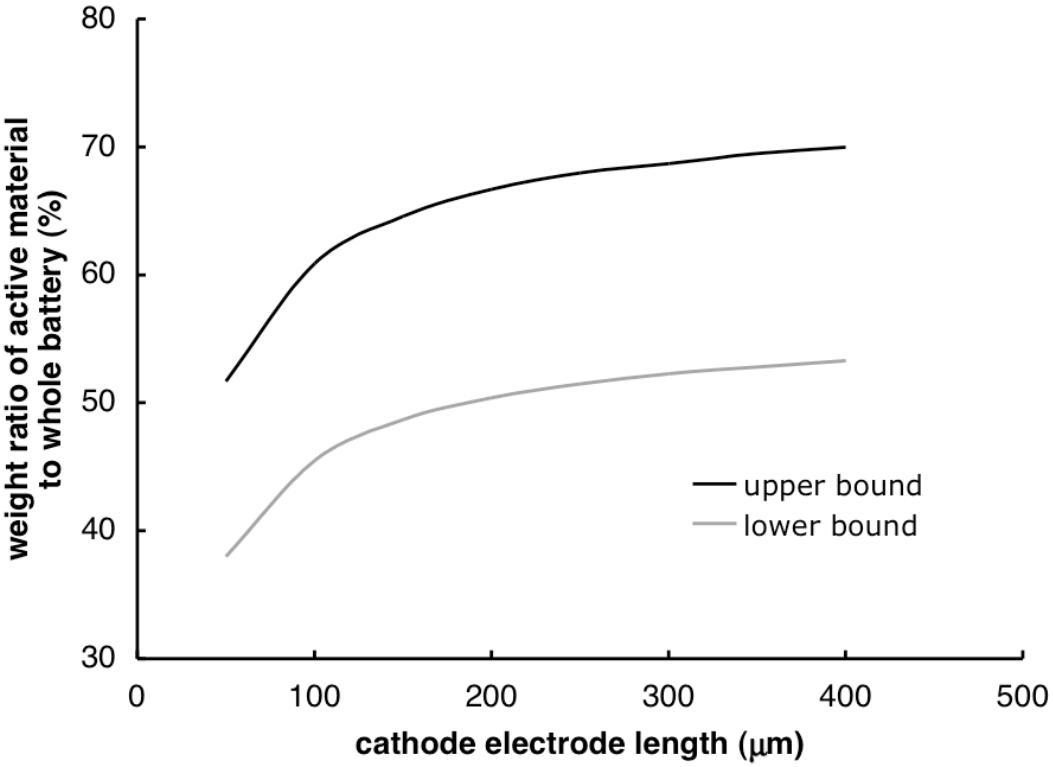

Figure 3.11: Upper bound and lower bound of weight ratio of active material to whole battery in studied cases.

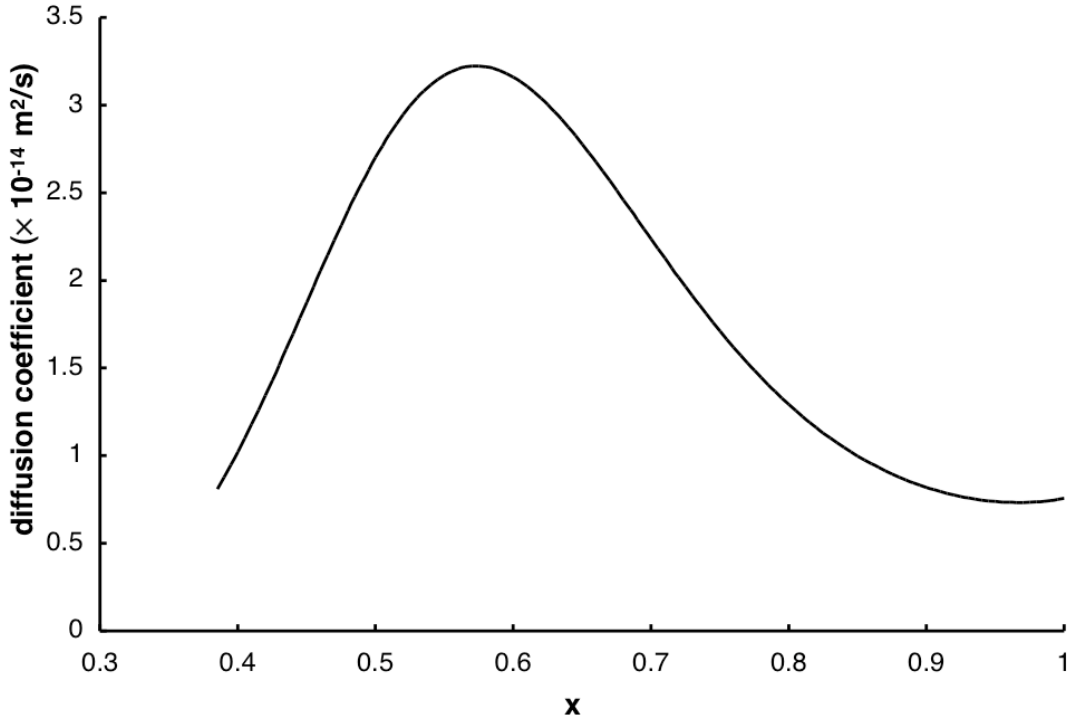

Figure 3.12: The diffusion coefficient of Li in $Li_x(Ni_{1/3}Co_{1/3}Mn_{1/3})O_2$.

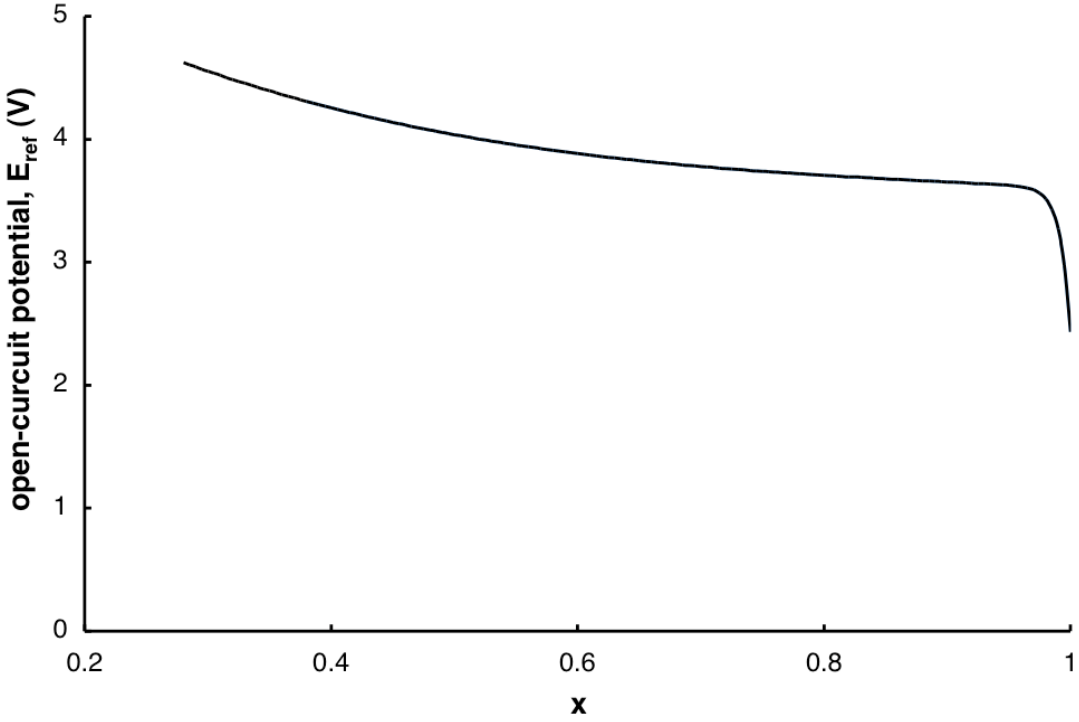

Figure 3.13: The open-circuit potential of $Li(Ni_{1/3}Co_{1/3}Mn_{1/3})O_2$ as a function of state of charge.

BIBLIOGRAPHY

1. Z. Chen, and J. R. Dahn, Studies of $LiCoO_2$ coated with metal oxides, Electrochemical and Solid-State Letters, 6 (11), A221-A224 (2003).

2. G. T. -K. Fey, R. F. Shiu, T. P. Kumar, C. L. Chen, Preparation and characterization of lithium nickel cobalt oxide powders via a wet chemistry processing, Materials Science & Engineering B, 100, (3), 234-243 (2003).

3. S. Mandal, J. M. Amarilla, J. Ibanez, and J. M. Rojo, The role of carbon black in $LiMn_2O_4$-based composites as cathodes for rechargeable lithium batteries, Journal of Electrochemical Society, 148, A24-A29 (2001).

4. J. Newman and K. E. Thomas-Alyea, Electrochemical Systems, p. 518-519, John Wiley & Sons, New Jersey (2004).

5. K. E. Thomas, S. E. Slop, J. B. Kerr, and J. Newman, Comparison of lithium-polymer cell performance with unity and nonunity transference numbers, Journal of Power Sources, 89 (2), 132-138 (2000).

6. C. Wang, L. Taherabadi, G. Jia, S. Kassegne, J. Zoval, and M. Madou, Carbon-MEMS architectures for 3D microbatteries, Proceedings of the SPIE - The International Society for Optical Engineering, 5455 (1), 295-302 (2004).

7. R. S. Rubino, H. Gan, and E. S. Takeuchi, A study of capacity fade in cylindrical and prismatic lithium-ion batteries, Journal of the Electrochemical Society, 148 (9), A1029-A1033 (2001).

8. S. P. Sheu, C. Y. Yao, J. M. Chen, and Y. C. Chiou, Influence of the $LiCoO_2$ particle size on the performance of lithium-ion batteries, Journal of Power Sources, 68 (2), 533-535 (1997).

9. R. Vacassy, H. Hofmann, N. Papageorgiou, and M. Gratzel, Influence of the particle size of electrode materials on intercalation rate and capacity of new electrodes, Journal of Power Sources, 81, 621-626 (1999).

10. C. -H. Lu and S. -W. Lin, Influence of the particle size on the electrochemical properties of lithium manganese oxide, Journal of Power Sources, 97-98, 458-460 (2001).

11. T. Kawamura, M. Makidera, S. Okada, K. Koga, N. Miura, and J. -i. Yamaki, Effect of nano-size $LiCoO_2$ cathode powders on Li-ion cells, Journal of Power Sources, 146 (1-2), 27-32 (2005).

12. U. Lafont, C. Locati, and E. M. Kelder, Nanopowders of spinel-type electrode materials for Li-ion batteries, Solid State Ionics, Diffusion & Reactions, 177 (35-36), 3023-3029 (2006).

13. V. Srinivasan and J. Newman, Design and optimization of a natural graphite/iron phosphate lithium-ion cell, Journal of the Electrochemical Society, 151 (10), A1530-A1538 (2004).

14. S. Ahn, Y. Kim, K. J. Kim, T. H. Kim, H. Lee, and M. H. Kim, Development of High Capacity, High Rate Li+ ion Batteries Utilizing Metal Fiber Conductive Additives, Journal of Power Sources, 82, 896-901 (1999).

15. J. S. Sakamoto, and B. Dunn, Vanadium Oxide-Carbon Nanotube Composite Electrodes for Use in Secondary Lithium Batteries, Journal of the Electrochemical Society, 149 (1), A26-A30 (2002).

16. J. S. Sakamoto, and B. Dunn, Vanadium Oxide-Carbon Nanotube Composite Electrodes for Use in Secondary Lithium Batteries. Journal of the Electrochemical Society, 149, 1, A26-A30 (2002).

17. K. Zaghib, J. Shim, A. Guerfi, P. Charest, and K. A. Striebel, Effect of Carbon Source as Additives in Lifepo4 as Positive Electrode for Lithium-Ion Batteries, Electrochemical and Solid State Letters, 8 (4), A207-A210 (2005).

18. C. M. Julien, K. Zaghib, A. Mauger, M. Massot, A. Massot, A. Ait-Salah, M. Selmane, F. Gendron, Characterization of the Carbon Coating onto $LiFePO_4$ Particles used in Lithium Batteries, Journal of Applied Physics, 100 (6), 63511-1-7 (2006).

19. Y. -H. Chen, C. -W. Wang, G. Liu, X. -Y. Song, V. S. Battaglia, and A. M. Sastry, Selection of conductive additives in Li-ion battery cathodes: a numerical study, Journal of the Electrochemical Society, 154 (10), A978-A986 (2007).

20. C. -W. Wang and A. M. Sastry, Mesoscale modeling of a Li-ion polymer cell, Journal of the Electrochemical Society, 154 (11), A1035-A1047 (2007).

21. J. Newman and W. Tiedemann, Porous-electrode theory with battery applications, AIChE Journal, 21(1), 25-41 (1975).

22. M. Doyle, J. Newman, A. S. Gozdz, C. N. Schmutz, and J. -M. Tarascon, Comparison of modeling predictions with experimental data from plastic lithium ion cells, Journal of the Electrochemical Society, 143 (6), 1890-1903 (1996).

23. E. Deiss, D. Haringer, P. Novak, and O. Haas, Modeling of the charge-discharge dynamics of lithium manganese oxide electrodes for lithium-ion batteries. Electrochimica Acta, 46 (26-27), 4185-4196 (2001).

24. E. Barsoukov, D. H. Kim, H. S. Lee, H. Lee, M. Yakovleva, Y. Gao, and J. F. Enge, Comparison of kinetic properties of $LiCoO_2$ and $LiTi_{0.05}Mg_{0.05}Ni_{0.7}Co_{0.2}O_2$ by impedance spectroscopy, Solid State Ionics, 161 (1-2), 19-29 (2003).

25. B. Y. Liaw, R. G. Jungst, G. Nagasubramanian, H. L. Case, and D. H. Doughty, Modeling capacity fade in lithium-ion cells, Journal of Power Sources, 140 (1), 157-161 (2005).

26. B. Y. Liaw, G. Nagasubramanian, R. G. Jungst, and D. H. Doughty, Modeling of lithium ion cells—A simple equivalent-circuit model approach, Solid State Ionics, 175 (1-4), 835-839 (2004).

27. J. N. Reimers, Can first principles calculations aid in lithium-ion battery design, Journal of Power Sources, 54 (1), 16-19 (1995).

28. J. W. Halley and Y. Duan, Role of atomic level simulation in development of batteries, Journal of Power Sources, 110 (2), 383-388 (2002).

29. M. E. Garcia, E. Webb, and S. H. Garofalini, Molecular dynamics simulation of V_2O_5/Li_2SiO_3 Interface, Journal of the Electrochemical Society, 145 (6), 2155-2164 (1998).

30. S. H. Garofalini and P. Shadwell, Molecular dynamics simulation of cathode/glass interface behavior: effect of orientation on phase transformation, Li migration, and interface relaxation, Journal of Power Sources, 89 (2), 190-200 (2000).

31. http://www.matweb.com (date: 04/20/2007).

32. S. -I. Lee, U. -H. Jung, Y. -S. Kim, M. -H. Kim, D. -J. Ahn, and H. -S. Chun, A study of electrochemical kinetics of lithium ion in organic electrolytes, Korean journal of Chemical Engineering, 19, 638-644 (2002).

33. Y. F. Zhou, S. Xie, X. W. GE, C. H. Chen, and K. Amine, Preparation of rechargeable lithium batteries with poly(methyl methacrylate) based gel polymer electrolyte by in situ γ-ray irradiation-induced polymerization, Journal of Applied Electrochemistry, 34 (11), 1119-1125 (2004).

34. C. -W. Wang, A. M. Sastry, K. A. Striebel, and K. Zaghib, Extraction of layerwise conductivities in carbon-enhanced, multilayered $LiFePO_4$ cathodes, Journal of The Electrochemical Society, 152 (5), A1001-A1010 (2005).

35. ABAQUS/STANDARD, Hibbitt, Karlsson & Sorensen Inc.

36. http://www.uscar.org/commands/files_download.php?files_id=156

37. N. Yabuuchi and T. Ohzuku, Novel lithium insertion material of $LiCo_{1/3}Ni_{1/3}Mn_{1/3}O_2$ for advanced lithium-ion batteries, Journal of Power Sources, 119-121, 171-174 (2003).

38. Kevin Eberman and Larry Krause, Diffusion coefficient of lithium in $Lix(Co_y(NiMn)_{(1-y)/2})O2$ cathode powders, The 204th Electrochemical Society Meeting, Orlando, FL (2003).

CHAPTER IV

IMAGE ANALYSIS AND COMUPTER SIMULATION OF AGGLOMERATION AND AGGREGATION PHENOMENA OF NANOPARTICLE CLUSTER[1]

INTRODUCTION

Megatons of particulates are produced annually by combustion methods including desirable nanomaterials [1,2] and toxic byproducts [3]. Yet accurate prediction of particulate emissions from combustion systems remains a daunting challenge. The chemical and physical processes involved span scales from the atomistic level of elementary chemical reactions to interparticle collision of highly three-dimensional micron-sized fractal structures. Advances in experimental and computational methods have demonstrated how the complex nature of combustion-generated materials (including the composition, polydispersity, and morphology of the nanoparticles) impacts the fate and transport of the nanoparticles [2, 4, 5, 6, 7, 8]. Accurate understanding of the physical and chemical characteristics of soot are particularly important in light of the adverse affects of carbonaceous soot on human health and the environment. The optical, electronic and catalytic properties of nanoparticles, critical for the design of advanced flame-generated materials, are also strong functions of the nanoparticle composition and

[1] Material in this chapter is a unpublished paper in progress: Y. -H. Chen, S. D. Bakrania, M. S. Wooldridge, and A. M. Sastry, Image analysis and computer simulation of agglomeration and aggregation phenomena of nanoparticle clusters, *Journal of Materials Science*, (2008).

architecture [9, 10, 11, 12, 13]. Improved methods to analyze and predict the complex physical properties of particulate emissions from combustion systems are vital to reduce pollutant particulate emissions and accelerate design of advanced materials.

Soot particles emitted from combustion processes are generally fractal structures that consist of primary particles on the order of 10-20 nm in diameter, where the primary particles are approximately spherical in shape (see Fig. 4.1). The fractal structures are created by agglomeration and aggregation, where an aggregate is a cluster of primary particles that are joined by inter-particle necks (which form due to locally high temperatures), and an agglomerate is a cluster of primary particles sticking to each other due to different and random attractive forces that occur between particles [14, 15]. Surface reactions, including oxidation, can also affect the composition and structure of soot emissions. The fractal geometries of soot particles are determined by competition between the nucleation rate of the primary particles, the interparticle collision rate, and the coalescence or sintering rate [16]. The morphology or geometry of the soot particulates is therefore determined by how primary particles form, collide and bond together. A quantitative understanding of the final morphology of soot emissions is critical to understanding fate, transport, reactivity and functionality of clusters of nanoparticles [2,5,6,10,11] and in particular, recent work has demonstrated the importance of understanding the fractal nature of soot particles [7,8, 17].

There have been many studies to understand the forces important during collision between nanoparticles. Table I highlights several methods, including experimental, molecular dynamics and mathematical modeling, used to study agglomerates and aggregates of nanoparticles and used to verify the different forces leading to different

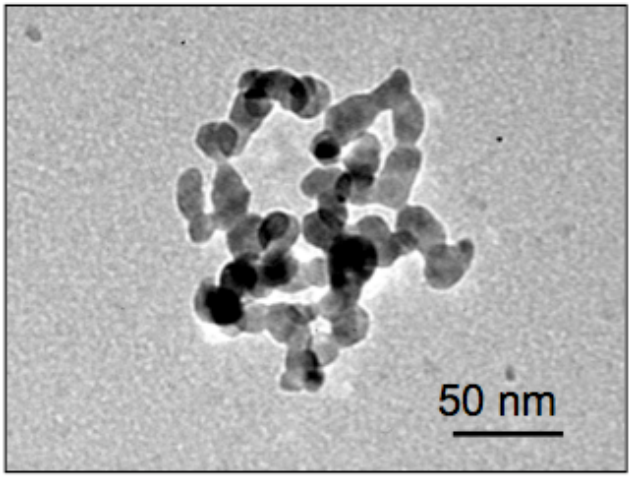

Figure 4.1: Transmission electron micrograph image of flame-generated tin dioxide nanoparticle cluster.

nanoparticle system	process used to create nanoparticles	force identified (experimental)/ force applied (simulation)	validation method	reference
Si	silane pyrolysis	Coulomb	experiment	Onischuk et al.[18]
carbonaceous soot	propane combustion	Coulomb	experiment	Onischuk et al.[18]
TiO_2	flame synthesis of $TiCl_4$	van der Waals	experiment	Froeschke et al.[19]
Ag, Ni	spark discharge	van der Waals	experiment	Froeschke et al.[19]
Si	simulation	van der Waals	molecular dynamics	Hawa and Zacharaiah[22]
colloidal nanoparticles	simulation	van der Waals solvation	molecular dynamics	Qin and Fichthorn[23]
colloidal nanoparticle	simulation	Coulomb	mathematical (finite element) modeling	Das and Bhattacharjee[24]
CdTe	simulation	Coulomb van der Waals	mathematical (Monte Carlo) modeling	Sinyagin et al.[26]
SiO_2	simulation	van der Waals	mathematical (moment) modeling	Suh et al.[25]

Table 4.1:Methods used to validate and/or represent interactions between nanoparticle collisions.

structures. Agglomeration has been extensively studied using experimentation. For example, in the study by Onischuk et al. [18] time-resolved imaging captured the process of adhesion between agglomerates, and the authors demonstrated that Coulomb forces were significant during the sticking process. In the work by Froeschke et al. [19], impact fragmentation of nanoparticle agglomerates was used to calculate the bond strength between primary particles and to verify the existence of van der Waals interactions.

In addition to experiments, computer simulations, such as molecular dynamics, are a useful and common way to simulate collisions and coalescence between particles. Molecular dynamics has often been applied to simulate the formation of primary particles (see for example Lümmen and Kraska [20] and Zachariah and Carrier [21]), and to study attractive forces and collisions between particles (see for example Hawa and Zachariah [22] and Qin and Fichthorn [23]). Mathematical modeling of agglomeration has also been carried out using finite element [24], moment [25], Monte Carlo [26] and stochastic methods [27]. These studies and others confirm that van der Waals interactions, static electricity, and solid-state necking (particularly at high temperatures) are the most important processes to represent coagulation between nanoparticles.

The experimentally observed morphology of nanostructured soot agglomerates has been most extensively studied using image analysis. Transmission electron microscopy (TEM) is the most common technique used for this purpose. TEM is typically used to acquire two-dimensional (2D) images of the agglomerates, which can be analyzed to extract information such as the average size of the primary particles, the number of primary particles in the agglomerate or aggregate, etc. Such 2D projections

provides little information on the three-dimensional (3D) structure of the agglomerates; however, recent advances in TEM methods, such as electron tomography [17, 28, 29, 30, 31] and relative optical density [32, 33]. have extended the capabilities of TEM imaging to evaluate the 3D morphology of nanostructures.

Image processing is essential to extract quantitative information from 2D and 3D TEM imaging data. Computer aided image analysis can easily handle a large number of particles and clusters, and it is much faster and less subjective than analysis conducted by individuals. Image analysis is commonly used to obtain the size distribution of nanoparticles [34, 35] and fractal dimensions [36, 37] in 2D and 3D images. Other parameters, such as radius of gyration, linearity coefficient, aspect ratio, and particle chain length are also used to characterize the geometry of fractal nanoparticle structures [26, 38].

Although the morphology of soot agglomerates has been studied extensively using 2D TEM imaging and 2D simulations, there are few experimental or modeling data describing the 3D nanoarchitecture of soot particles which is so important to understanding the behavior of combustion generated particulates. In order to address this need, the current work presents a novel approach which combines 3D modeling and experiments in order to determine the interactions between nanoparticles and to predict the morphology of particles generated from combustion systems. The method includes 3D TEM, image analysis, and computer simulation. Semi-stochastic or probabilistic modeling is used as the basis for simulating the nanoparticle interactions. Semi-stochastic mathematics is a powerful and robust means to model nanoparticle agglomeration because such methods do not require extensive information on material

properties, environmental conditions, and reaction processes, which are often unavailable, particularly for nanoscale systems and combustion environments. Computer simulations based on probabilities can model agglomeration in 3D to predict 3D soot morphology. Such a technique can be combined with 3D imaging and analysis from experimental data to predict or analyze mechanisms of nanoparticle cluster formation. Based on the motivation to develop such analytical and predictive capabilities, the two objectives of this work are to develop the methods to simulate formation of nanoparticle clusters by semi-stochastic placement, and to apply this method to identify the forces important during nanoparticle clustering in a representative combustion system.

METHODS

EXPERIMENTAL METHODS

Figure 4.2 shows the schematic of the combustion synthesis facility used to generate the combustion nanoparticulates analyzed in this work. Tin dioxide (SnO_2, cassiterite phase) particles were generated using a multi-element hydrogen-oxygen diffusion burner. Tetramethyltin (TMT, $Sn(CH_3)_4$) was introduced into the flame as a precursor for tin dioxide using argon as a carrier gas, yielding argon flow saturated with approximately 21% TMT on mole basis. TEM samples were acquired by thermophoretic deposition onto carbon-meshed copper grids at a height of 27 centimeters above the burner surface. Additional details on the particle sampling, burner characteristics and operating conditions can be found in Miller et al. [39] and Bakrania et al. [40, 41].

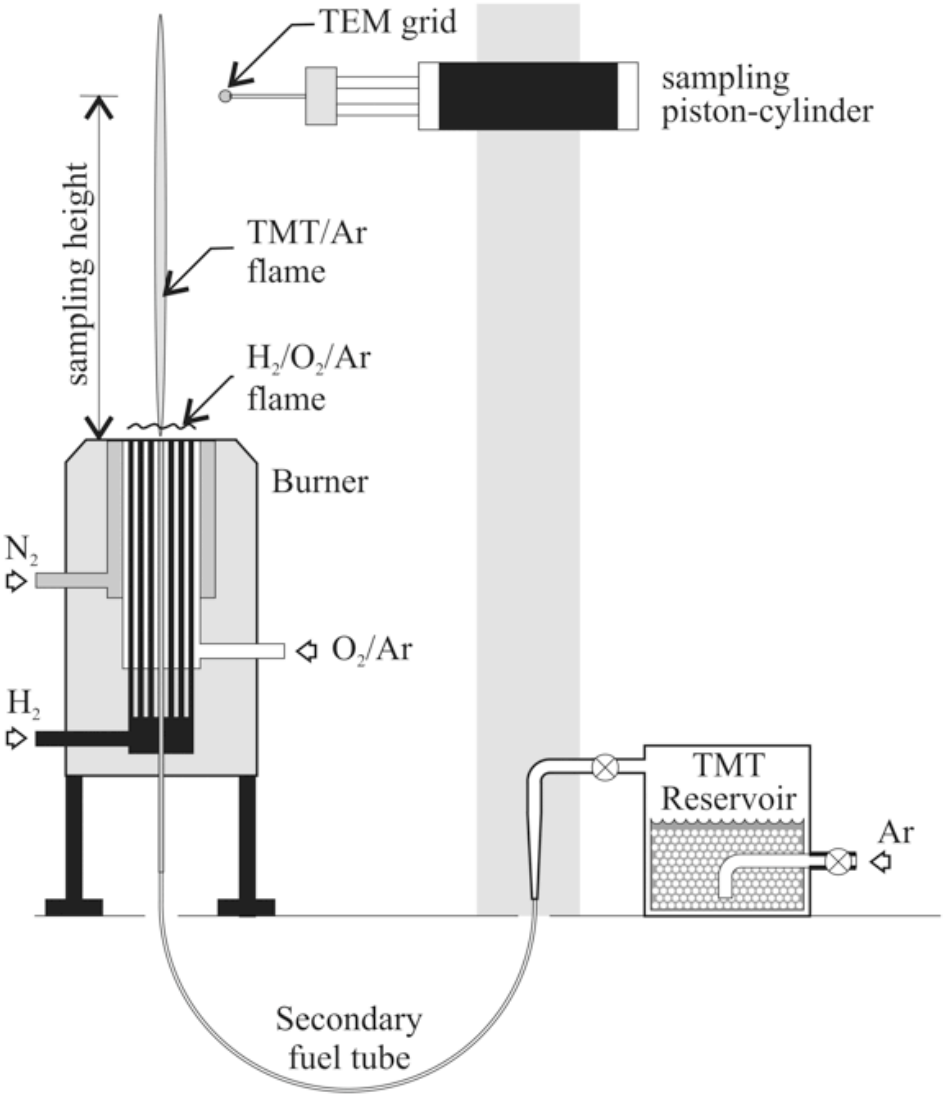

Figure 4.2: Schematic of the combustion synthesis facility used to create the tin dioxide nanoparticles.

TEM images were obtained using a JEOL 3011 High Resolution Electron Microscope. The specimen tilt capability was used to acquire 2D images at various planes of inclination with the tilt angle ranging from -55° to +55° in 2.5° increments. The 2D images acquired were aligned using the image processing and modeling software IMOD [42, 43]. Image data were converted between Fourier and real spaces based on the electron tomographic technique [28] and tomographic images were obtained from data conversion. The 3D cluster was then reconstructed and rendered by detecting the outline of the tomographic images using IMOD.

COMPUTATIONAL METHODS

A semi-stochastic method was used for the algorithm for generating the nanoparticle clusters. The model is semi-stochastic because the presence of particles depends on assigned probabilities in order to simulate the effect of different interactions. The computer simulation was used to generate 3D clusters of nanoparticles. The simulation was a 3D model with non-periodic boundaries. Each length of the domain cell was set at 1000 times the particle diameter so the cluster created in the simulation could not contact the boundary. During each simulation, a cluster consisting of N particles was formed, and 100 realizations of agglomerates for each value of N were computed and the results were averaged. Values of N from 10 to 100 were simulated. For each calculation, the initial primary particle was placed in the center of the cell. The agglomeration of nanoparticles was represented as a series of steps of single particle addition, assuming a constant size for all particles. The position of each new particle depended on the assigned probabilities. Two particle bonding criteria for forming agglomerates were

considered. Case (1) is the addition of the next particle sticking to other particles in the cluster. Case (2) is the addition of the next particle sticking to the tip of a chain of particles in the cluster.

Case (1) represents the short-range van der Waals forces that make particles stick together when two particles collide. Figure 4.3 shows schematically how Case (1) is implemented in the simulations. For each particle addition step, a particle within the existing cluster is randomly chosen as the binding site. The position of the new particle is chosen using a random angle around the particle in the cluster. If the new particle overlaps with other particles in the cluster, the new particle is not added to the cluster and the process is restarted.

Case (2) represents the attractive forces due to dipoles or charges concentrated on the tip of a chain of particles and the repulsive forces of the inner part of a cluster. These long-range forces cause bonding to occur at the tip of a chain of particles. Figure 4.4 shows schematically how Case (2) is implemented in the simulations. For a cluster with two tip particles in the computational domain, one tip particle is randomly selected as the site for the addition of the new particle. The position of the new particle is determined using a random angle around the hemisphere of the tip particle. The assumption of the new particle sticking at an angle in the hemisphere of the tip particle is based on experimental observation [18]. As with Case (1), if the new particle overlaps with other particles in the cluster, the new particle is not added to the cluster, and the process is restarted.

P1 is the probability of Case (1) occurring during agglomerate formation, and P2 is the probability of Case (2). The summation of P1 and P2 is 1 because there are only

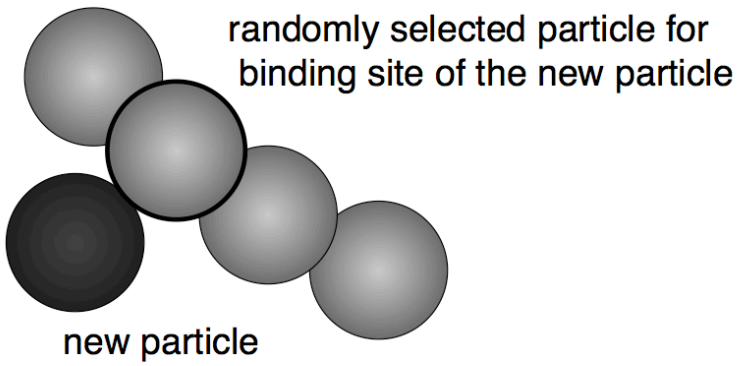

Figure 4.3: Schematic representing the Case 1 binding method. The gray particles are particles existing within the computational boundary, and the black particle is the new particle searching for a binding site. The gray particle circled in black is the randomly chosen particle for binding.

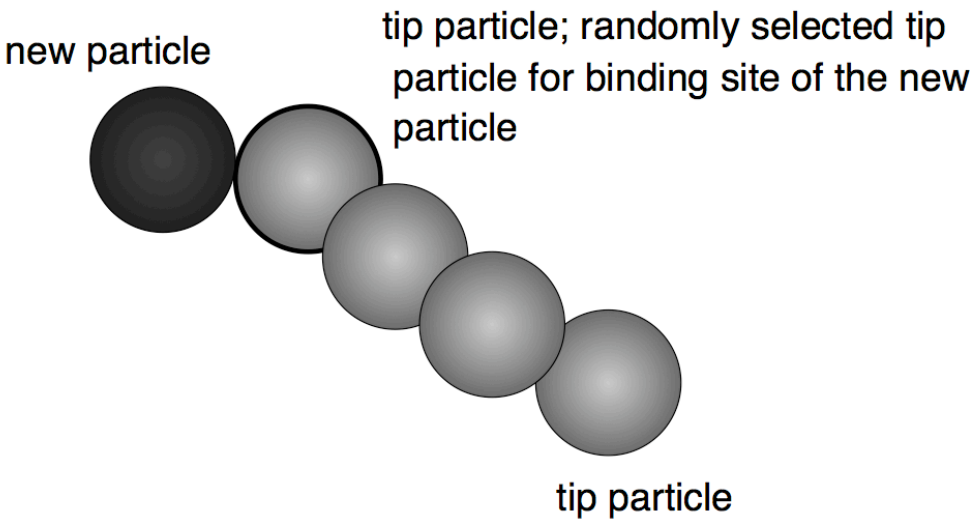

Figure 4.4: Schematic representing the Case 2 binding method. The gray particles are particles existing within the computational boundary, and the black particle is the new particle searching for a binding site. The gray particle circled in black is the randomly chosen tip particle for binding.

two bond criteria assigned in the simulation. By varying the assigned probabilities of Case (1) and Case (2), the combination of forces during the formation of agglomerates can be simulated.

IMAGE ANALYSIS

Radius of gyration, aspect ratio, main chain length, and fractal dimension are used to characterize the geometric properties of the 3D nanoparticle clusters from experiments and simulations. For a specific cluster, radius of gyration, R_g, is used to characterize the overall size of the cluster. Aspect ratio is used to estimate the shape of the cluster in terms of the ratio of the three major axes of the fitted ellipsoid. Main chain length, L_m, is used to determine the maximum chain length in the cluster. Fractal dimension, D_f, is used to characterize the compactness of the cluster. Each geometric property was determined as follows.

Radius of gyration, R_g, of a cluster is a measure of its overall size, which is expressed as

$$R_g = \frac{\int r^2 \rho(\vec{r}) d\vec{r}}{\int \rho(\vec{r}) d\vec{r}} \quad (1)$$

where r is the radial distance measured from the cluster center of mass, ρ(r) is the cluster mass density. The denominator is equal to the total cluster mass. It is assumed that the density of each particle is constant.

From [38], the shape of any object can be characterized by the moment of inertia tensor, T_I, with components

$$T_{ij} = \int \rho(\vec{r}) q_i q_j d\vec{r} \quad \text{for i,j=1,…,d, i≠j}$$

$$T_{ij} = \int \rho(\vec{r}) q_i q_j d\vec{r} \quad \text{for i,j=1,…,d, , i=j} \tag{2}$$

where q_i=x, y, z for i = 1, 2, 3 respectively, and x, y, z are coordinate values. By diagonalizing and dividing by the total cluster mass, the squares of principal radii of gyration R_i^2, for i=1,…,d, can be obtained. Then the shape and overall size are related by

$$R_g^{\,2} = \frac{1}{2}[R_1^{\,2} + R_2^{\,2} + R_3^{\,2}] \tag{3}$$

The relation of principal radii of gyration and axes lengths of a fitted 3D ellipsoid are

$$R_i^{\,2} = \frac{2}{5}[d_j^{\,2} + d_k^{\,2}] \tag{4}$$

where d_i=a, b, c for i=1, 2, 3 respectively, and a, b, c are three main axes of the fitted ellipsoid. By solving for d_i

$$d_i^{\,2} = [\frac{2}{5}((1-2\delta_{i1})R_1^{\,2} + (1-2\delta_{i2})R_2^{\,2} + (1-2\delta_{i3})R_3^{\,2})]^{\frac{1}{2}} \tag{5}$$

where δ_{ij} is the Kronecker delta and d_i corresponds to axes a, b, c for i=1, 2, 3. Aspect radio a_b (a/b) and aspect ratio a_c (a/c) can then be obtained using the eq (5).

Main chain length, L_m, is the length along the actual path between the two most distant particles in a cluster. L_m is calculated using the Floyd-Warshall All-Pairs-Shortest-Path algorithm [44]. Please note the main chain length and radius of gyration are reported as dimensionless values in this work by normalization using the radius of the particle, r. L_m is the length measuring from end point of a particle, through particle center to enter, to end point of another particle For example, if N is one, L_m/r is 2.

The fractal dimension, D_f, is determined using the following expression [45],

$$N = A(\frac{R_i}{r})^{D_f} \tag{6}$$

where r is the radius of primary particle and A is a dimensionless constant. For the simulations, an average value for D_f is determined by averaging over many agglomerates with the same N. For compact agglomerates, D_f is close to 3, and for chain-like structures, D_f is close to 1.

The computationally generated 3D agglomerates and the 3D reconstructions of the experimentally-observed agglomerates were analyzed using identical methods. Uniform 4x4x4 distributed grids were dispersed in each unit cubic to calculate R_g, a_b, a_c, and L_m. Comparison of the simulation results and experimental data allows values for P1 and P2 to be determined, and the forces important during agglomeration can thus be determined indirectly.

RESULTS

Figures 4.5 and 4.6 show TEM images of two distinct SnO_2 agglomerates sampled from the combustion system. The tilt angles used for the images were -55°, 0°, and +55°. As seen in the images, considerably different 2D projections are observed from the same agglomerate for different tilt angles. Figures 4.7 and 4.8 present 2D projections of the reconstructed 3D structures of the agglomerates from Figs. 4.5 and 4.6. The projected 2D images from the 3D reconstruction are presented for -55°, 0°, +55°, +110°, and +165° tilt angles. Note the 2D projected images based on the 3D reconstructions correctly reproduce the TEM images of Figs. 4.5 and 4.6 for equivalent tilt angles.

Figures 4.9 and 4.10 show the effects of the relative values of P1 and P2 on the average aspect ratios a_b and a_c, respectively, for values of N = 20, 40, 60, 80 and 100.

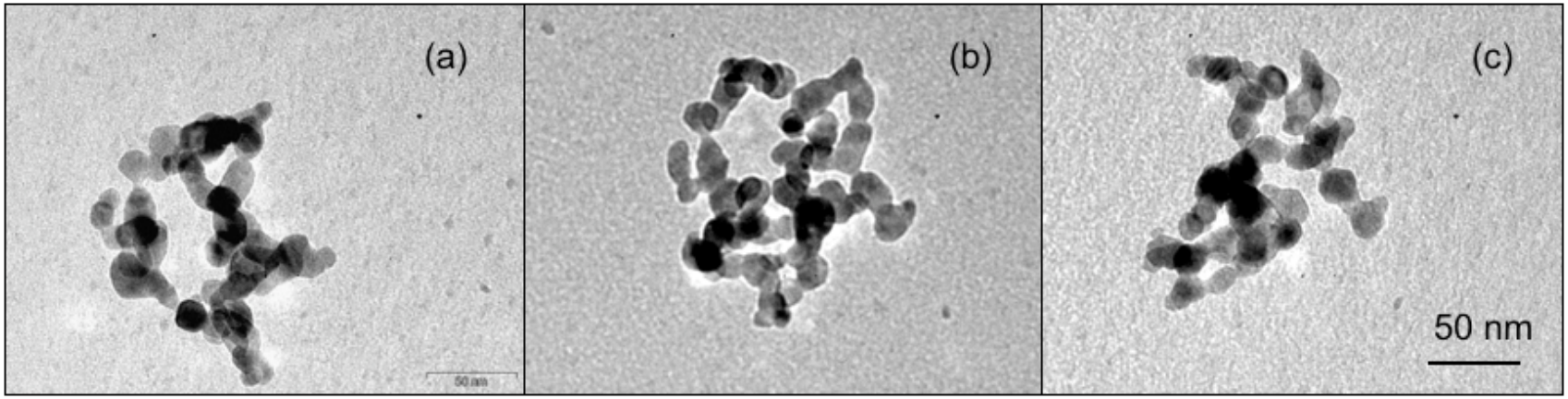

Figure 4.5: TEM pictures of agglomerate I at different tilt angles: (a)-55°, (b)0°, and (c)+55°.

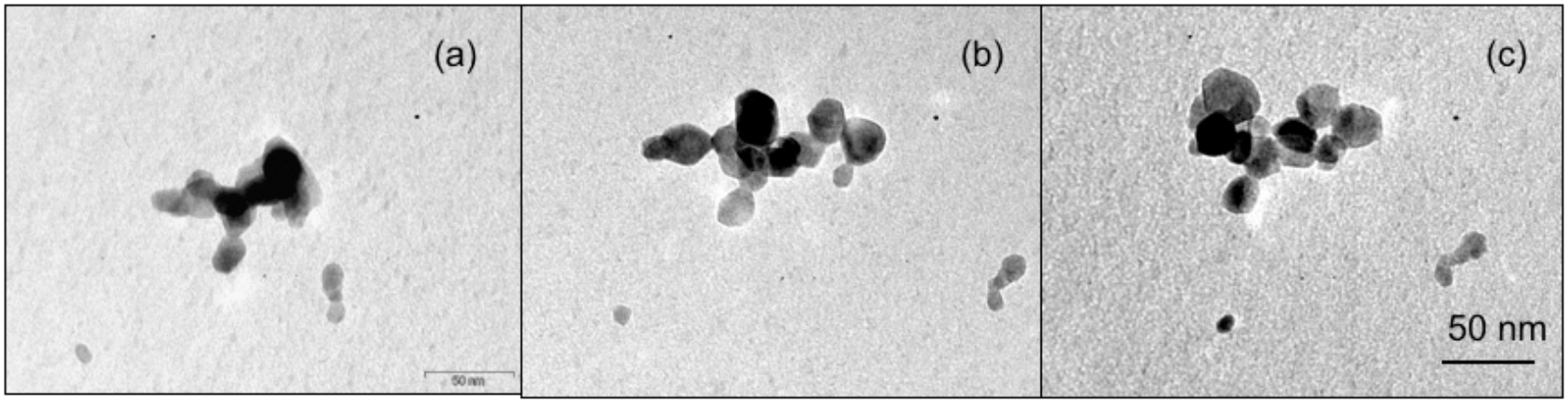

Figure 4.6: TEM pictures of agglomerate II at different tilt angles: (a)-55°, (b)0°, and (c)+55°.

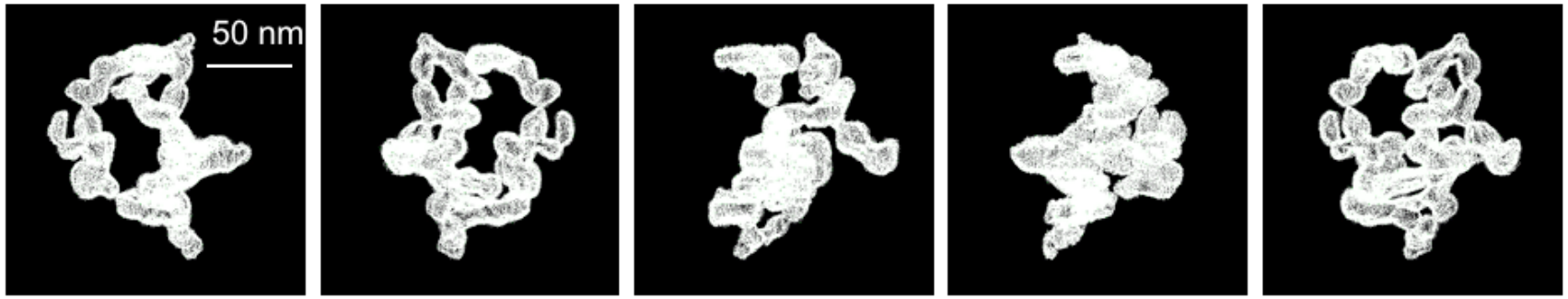

Figure 4.7: 3D model of agglomerate I at different angles: (a)-55°, (b)0°, (c)+55°, (d)+110°, and (e)165°.

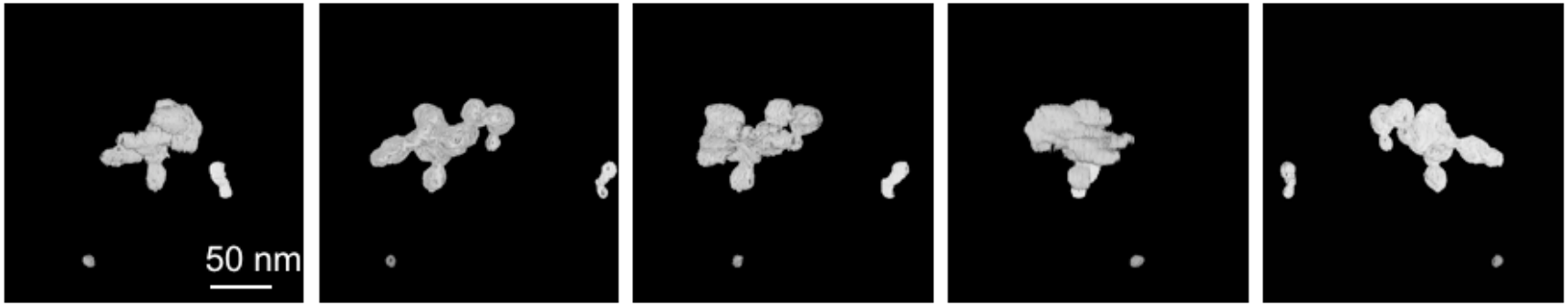

Figure 4.8: 3D model of agglomerate II at different angles: (a)-55°, (b)0°, (c)+55°, (d)+110°, and (e)165°.

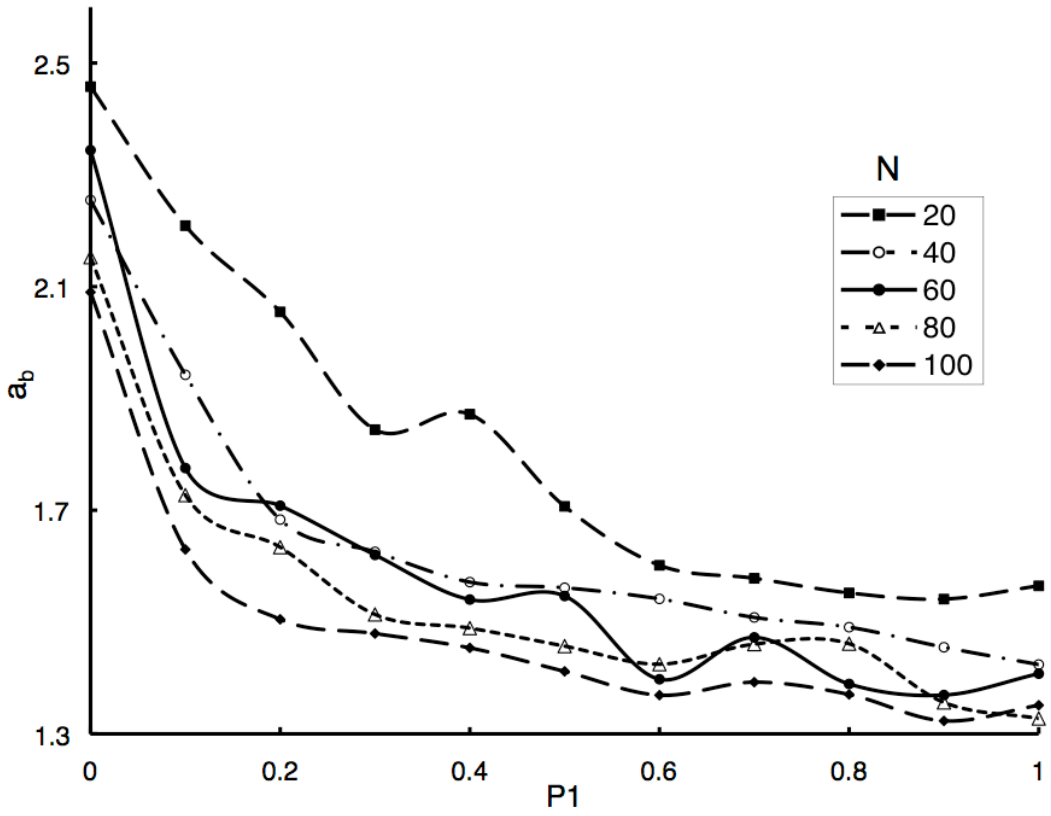

Figure 4.9: Simulation results of a_b as a function of P1 at different cluster size N.

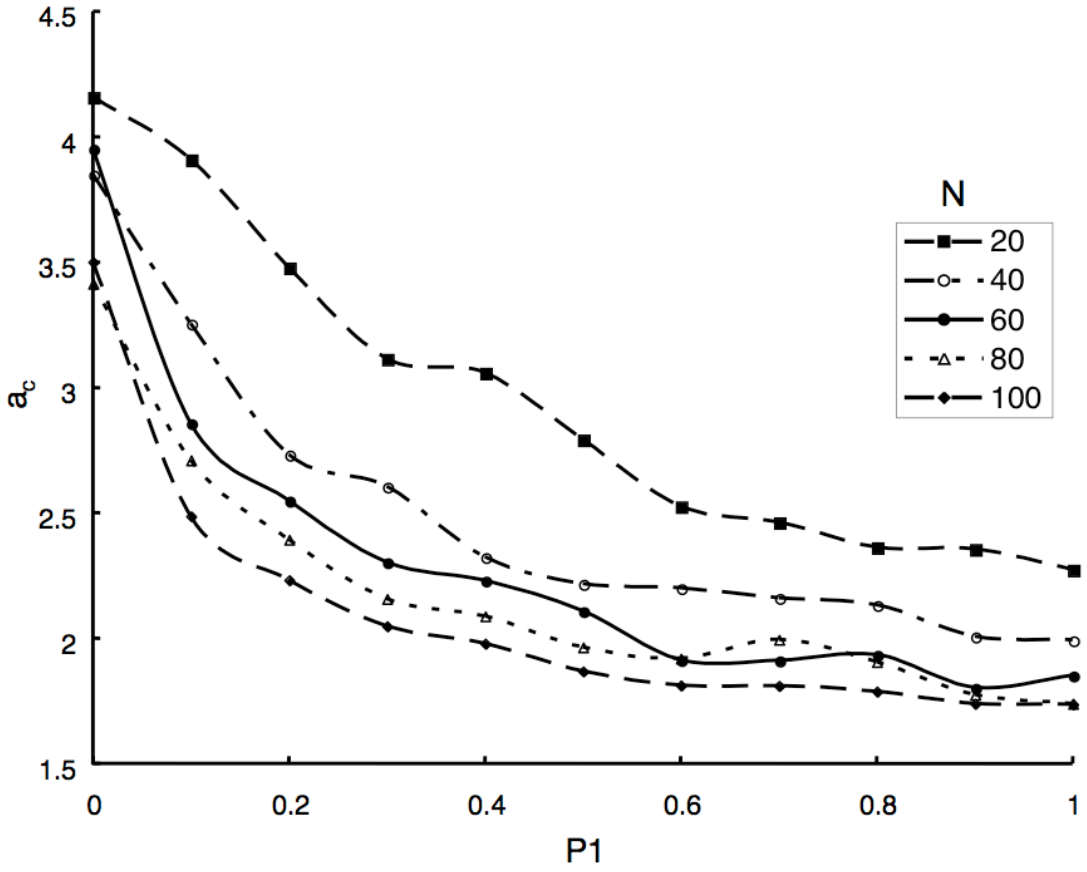

Figure 4.10: Simulation results of a_c as a function of P1 at different cluster size N.

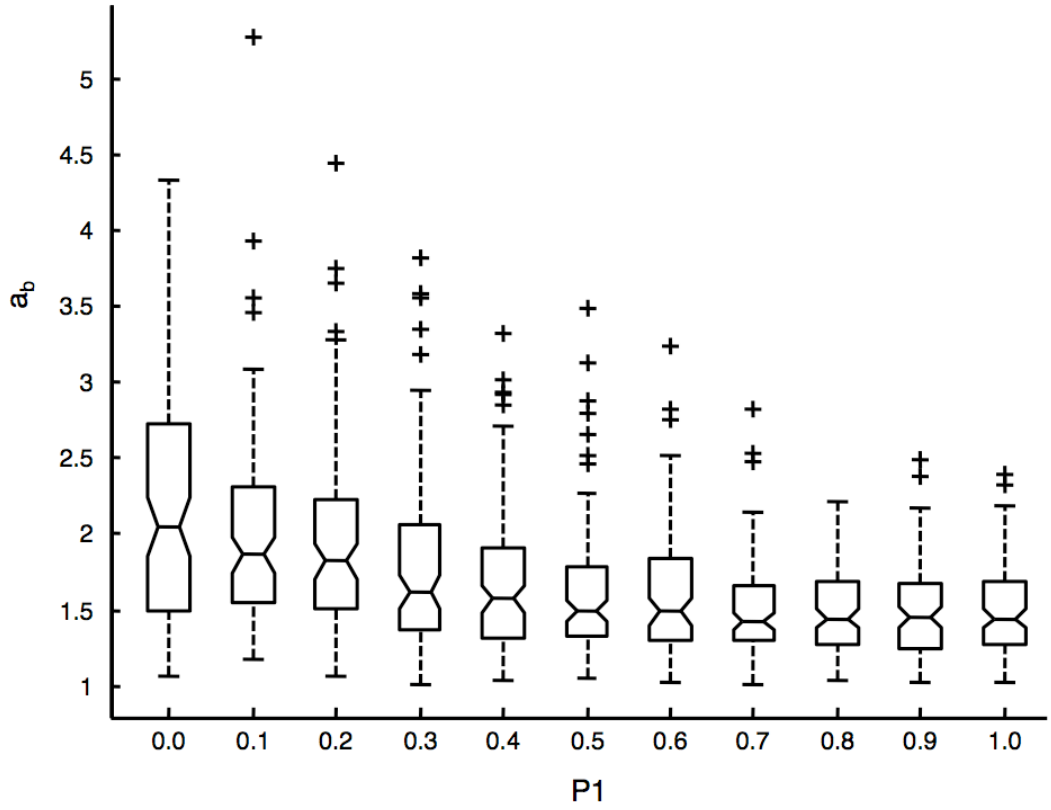

Figure 4.11(a): Simulation results of notched box plots of the effect of P1 on aspect ratio a_b when N is 20.

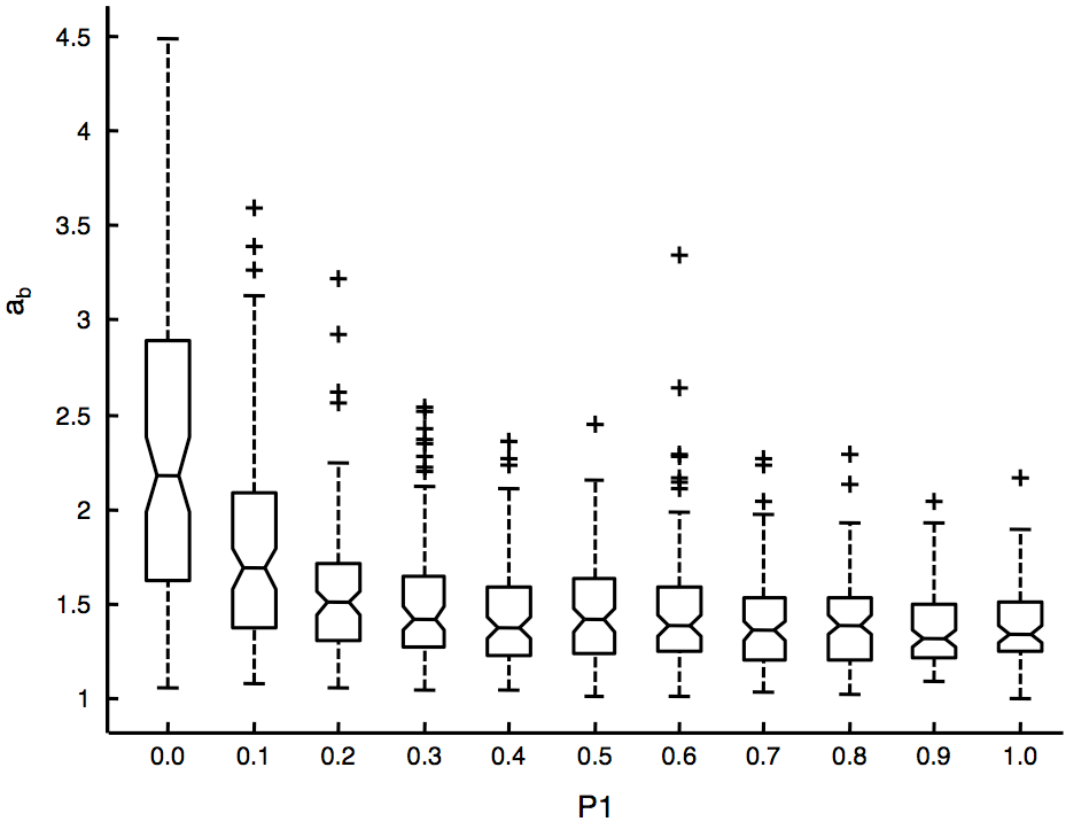

Figure 4.11(b): Simulation results of notched box plots of the effect of P1 on aspect ratio a_b when N is 60.

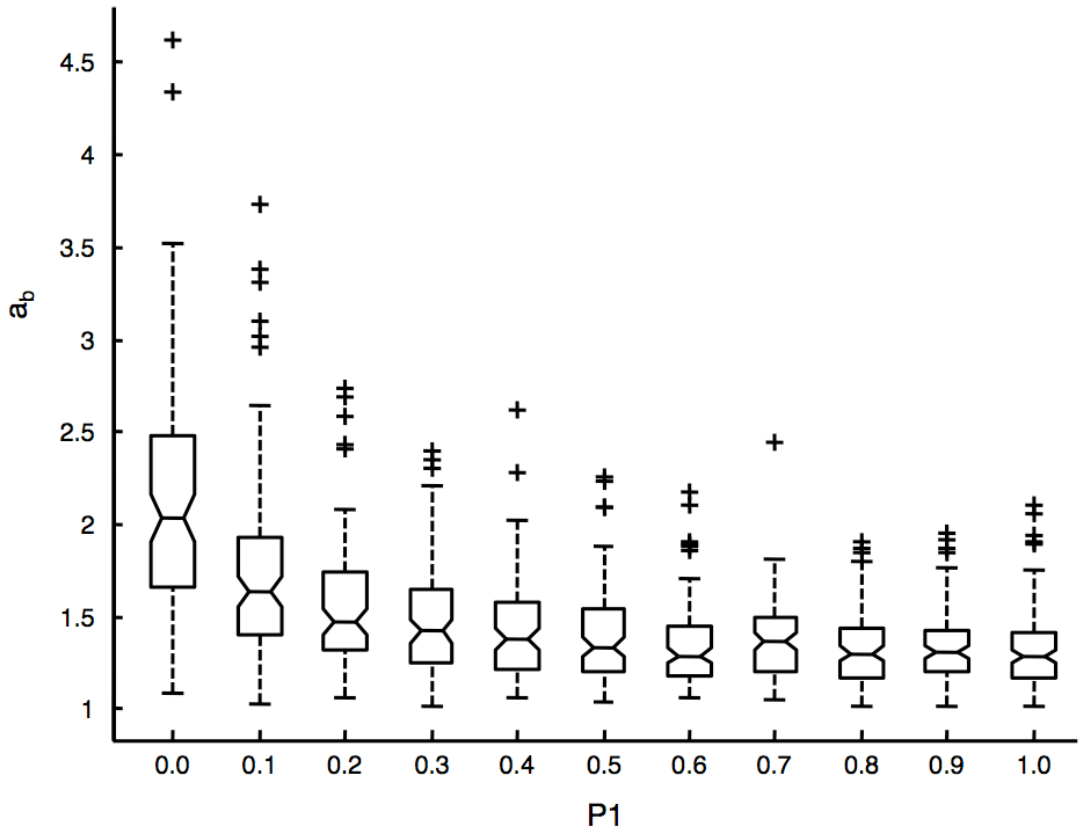

Figure 4.11(c): Simulation results of notched box plots of the effect of P1 on aspect ratio a_b when N is 100.

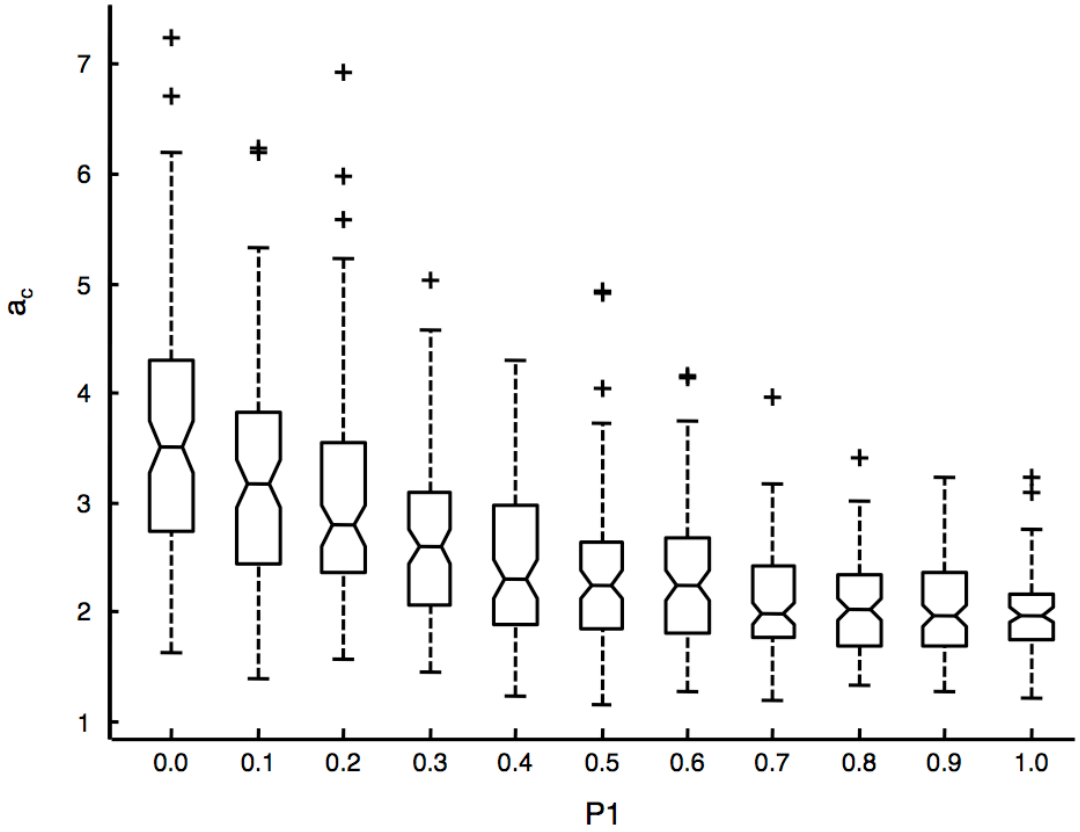

Figure 4.12(a): Simulation results of notched box plots of the effect of P1 on aspect ratio a_c when N is 20.

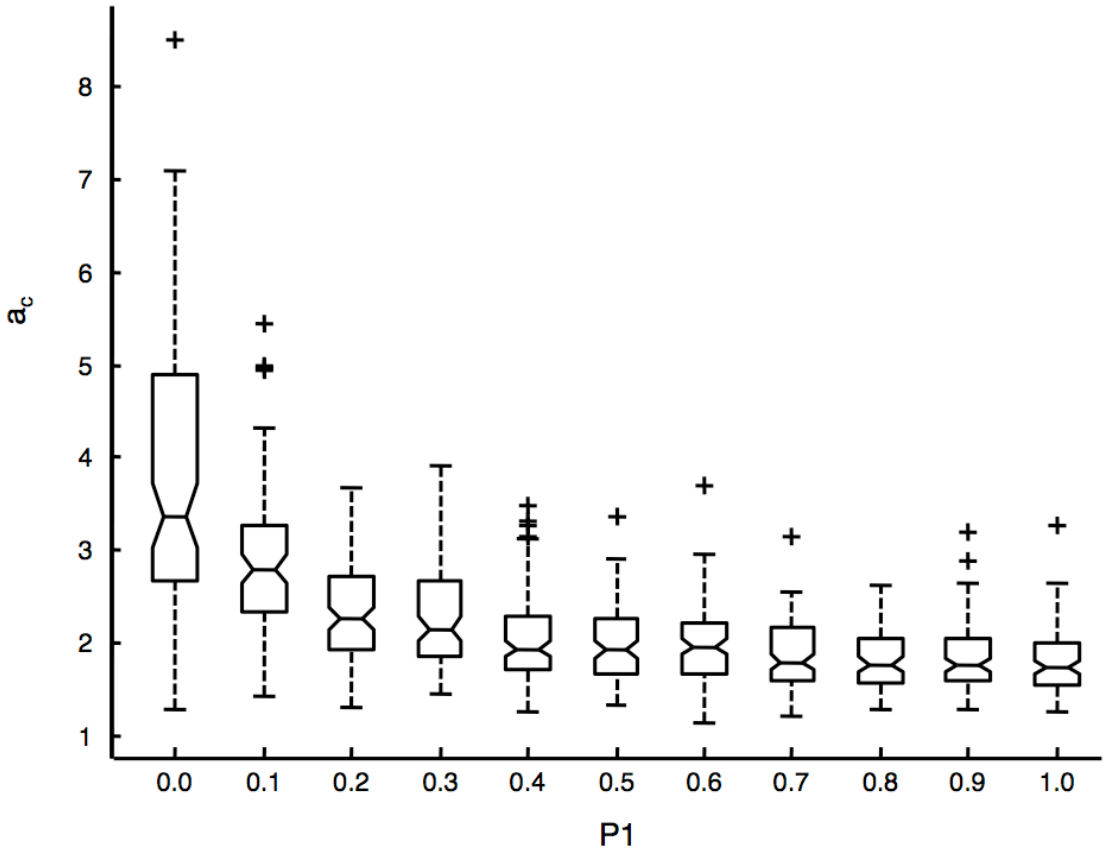

Figure 4.12(b): Simulation results of notched box plots of the effect of P1 on aspect ratio a_c when N is 60.

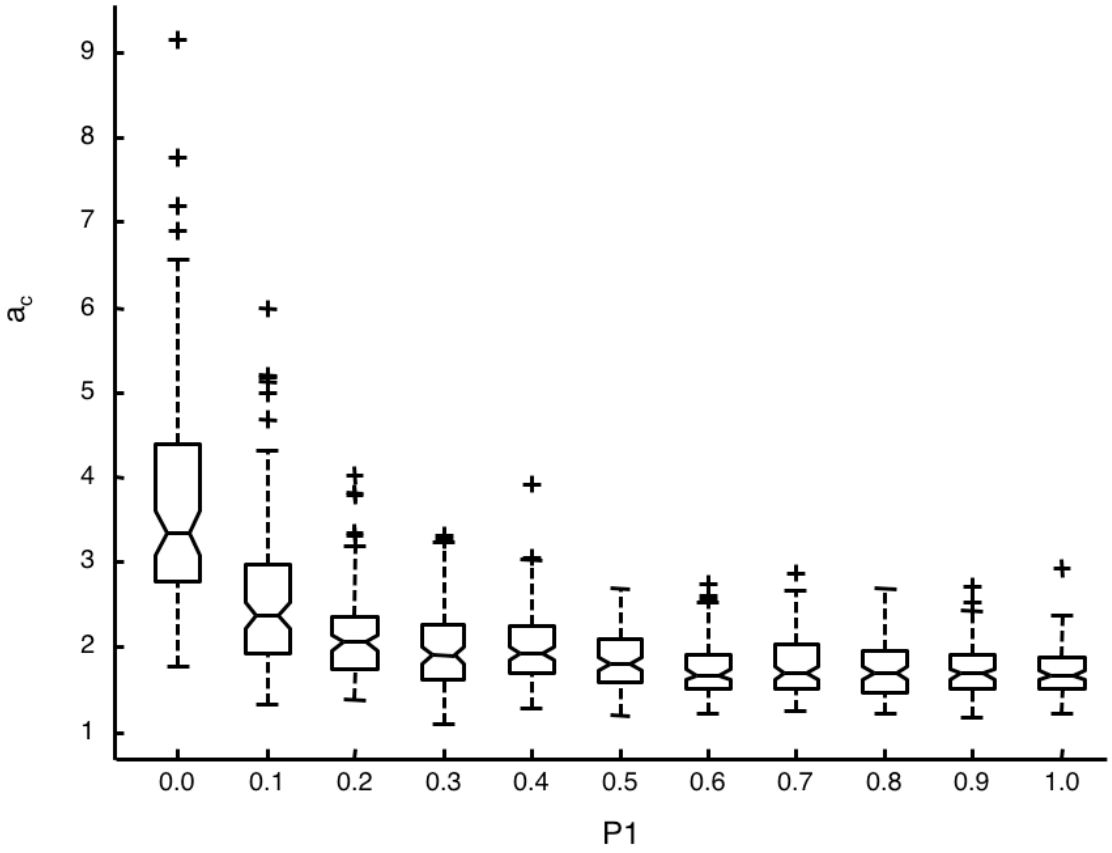

Figure 4.12(c): Simulation results of notched box plots of the effect of P1 on aspect ratio a_c when N is 100.

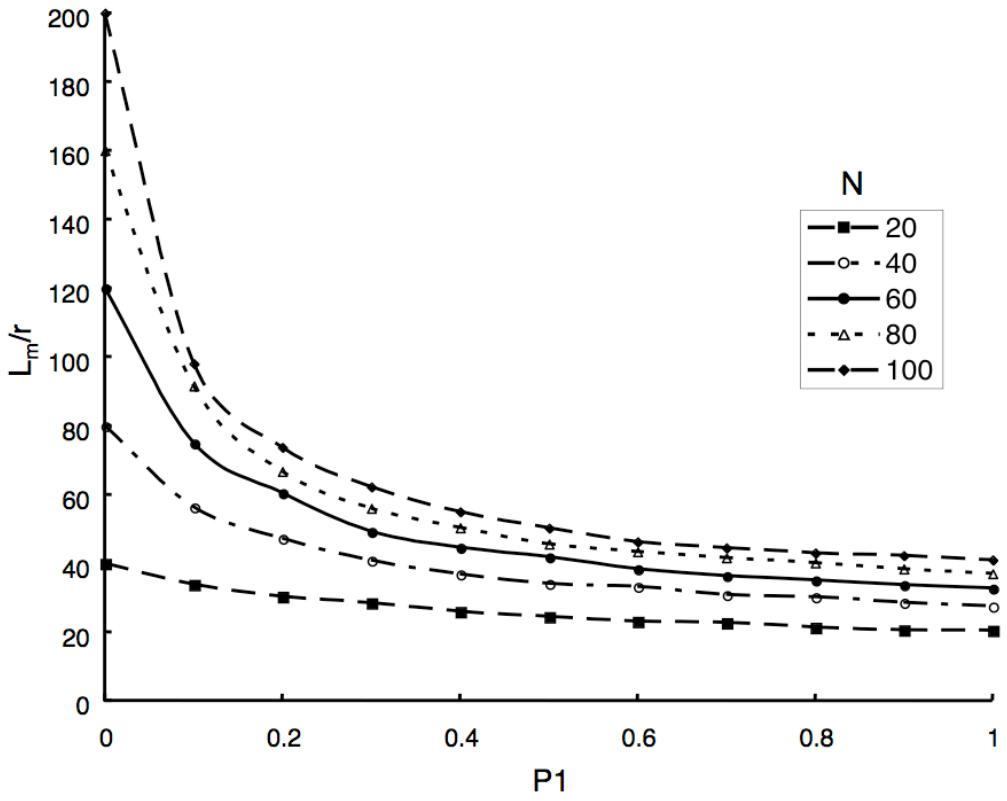

Figure 4.13: Simulation results of the effect of P1 on average main chain length normalized by particle radius, L_m/r, for cluster sizes N = 20, 40, 60, 80 and 100.

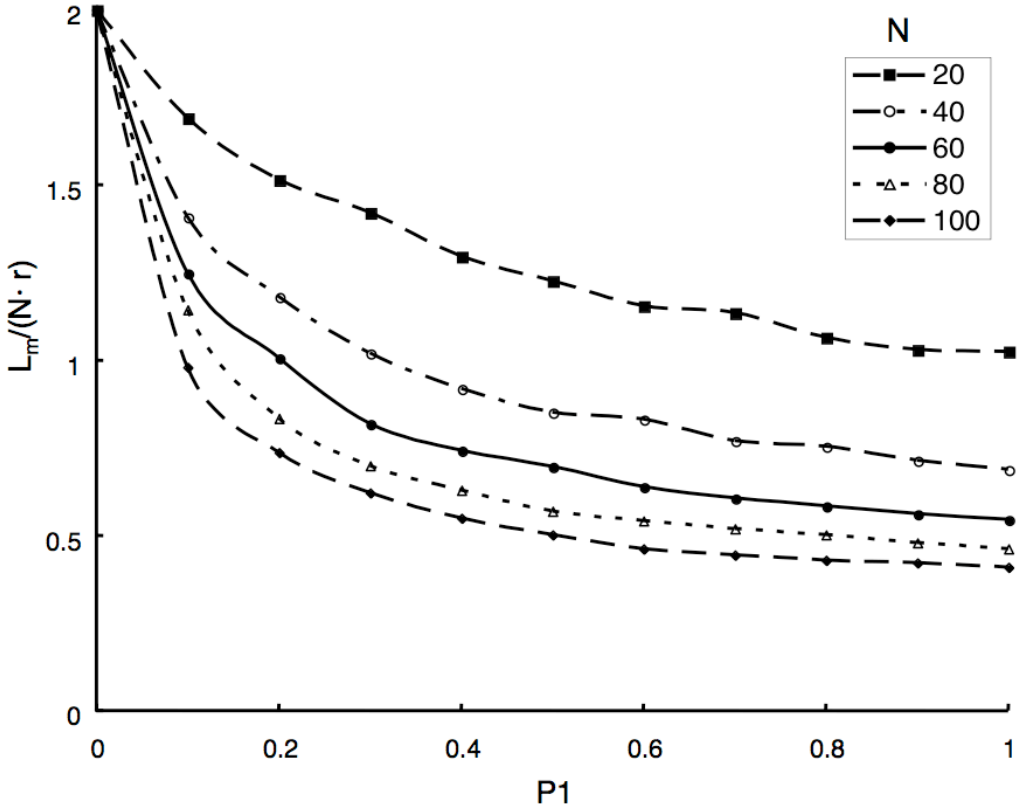

Figure 4.14: Simulation results of the effect of P1 on normalized main chain length, $L_m/(N\ r)$, for cluster sizes N = 20, 40, 60, 80 and 100.

(Recall P2 = 1 – P1.) The values for a_b are systematically lower than the values for a_c for all values of P1. Both aspect ratios decrease as the number of particles in the cluster increases, and both aspect ratios decrease as the probability of Case 1 bonding (representing van der Waals forces) increases. Figures 4.11 and 4.12 are notched-box plots of the effects of P1 on the aspect ratios a_b and a_c respectively for N = 20, 60, and 100. Each notched box has lines at the lower quartile, median, and upper quartile values. Each notched box also has whiskers which are lines extending from each end of the box to show the extent of the rest of the data in 1.5 times the interquartile range. Outliers (denoted as plus signs in the figures) are data with values beyond the ends of the whiskers. If the notches in the box plot do not overlap, one can conclude with 95% confidence that the true medians differ [46]. For example, results from Fig. 4.11 shows that when P1 is larger than 0.6, there is no significant change in the median value of a_b. Additionally, a wider range between whiskers, especially with larger values of P1, indicates larger variation in the data. Data distribution can also be observed in notched-box plots. Fig. 4.11 and 4.12 show asymmetric data distribution. Extended data deviation in larger value in Fig. 4.11 and 4.12 results in the averaged values in Fig. 9 and 10 greater than median values in Fig. 4.11 and 4.12.

Figures 4.13 and 4.14 show the effects of P1 on average main chain length L_m/r and normalized main chain length, $L_m/(N \cdot r)$, respectively, for values of N = 20, 40, 60, 80, and 100. L_m/r increases with decreasing values of P1 and increasing values of N. The normalized main chain length also increases with decreasing values of P1; however, $L_m/(N \cdot r)$ decreases with increasing values of N. P1 = 0 is the special case where new particles always stick to the tip particles, and only one chain-like structure with $L_m/(N \cdot r)$

= 2 is formed. Figure 4.15 shows the notched box plots of the effects of P1 on L_m/r for N = 20, 60, and 100. The range between whiskers decreases with increases in P1 and N. However, unlike aspect ratio, notches in the box plots for L_m/r only overlap over a small range of values for P1.

Figure 4.16 shows the effects of P1 on the average radius of gyration normalized by particle radius, R_g/r, for values of N = 20, 40, 60, 80, and 100. R_g/r increases with decreasing values for P1 for all values of N. R_g/r also increases with increasing cluster size. Figure 4.17 shows the notched box plots of the effect of P1 on R_g/r when N is 20, 60, and 100. With increases in P1 and N, the range between whiskers decreases, similar to the results for main chain length.

The simulation results were also examined to determine if the predicted structures were self-similar. Figure 4.18 presents logN as a function of $\log(R_g/r)$ for several values of P1. Each of the data sets is approximately linear on this scale, indicating the structures are self-similar. From equation (6), the slope of the line of the $\log(R_g/r)$ versus logN plot is the fractal dimension, D_f. Using regression analysis, D_f is determined for each value of P1, and the results are presented in Fig. 4.19. The fractal dimension increases from D_f = 1.8 for P1 = 0 to D_f = 3 for P1 = 1.

Table 4.2 presents the results from the image analysis of the flame-generated soot agglomerates presented in Figs. 4.5-6. The analysis yields N = 45 and r = 21.5 [pix] for agglomerate I and N = 16 and r = 20.5 [pix] for agglomerate II. Figures 4.20 and 4.21 show the simulation results for average L_m/r and R_g/r based on these values for the two agglomerates. Note the remarkable difference in the scales of Figs 4.20 and 4.21, indicating the level of sensitivity that can be achieved using the integrated modeling

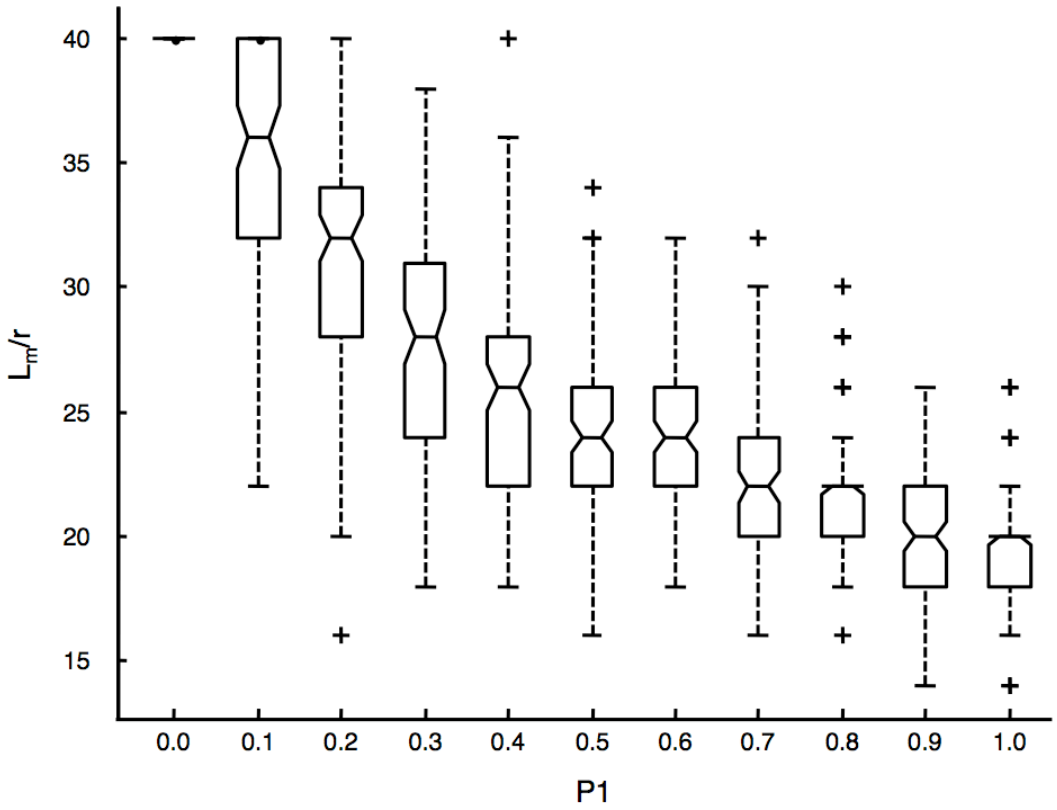

Figure 4.15(a): Simulation results of notched box plots of the effect of P1 on L_m when N is 20.

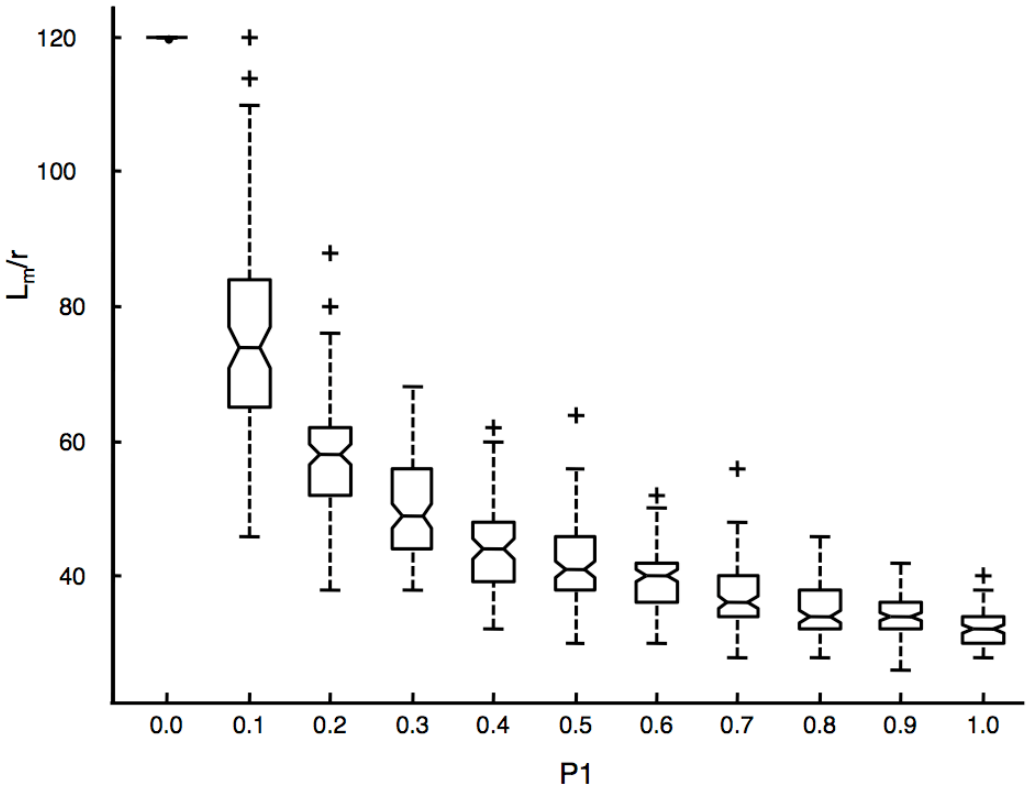

Figure 4.15(b): Simulation results of notched box plots of the effect of P1 on L_m when N is 60.

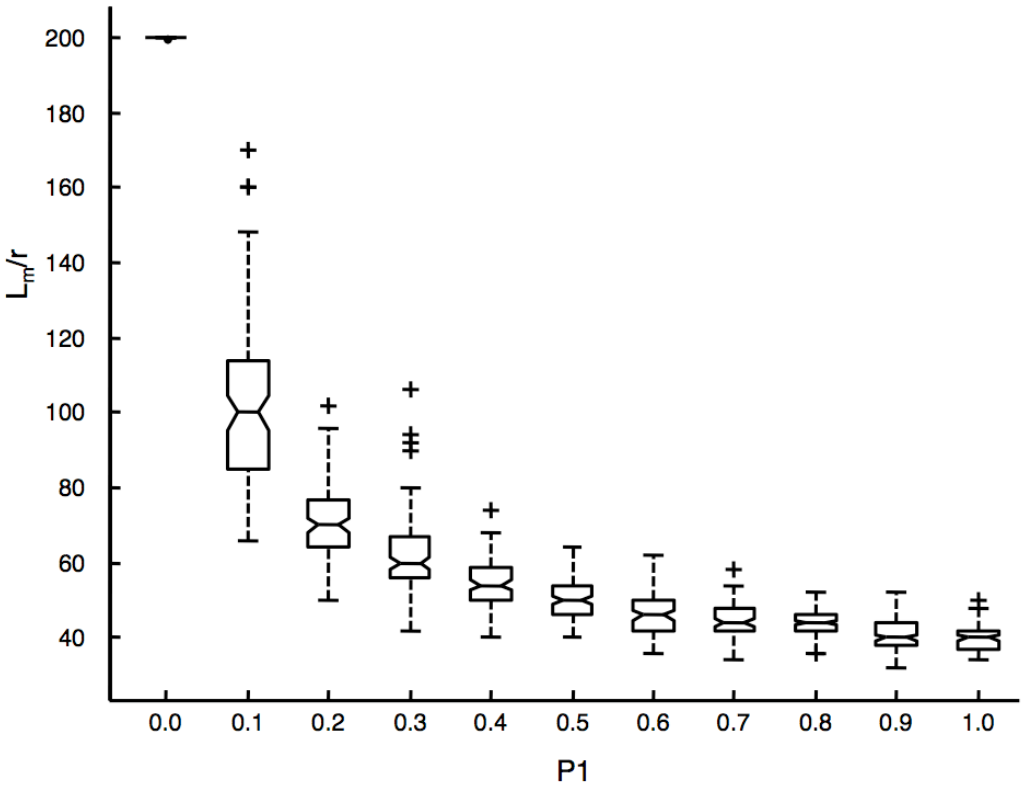

Figure 4.15(c): Simulation results of notched box plots of the effect of P1 on L_m when N is 100.

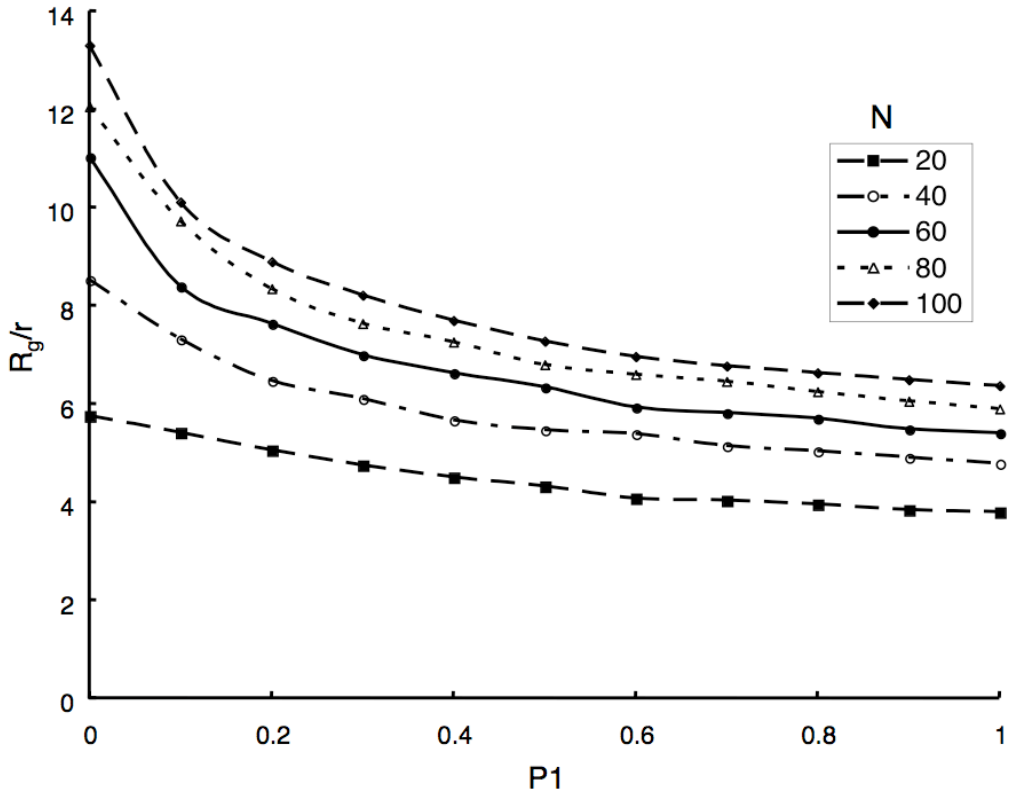

Figure 4.16: Simulation results for the effects of P1 on average radius of gyration, R_g/r, for cluster sizes N = 20, 40, 60, 80 and 100.

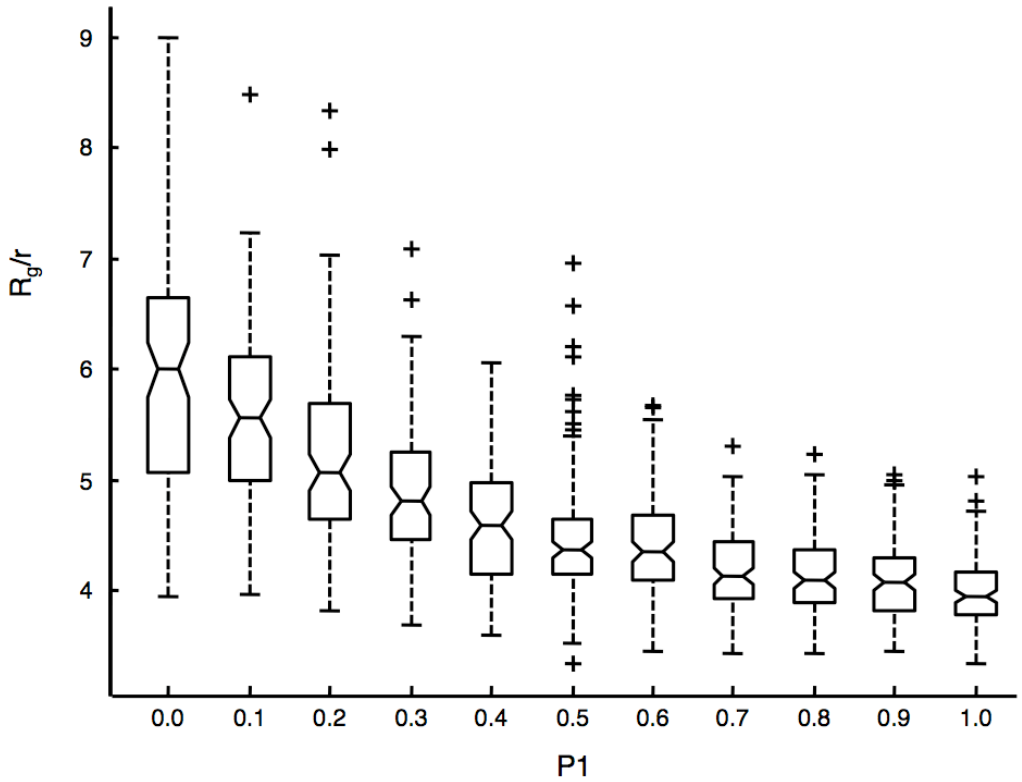

Figure 4.17(a): Simulation results of notched box plots of the effect of P1 on R_g/r when N is 20.

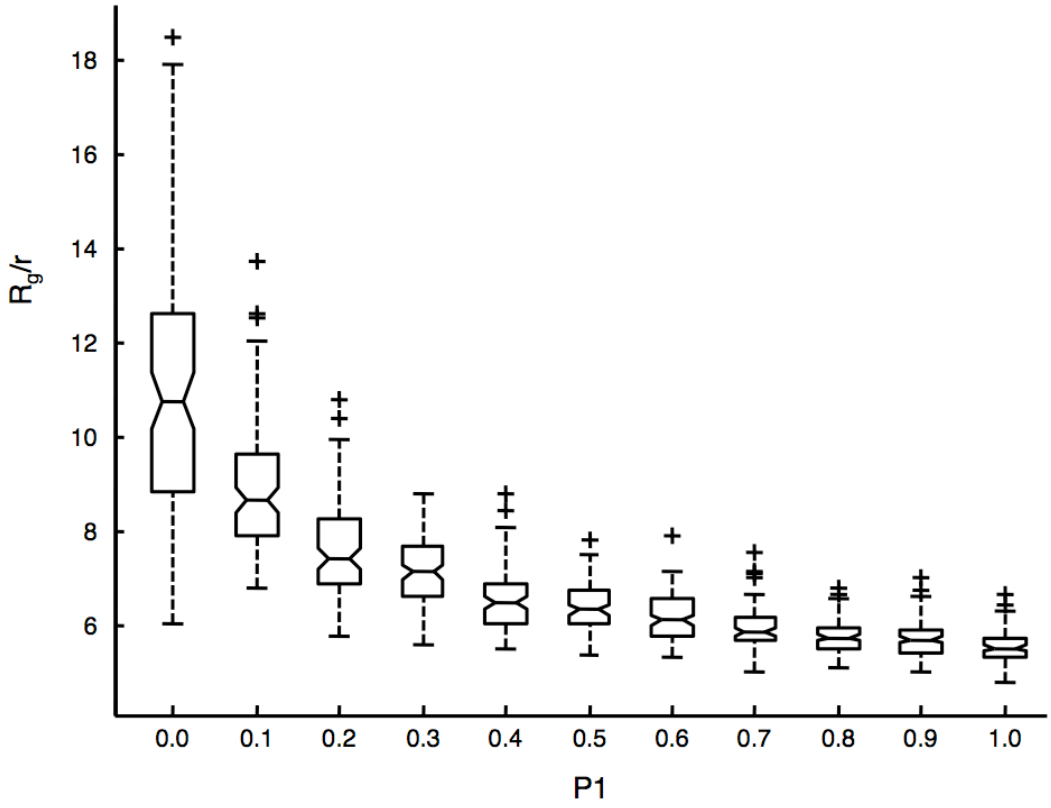

Figure 4.17(b): Simulation results of notched box plots of the effect of P1 on R_g/r when N is 60.

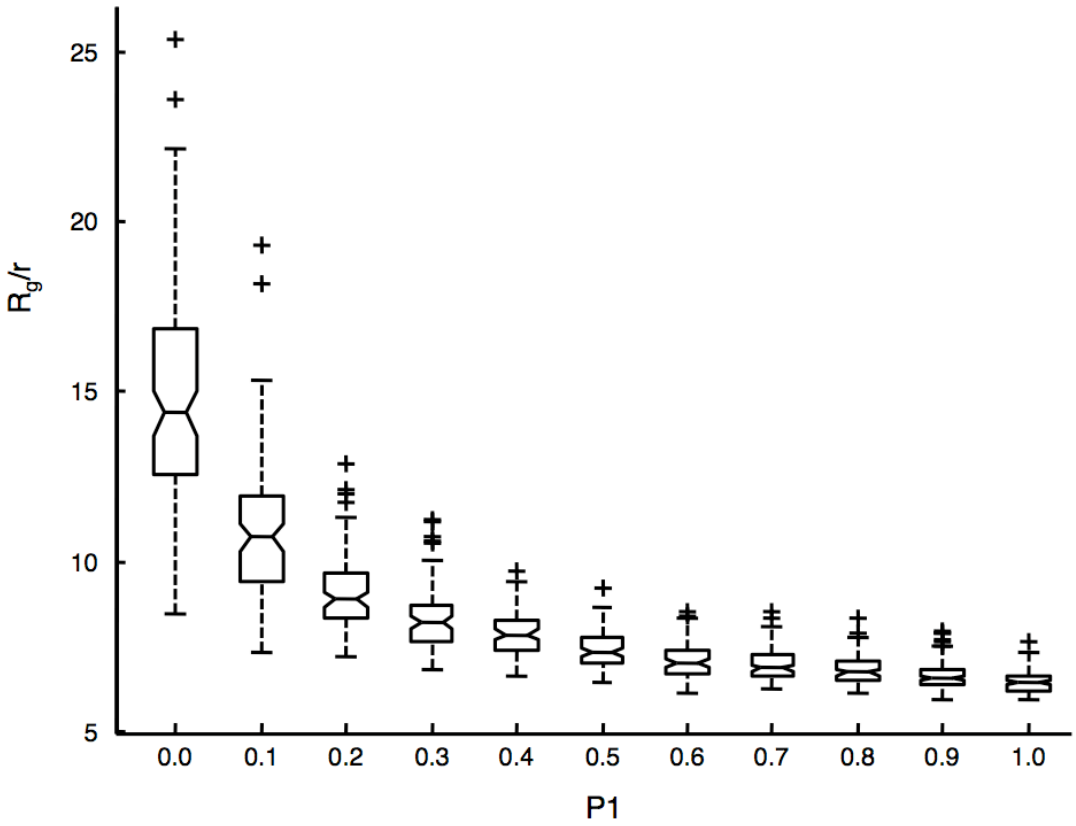

Figure 4.17(c): Simulation results of notched box plots of the effect of P1 on R_g/r when N is 100.

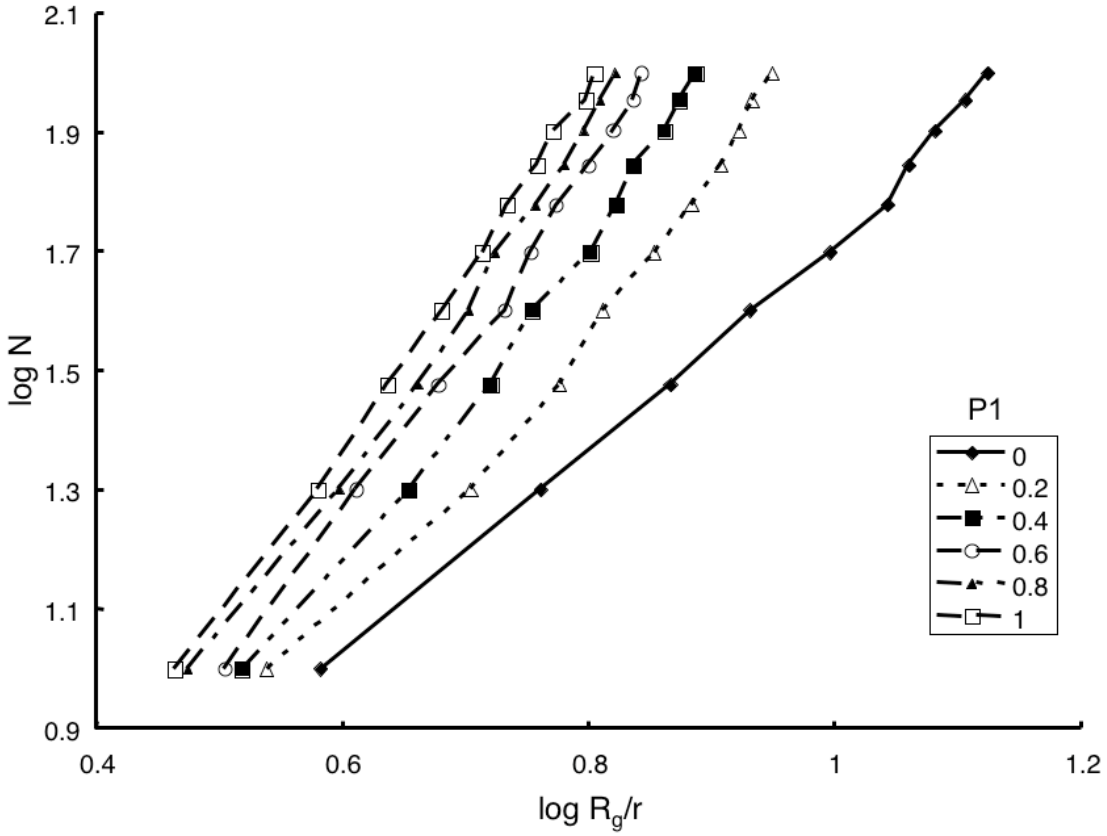

Figure 4.18: log(R_g /r) vs. logN at different P1.

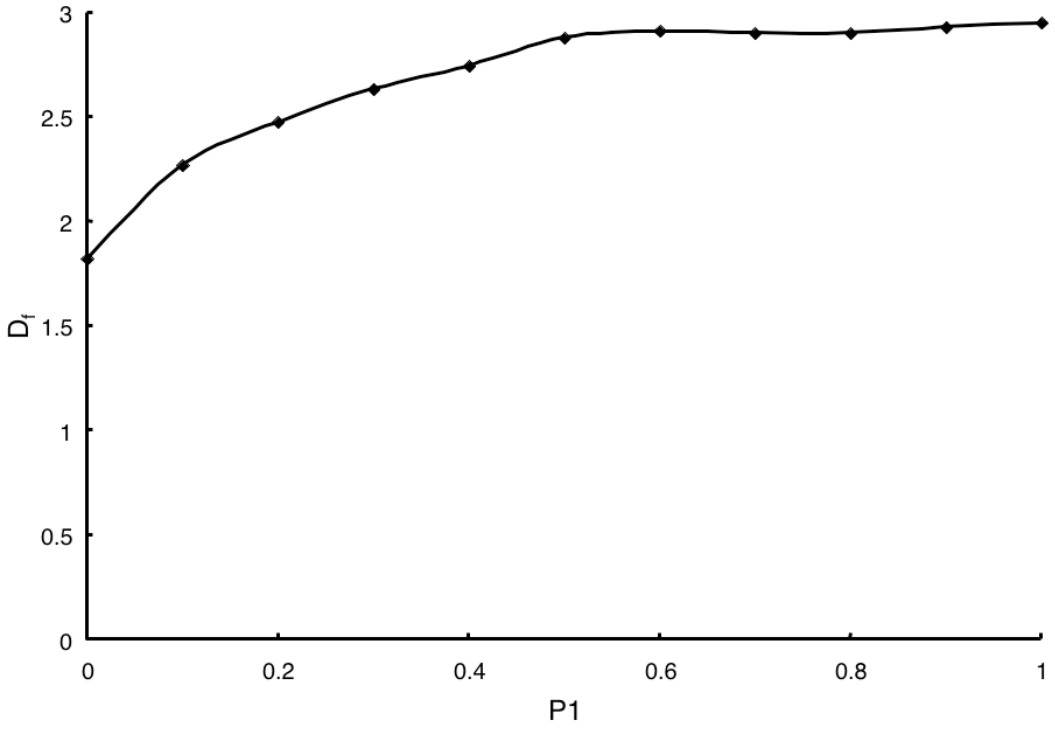

Figure 4.19: Simulation results for the fractal dimension, D_f, as a function of P1 derived from the results of Fig. 18.

Parameter	Agglomerate I	Agglomerate II
N	45	16
scale [pix/nm]	2.3	2.3
r [pix]	21.5	20.5
r [nm]	9.3	8.9
L_m [pix]	1610.3	536.8
L_m [nm]	700.1	233.4
R_g [pix]	190.2	99.3
R_g [nm]	82.7	43.2
L_m/r	74.9	26.2
R_g/r	8.8	4.8
estimated P1 by L_m/r	0-0.1	0.2-0.3
estimated P1 by R_g/r	0-0.1	0-0.3

Table 4.2: Results of image analysis of soot nanoparticle clusters.

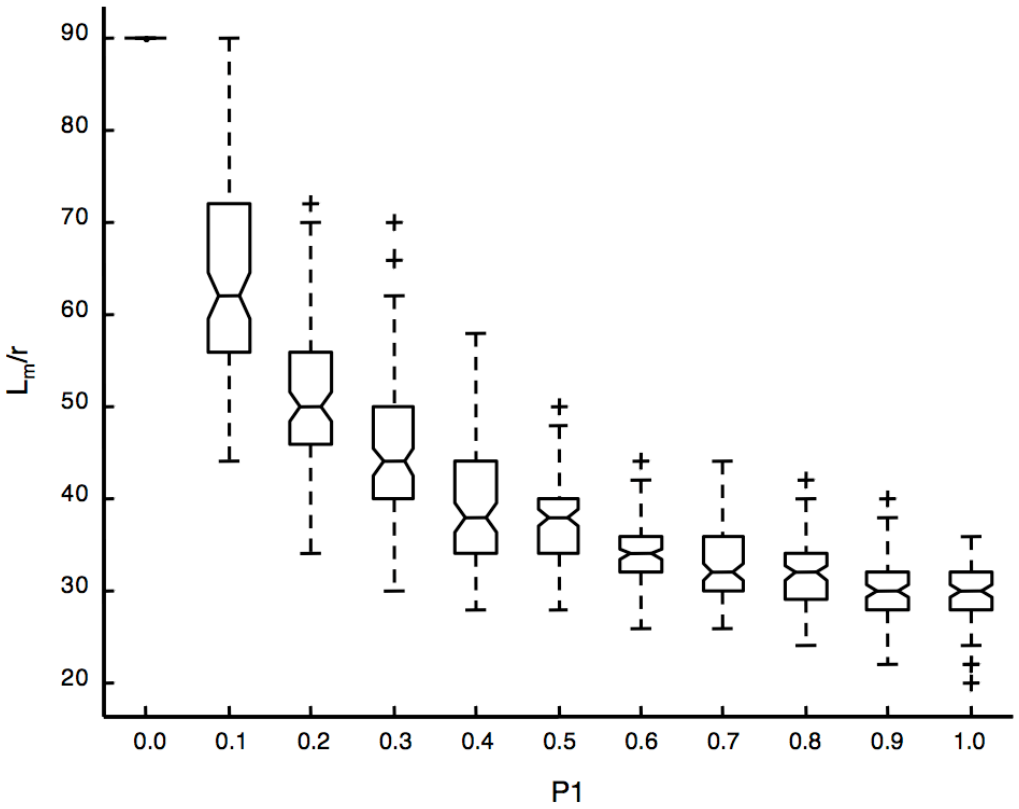

Figure 4.20(a): Simulation results of notched box plots of the effect of P1 on L_m/r for agglomerate I (N=45).

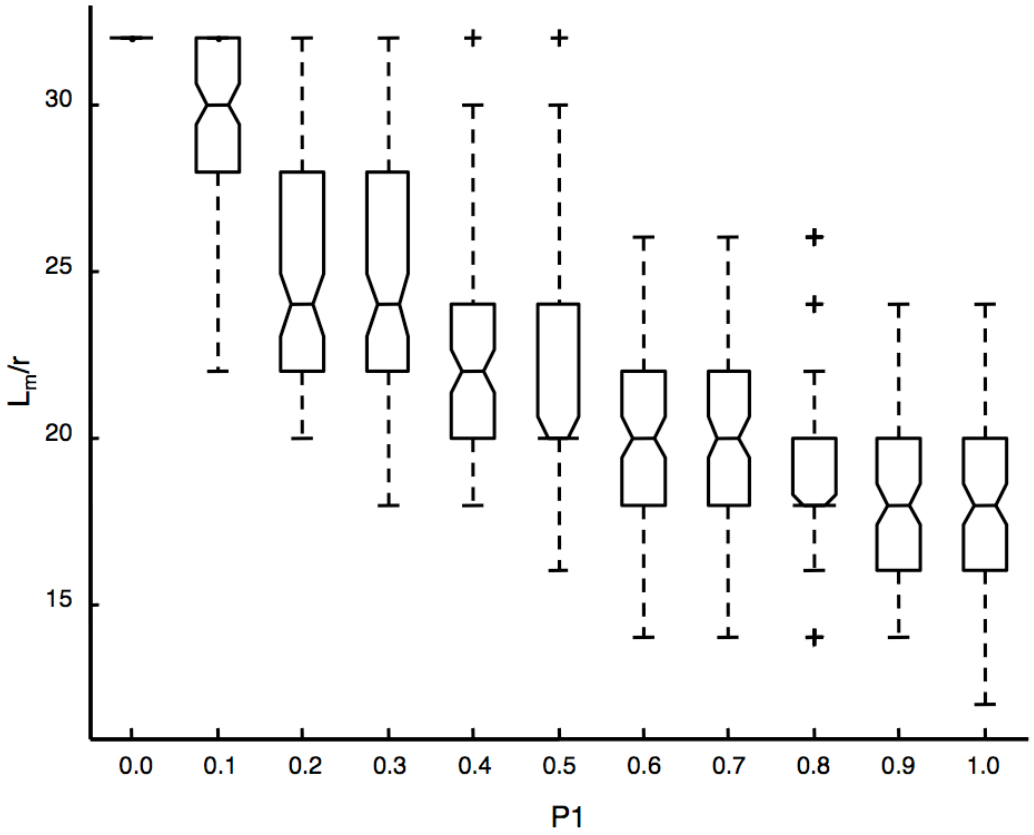

Figure 4.20(b): Simulation results of notched box plots of the effect of P1 on L_m/r for agglomerate II (N=16).

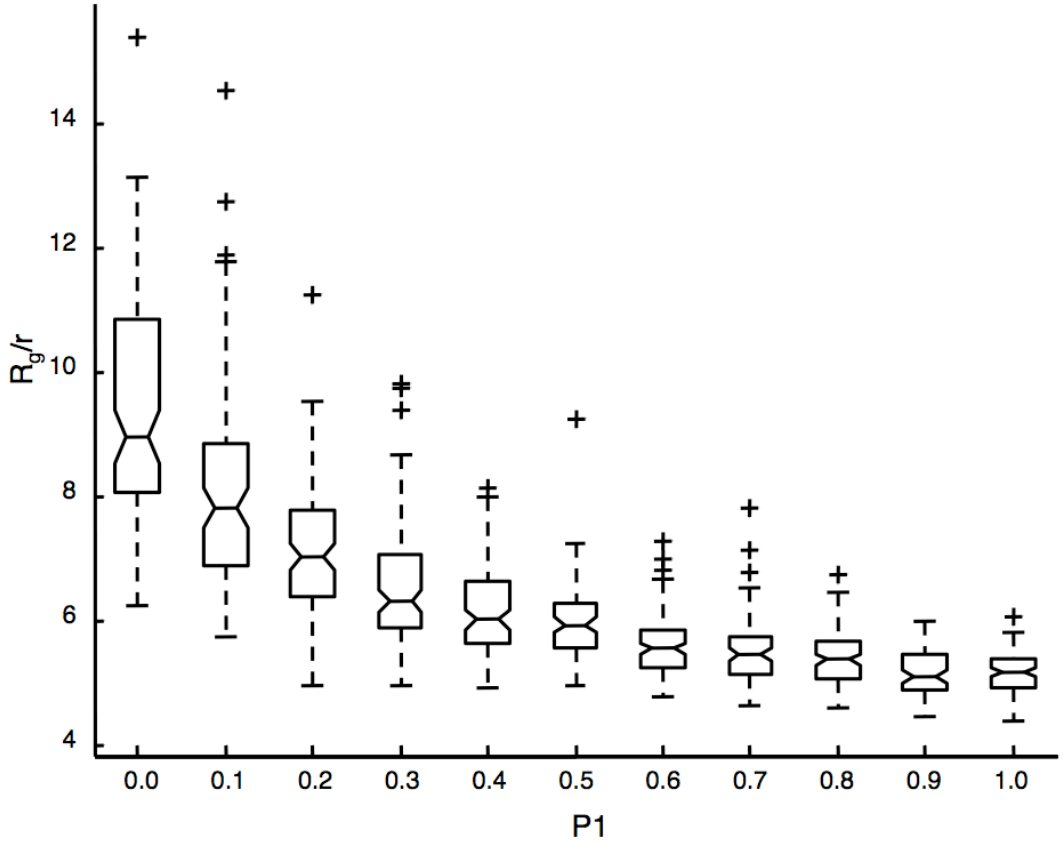

Figure 4.21(a): Simulation results of notched box plots of the effect of P1 on R_g/r for agglomerate I (N=45).

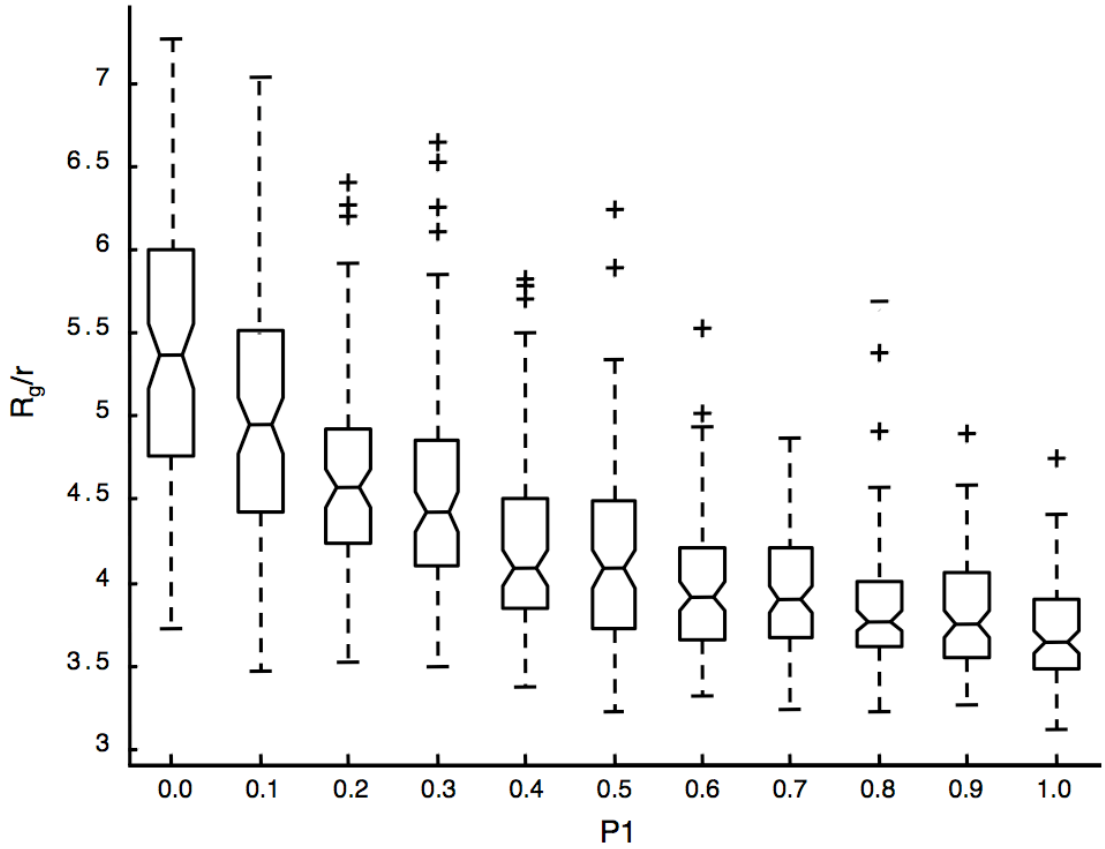

Figure 4.21(b): Simulation results of notched box plots of the effect of P1 on R_g/r for agglomerate II (N=16).

approach. Comparing the results from the experiments with the results from the simulations, if the values from the experimental imaging are located within the range of the boxes presented in Figs. 4.20 and 4.21, P1 can be determined. Estimated ranges of P1 for the two agglomerates are shown in Table 4.2. The implication of these results are discussed below.

DISCUSSION

The experimental data (Figs. 4.5-6) and the image reconstruction results (Figs. 4.7-8) both demonstrate the three dimensional nature of combustion-generated agglomerates. The nanoparticle clusters yield different 2D projections based on the orientation of the image. In traditional 2D TEM images, the view angle can falsely indicate overlapping particles or interconnections of particles. Analysis of geometric properties based only on 2D images can lead to errors. Therefore, conventional TEM images, which only show 2D projections, are not sufficient for characterization and analysis of morphology. 3D TEM provides further structural understanding in real space.

The simulation results (Figs. 4.9-19) demonstrate that Coulomb forces (Case 2) are responsible for elongated agglomerates while van der Waals forces (Case 1) yield particles with more compact structure. By varying the probabilities representing these forces, different combinations of P1 and P2 simulate different effects of van der Waals and Coulomb forces. For the results for a_b and a_c shown in Figs. 4.9-10, agglomerates tend to have larger aspect ratios when P2 is higher and particles form clusters with smaller aspect ratios when P1 is higher. This indicates that the attractive force concentrated on the tip particles is responsible for elongated shape cluster. With less

attractive force on the tip, particles tend to form a more compact structure. Also, with increasing N, new particles have more opportunities to stick to particles in the cluster which are farther from the major axes, so the aspect ratios, a_b and a_c, decrease.

The box plots of a_b and a_c in Figs. 4.11-12 indicate the variety of shapes the agglomerates can form. For lower values of P1, the whisker of the box is larger, which indicates that the shape of the clusters is more variable under the strong effects of Coulomb forces on the tip particles. In Figs. 4.11-12, the boxes overlap over a wide range of P1, which can be seen especially at smaller values of N. This overlap shows that aspect ratio is not a good parameter to uniquely characterize the forces important during the formation of agglomerates.

As seen by the simulation results of main chain length (Fig. 4.13), agglomerates tend to have higher values for L_m/r when P2 is higher. This means that with more attractive force concentrated on the tip particles, the clusters tend to form longer chain-like structures. Otherwise, without the strong forces at the tip, new particles bind to other parts of the cluster due to van der Waals forces and form more compact structures. Hence, Coulomb forces are responsible for agglomerates with long main chain length.

In Fig. 4.14, normalized L_m decreases as N increases, but the rate of change on L_m/r also decreases with increasing N. With increasing N, $L_m/(N \cdot r)$ is lower because particles have more chances to bind to other particles that are not part of the main chain. As seen in the box plots for L_m/r for N=20, 60, and 100 (Fig. 4.15), the range of the boxes decreases with increasing P1, especially at larger N. Unlike the results for aspect ratio (Figs. 4.11-12), overlapping boxes are not seen for wide ranges of values for P1, which means L_m/r is a useful parameter to characterize the forces important during the

formation of agglomerates. However, for small clusters such as agglomerates with 20 particles, boxes still overlap in a range of P1. These results indicate that for smaller agglomerates with known morphology information, comparison with data for L_m/r may identify non-unique combinations of van der Waals and Coulomb forces. In other words, there may be difficulties identifying the specific force sources for smaller clusters.

The Coulomb force is also responsible for agglomerates with large and loose structures with large radius of gyration, R_g, as seen in Fig. 4.16. R_g is a measure of overall size of a specific cluster hence R_g increases with a larger number of particles. For lower values of P1, particles tend to bind to the tip particles, increasing the length of some chains of the cluster and making the whole structure larger and less compact. Without this effect, the cluster becomes more compact and small and R_g decreases.

The box plots for radius of gyration (Fig. 4.17) show similar results to mean chain length (Fig. 4.15), where a larger variety of shapes occurs with higher values of P2 and more uniform morphology is observed with higher values of P1. Again, the range of the boxes decreases with increasing P1, especially at larger N, and overlapping boxes are not seen for large differences in P1 when N is large. As a consequence, R_g is useful to characterize the formation of agglomerates for larger cluster sizes.

As noted earlier, the simulation results for $\log(R_g/r)$ vs. logN (Fig. 4.18) indicate that the agglomerates are self-similar structures. Additionally, the simulation results (Fig. 4.19) show that agglomerates with a specific fractal dimension come from a specific combination of forces. The fractal dimension is usually used to indicate the compactness of agglomerates. For compact agglomerates in 3D, D_f is close to 3, and for chain-like structures, D_f is close to 1. With increasing P1, D_f increases close to 3 and this indicates

the compact agglomerates are formed due to van der Waals forces. When only Coulomb forces are considered (P1 = 0), D_f decreases to a value of 1.8

The forces governing the formation of a specific cluster can be estimated by comparing experimental and modeling results for L_m/r and R_g/r. Comparing the experimental results of Table 4.2 with the simulation results presented in Figs. 4.20-21, P1 for agglomerate I is estimated between 0 and 0.1 based on both L_m/r and R_g/r. The results indicate that the Coulomb forces dominate during the formation of the particle cluster. For agglomerate II, P1 is estimated between 0.2-0.3 based on the values for L_m/r, and P1 is estimated between 0-0.3 based on the values for R_g/r. As noted earlier, for smaller agglomerates various combinations of P1 and P2 can result in similar morphologies, hence the larger range of probabilities assigned to this smaller agglomerate.

The results for the forces governing the SnO_2 nanoparticle cluster formation are consistent with other studies of agglomeration of combustion generated particulates. For example, Onischuk et al. [18] studied agglomeration through experimental observation of particle/agglomerate interactions of carbonaceous soot aerosols and silicon aerosols generated through silane pyrolysis. They found that "Coulomb interactions are significant during the sticking process and, in particular, they are responsible for the fractal dimension." The authors also found the type and extent of dipole charge varied between the two materials studied.

The radii of gyration determined by the simulations and by the reconstruction of the TEM images are consistent with other measurements of flame generated particulates. For example, Sztucki et al. [47] studied clusters of carbon particles formed in an

acetylene flame using small-angle x-ray scattering (SAXS). The authors found the soot particles formed fractal structures where R_g varied from 45 to 300 [nm] based on the residence time of the particles in the flame. Their work showed that the longer the residence time, the larger the radius of gyration. The measured values for R_g for agglomerates I (83 nm) and II (43 nm) (Table 4.2) and the computed range of values shown in Fig. 4.21 (normalized) are consistent with the SAXS data.

BIBLIOGRAPHY

1. M. S. Wooldridge, Gas-phase combustion synthesis of particles, Prog. Energy Combust. Sci. 24, 63 (1998). M. F. Yan, Solid-state sintering, Engineered Material Handbook, Ceramics Glasses 4, 270-284 (1987).

2. B. Nowack and T. D. Bucheli, Occurrence, behavior and effects of nanoparticles in the environment, Environ. Pollut. 150, 5 (2007).M. S. Wooldridge, Gas-phase combustion synthesis of particles, Progress in Energy Combustion Science 24 (1), 63-87 (1998).

3. U.S. Environmental Protection Agency, "National Air Pollutant Emission Trends, 1900-1998", http://www.epa.gov/ttn/chief/trends/trends98/.S. Froeschke, S. Kohler, A. P. Weber, G. Kasper, Impact fragmentation of nanoparticle agglomerates, Journal of Aerosol Science 34, 275-287 (2002).

4. J. S. Lighty, J. M. Veranth, and A. F. Sarofim, Combustion aerosols: factors governing their size and composition and implications to human health, J. Air Waste Manag. Assoc. 50, 1565 (2000).

5. M. M. Maricq, Chemical characterization of particulate emissions from diesel engines: A review, J. Aerosol Sci. 38, 1079 (2007).

6. H.-H. Grotheer, H. Pokorny, J. Happold, T. Gonzalez Baquet, M. Thierley, M. Aigner, C. Baumstark-Khan, C. E. Hellweg, and A. Arenz, On combustion generated nanoparticles and their biological effects. Part I: Measurement of nanoparticles and their detection in and behind flames, Current Nanoscience 3, 199 (2007).P. K. Das, S. Bhattacharjee, Electrostatic interactions between nanoprticles in confined spaces: influence of confining wall roughness, Proceedings of the International Conference on MEMS, NANO, Smart Systems, 0-7695-1947-4/03 (2003).

7. D. Coelho, S. Bekki, J.-F Thovert, and P. M. Adler, Uptake on fractal particles. 1. Theoretical framework, J. Geophys. Res. 105, 3905 (2000).N. Morgan, C. Wells, M. Kraft, W. Wagner, Modelling Nanoparticle Dynamic: Coagulation, Sintering, Particle Inception Surface Growth, Cambridge Center for Computational Chemical Engineering Report, ISSN 1473-4273, (2003). (to be published)

8. S. Bekki, C. David, K. Law, D. M. Smith, D. Coelho, J.-F Thovert, and P. M. Adler, Uptake on fractal particles. 1. Applications, J. Geophys. Res. 105, 3917 (2000).L. H. Radzilowski, B. O. Carragher, S. I. Stupp, Three-dimensional self-assembly of rodcoil copolymer nanostructures, Macromolecules 30 (7), 2110-2119 (1997).

9. N. Yamazoe, New approaches for improving semiconductor gas sensors, Sens. Actuators B 5, 7 (1991).

10. R. Strobel and S. E. Pratsinis, Flame aerosol synthesis of smart nanostructured materials J. Mater. Chem. 17, 4743 (2007).

11. R. Strobel, A. Baiker, and S. E. Pratsinis, Aerosol flame synthesis of catalysts, Adv. Powder Tech. 17, 457 (2006).

12. H. Hahn, Gas phase synthesis of nanocrystalline materials, Nanostruct. Mater. 9, 3 (1997).S. Hayashi, Y. Hisaeda, Y. Asakuma, H. Aoki, T. Miura, Simulation of soot aggregates formed by benzene pyrolysis, Combustion and Flame, 117 (4), 851-860 (1999).

13. G. Skandan and A. Singhal, Tailoring nanostructured powders for functional and structural applications, Powder Metallurgy 43, 313 (2000).

14. Soot Formation in Combustion, Mechanisms and Models, edited by H. Bockhorn, (Springer-Verlag, Berlin, 1994).

15. R. C. Flagan, M. M. Lunden, Particle structure control in nanoparticle synthesis from the vapor phase, Mater. Sci. Eng. A204, 113 (1995).

16. N. Morgan, M. Kraft, M. Balthasar, D. Wong, M. Frenklach, and P. Mitchell, Numerical simulations of soot aggregation in premixed laminar flames, Proc. Combust. Inst. 31, 693 (2007).S. D. Bakrania, T. A. Miller, C. Perez, M. S. Wooldridge, Combustion of multiphase reactants for the synthesis of nanocomposite materials, Combustion and Flame 148 (1-2), 76-87 (2007).

17. K. Adachi, S. H. Chung, H. Friedrich, and P. R. Buseck, Fractal parameters of individual soot particles determined using electron tomography: implications for optical properties, J. Geophys. Res. D 112, D14202 (2007).J. R. Kremer, D. N. Mastronarde, R. McIntosh, Computer visualization of three-dimensional image data using IMOD, Journal of Structural Biology 116 (1), 71-76 (1996).

18. A. A. Onischuk, S. di Stasio, V. V. Karasev, V. P. Strunin, A. M. Baklanov, and V. N. Panfilov, Evidence for long-range coulomb effects during formation of nanoparticle agglomerates from pyrolysis combustion routes, J. Phys. Chem. A 104, 10426 (2000).

19. S. Froeschke, S. Kohler, A. P. Weber, and G. Kasper, Impact fragmentation of nanoparticle agglomerates, J. Aerosol Sci. 34, 275 (2003).S. K. Friedlander, Smoke, Dust, and Haze: Fundamentals of Aerosol Dynamics, Oxford University Press, New York, pp. 222, 2000.

20. N. Lümmen and T. Kraska, Investigation of the formation of iron nanoparticles from the gas phase by molecular dynamics simulation, Nanotech. 15, 525 (2004).

21. M. R. Zachariah and M. J. Carrier, Molecular dynamics computation of gas-phase nanoparticle sintering: a comparison with phenomenological models, J. Aerosol Sci. 30, 1139 (1999).

22. T. Hawa and M. R. Zachariah, Molecular dynamics study of particle-particle collisions between hydrogen-passivated silicon nanoparticles, Physical Review B 69, 035417-1 (2004).

23. Y. Qin and K. A. Fichthorn, Molecular-dynamics simulation of forces between nanoparticles in a Lennard-Jones liquid, J. Chem. Phys. 119, 9745 (2003).

24. P. K. Das and S. Bhattacharjee, Electrostatic interactions between nanoparticles in confined spaces: influence of confining wall roughness, Proceedings of the International Conference on MEMS, NANO, Smart Systems, 0-7695-1947-4/03 (2003).

25. S.-M. Suh, M. R. Zachariah, and S. L. Girshick, Modeling particle formation during low-pressure silane oxidation: Detailed chemical kinetics and aerosol dynamics, J. Vac. Sci. Tech. A 19, 940 (2001).

26. A. Sinyagin, A. Belov, N. Kotov, Monte Carlo simulation of linear aggregate formation from CdTe nanoparticles, Model. Sim. Mater. Sci. Eng. 13, 389 (2005).

27. N. Morgan, C. Wells, M. Kraft, and W. Wagner, Modelling nanoparticle dynamics: coagulation, sintering, particle inception and surface growth, Combust. Theory Model. 9, 449 (2005).

28. J. Frank (Ed.), Electron Tomography: Three-Dimensional Imaging with the Transmission Electron Microscope, (Plenum Press, New York, 1992).

29. A. J. Koster, U. Ziese, A. J. Verkleij, A. H. Janssen, and K. P. de Jong, Three-dimensional transmission electron microscopy: a novel imaging and characterization technique with nanometer scale resolution for materials science, J. Phys. Chem. B 104, 9368 (2000).

30. L. H. Radzilowski, B. O. Carragher, and S. I. Stupp, Three-dimensional self-assembly of rodcoil copolymer nanostructures, Macromolecules 30, 2110 (1997).

31. S. Kohjiya, A. Katoh, J. Shimanuki, T. Haseqawa, and Y. Ikeda, Three-dimensional nano-structure of in situ silica in natural rubber as revealed by 3D-TEM/electron tomography, Polymer 46 (12) 4440 (2005).

32. K. Tian, F. Liu, M. Yang, K. A. Thomson, D. R. Snelling, and G. J. Smallwood, Numerical simulation aided relative optical density analysis of TEM images for soot morphology determination, Proc. Combust. Inst. 31, 861 (2007).

33. K. Tian, K. A. Thomson, F. Liu, D. R. Snelling, G. J. Smallwood, and D. Wang, Determination of the morphology of soot aggregates using the relative optical

density method for the analysis of TEM images, Combust. Flame 144, 782 (2006).

34. R. Fisker, J. M. Carstensen, M. F. Hansen, F. Bødker, and S. Mørup, Estimation of nanoparticle size distributions by image analysis, J. Nanopart. Res. 2, 267 (2000).

35. M. T. Reetz, M. Maase, T. Schilling, and B. Tesche, Computer image processing of transmission electron micrograph pictures as a fast reliable tool to analyze the size of nanoparticles, J. Phys. Chem. B 104, 8779 (2000).

36. S. Hayashi, Y. Hisaeda, Y. Asakuma, H. Aoki, T. Miura, H. Yano, and Y. Sawa, Simulation of soot aggregates formed by benzene pyrolysis, Combust. Flame, 117 851 (1999).

37. Ü. Ö. Köylü, G. M. Faeth, T. L. Farias, and M. G. Carvalho, Fractal and projected structure properties of soot aggregates, Combust. Flame 100, 621 (1995).

38. D. Fry, A. Mohammad, A. Chakrabarti, and C. M. Sorensen, Cluster shape anisotropy in irreversibly aggregating particulate systems, Langmuir 20, 7871 (2004).

39. T. A. Miller, S. D. Bakrania, C. Perez, and M. S. Wooldridge, A new method for direct preparation of tin-dioxide nanocomposite materials, J. Mater. Res. 20, 2977 (2005).

40. S. D. Bakrania, C. Perez, and M. S. Wooldridge, Methane-Assisted Combustion synthesis of nanocomposite tin dioxide materials, Proc. Combust. Inst. 31, 1797 (2007).

41. S. D Bakrania, T. A. Miller, C. Perez, and Wooldridge, M. S., Combustion of multiphase reactants for the synthesis of nanocomposite materials, Combust. Flame 148, 76 (2007).

42. The IMOD Home Page, http://bio3d.colorado.edu/imod/index.html), Boulder Lab For 3D Electron Microscopy of Cells, University of Colorado.

43. J. R. Kremer, D. N. Mastronarde, and R. McIntosh, Computer visualization of three-dimensional image data using IMOD, J. Struct. Bio. 116, 71 (1996).

44. T. H. Cormen, C. E. Leiserson, and R. L. Rivest, Introduction to Algorithms (The MIT Press, Cambridge, 1990).

45. S. K. Friedlander, Smoke, Dust, and Haze: Fundamentals of Aerosol Dynamics, (Oxford University Press, New York, 2000).

46. R. McGill, J. W. Tukey, and W. A. Larsen, Variations of boxplots, The Amer. Stat. 32 12 (1978).

47. A. A. Onischuck, S. di Stasio, V. V. Karasev, V. P. Stunin, A. M. Baklanov, and V. N. Panfilov, Evidence for long-range Coulomb effects during formation of nanoparticle agglomerates from pyrolysis and combustion routes, J. Phys. Chem. 104, 10426 (2000).

CHAPTER V

CONCLUSIONS AND FUTURE WORK

SELECTION OF CONDUCTIVE ADDITIVES

A method was presented to simulate the particulate system of conductive additives in Li-ion battery cathodes and quantify relationships among concentrations of specific additives, and conductivity. The error due to size effect of the domain was negligible for the selected ratio $L/d > 2.5$. Variances in the simulation results mainly arose from differences in arrangements of random structures. Our model is capable of generating realistic microstructures of cathode systems, and robustly predicting the effective conductivities of different types of conductive additives, e.g. conductive surface coatings and larger, disperse conductive additives.

A key finding was that the conductive coatings strongly influence conductivity, because they substantially reduce contact resistance. Percolation was detected in these systems at a volume fraction of active material ≥30%,which is somewhat higher than the theoretical percolation threshold (29%) for 3D spherical particulate systems. Generally, using carbon black/PVDF composite coatings was found to be more advantageous than addition of conductors (e.g. graphite) to composite cathodes, for all baseline materials. Overall, the best conductivity in each system studied was achieved by combination of

30% active material, 40% porosity, 7.5% graphite, 10.15% carbon black, and 12.35% PVDF.

Neither surface nor bulk modifications of active material particles conductivities seem desirable targets for improvement of laminate conductivity, for the ranges of materials studied. Our simulation results showed that the differences among the highest normalized conductivities of each system were within one order in magnitude, while the conductivities of four active materials, spanned four orders of magnitude (5.91×10^{-1} to 5.56×10^{-4} S/m). Even with only a 10% volume fraction of coating (4.51% carbon black, 5.49% PVDF) in cases of 50% porosity and 40% active material, the overall conductivity was increased by at least 14.9 S/m, a value 25 times larger than the bulk conductivity of the active material. An improvement of approximately three orders of magnitude in conductivity (PVDF/C: $7.6x10^{2}$ S/m vs. LiFePO4: $5.91x10^{-1}$ S/m), of the active material would be required to offer substantial improvement in overall conductivity.

As part of future work, the trade-off between conductivity and capacity will be considered. Next steps will include study of the effect of improved conductivity in the simulations of battery performance, in order to further optimize cathode design.

POROUS CATHODE OPTIMIZATION FOR LITHIUM CELLS

A method was presented to investigate relationships between ionic and electronic conductivity in the Li-ion battery cathode systems, and correlate the conductivity to specific energy, to improve cathode design. Cathode electrodes were optimized for best specific conductivity at a 3C rate. The highest specific energy, 323.5 Wh/kg, was

obtained by selection of 36.2% active material, 0% graphite, 10% PVDF/C, and 192.5 μm cathode thickness.

One key finding is that there is a trade-off between ionic and electronic conductivity, and neither best electronic nor ionic conductivity results in the best overall specific energy. Monotonically increasing electronic conductivity by adding more conductive additive particles is unnecessary, and actually reduces specific properties, since highly conductive surface coatings better provide improved conductivity through reduction of contact resistance. Also, compression of cathode systems in order to obtain higher electronic conductivity and theoretical capacity density, appears undesirable, in terms of specific energy for the ranges of materials studied.

Generally, design rules for cathode electrodes of higher specific energy, also apply for design for higher utilization and specific power. To improve performance, it is important to consider the effect of cathode thickness and volume fraction of active material with regard to the ion transport, cathode capacity, and total mass of active material. Even though specific energy was set as the only objective function for the present research, both high utilization (0.88), and high specific power (1614 W/kg) were also achieved.

We demonstrated the importance of cathode design and provided a baseline to optimize cathode composition with additives to obtain best specific energy. Our next step is to incorporate this technique with different materials to design high rate cells.

AGGLOMERATION AND AGGRATION

A method including 3D model reconstruction, image analysis, and computer simulation was developed to identify factors important in agglomeration and aggregation of nanoparticles. Our approach used probabilistic techniques, along with image analysis, rather than first physiochemical principles, to predict and analyze mechanisms of cluster formation. Application of the model over a range of probabilities representing varying levels of Coulomb and van der Waals forces showed that Coulomb forces concentrated on the tip of particle clusters inevitably lead to formation of long chain-like shapes, creating branchy agglomerates. Coulomb forces were also found to be responsible for greater variability in the shapes of clusters. Particles tended to form more compact and smaller clusters when van der Waals forces dominated. Our simulation results suggest that radius of gyration and main chain length are better parameters than aspect ratio to characterize the forces governing 3D cluster formation. The simulation results also indicated that the clusters form self-structures under certain combinations of interactions.

Agglomerates generated by combustion systems are 3D branchy structures, as shown using reconstruction methods combined with 2D TEM imaging. Analysis of 2D TEM images using a single projection angle does not contain sufficient information to reconstruct the 3D shape of the combustion nanoparticle agglomerate. Additionally, 2D projected images can lead to incorrect assumptions regarding the real cluster geometry. 3D reconstruction models can provide information on the actual particle morphology and make direct comparison with simulation possible. Comparisons among representative soot agglomerates and simulation results allowed validation of the approach, in identifying mechanisms important for cluster formation. Specifically, the branchy

structures observed for the soot particles were attributable to strong Coulomb forces, with minimal van der Waals interactions.

The approach demonstrated in this work combines experimental data, image reconstruction and semi-stochastic modeling, and is a powerful means to analyze particle clusters, providing new insight without high computational costs. For example, this approach can be applied to provide new understanding such as what are the forces controlling the formation of highly ordered structures in flames, such as rods and whiskers, as opposed to fractal agglomerates and aggregates. With greater resolution, this method may provide even higher level of detail such as the charge state of the nanoparticle clusters. Additionally, such methods can be the basis for developing predictive models for particle formation that can bridge the gap between detailed chemical modeling and nanoparticle interactions. Moreover, semi-stochastic modeling provides critical information on particle shape.